August 2014

Thesis for Doctorate Degree

Simulation Method based-on Dipole Model for the AC-type Magnetic Camera in the Nondestructive Testing and Evaluation

Graduate School of Chosun University

Department of Control and Instrumentation Engineering

Le Minh Huy

비파괴 평가를 위한 교류형 자기카메라의 다이폴 모델 기반 시뮬레이션 기법에 관한 연구

Simulation Method based-on Dipole Model for Magnetic

Camera in Nondestructive Testing and Evaluation

2014 년 8 월 25 일

조선대학교 대학원

제어계측공학과

레민후이

비파괴 평가를 위한 교류형 자기카메라의 다이폴 모델 기반 시뮬레이션 기법에 관한 연구

지도교수 　　　이 진 이

이 논문을 공학박사 학위신청 논문으로 제출함

2014 년 4 월

조선대학교 대학원

제어계측공학과

레민후이

레민후이의 박사학위 논문을 인준함

위원장　　조선대학교　　교수　　고낙용　　인

위원　　　국방대학교　　교수　　신기수　　인

위원　　　조선대학교　　교수　　조창현　　인

위원　　　(주)네드텍　　부장　　전종우　　인

위원　　　조선대학교　　교수　　이진이　　인

2014 년 6 월

조선대학교 대학원

CONTENTS

List of Tables

List of Figures

NONMECLATURE

NDT	Nondestructive testing
NDE	Nondestructive evaluation
PT	Penetrant testing
RT	Radiography testing
UT	Ultrasonic testing
ET	Electromagnetic testing
MT	Magnetic particle testing
MFLT	Magnetic flux leakage testing
ECT	Eddy current testing
AMR	Magnetoresistance sensor
GMR	Giant magnetoresistance sensor
Hall	Hall sensor
AC	Alternating current
DC	Direct current
PDE	Partial Differential Equation
FEM	Finite Element Method
BEM	Boundary Element Method
FDM	Finite Difference Method
TREE	Truncated Region Eigenfunction Expansion
MOI	magneto-optical eddy current imager
ID/OD	Inner/outer diameter
EM	Electromagnetic
MURX	Relative magnetic permeability in X-direction
RSVX	Electrical resistivity in X-direction
LMC	Linear-type magnetic camera
LIHaS	Linearly integrated Hall sensor array
AIHaS	Area-type integrated Hall sensors array
RMS	Root-mean-square
ADC	Analog-to-digital converter
AMP	Amplifier

HPF	High-pass-filter
STIC	Sheet-type induce current
CMC	Cylinder-type magnetic camera
LGM	Linear guide motor
LSM	Line scan mode
ASM	Area scan mode
BIHaS	Bobbin-type integrated Hall sensors array
CIHaS	Cylinder-type integrated Hall sensors array
BMC	Bobbin-type magnetic camera
D_{RMS}	RMS data using in 1/nRN algorithm
G	Amplifier gain constant
K_H	Hall constant
I_H	Hall input current
B_{RMS}	RMS magnetic intensity
$\Delta B(r, \theta)$	Differential magnetic intensity in radial direction
$\Delta B\vert_{total}$	Integrated absolute value of $\Delta B(r, \theta)$ in an area
$(r, \theta, w/2sin\varphi)$	Cylindrical coordinate of magnetic charge (A)
(R_s, θ_s, z_s)	Cylindrical coordinate of each sensing element (B)
R_s, R_I, R_O	Radius of sensing area, inner surface, and outer surface of the specimen
F	Function of the integral of the magnetic field
V_H	Hall output voltage
V_{RMS}	RMS of Hall output voltage
ΔV_{RMS}	Differential RMS of Hall output voltage
$\Delta V_{RMS}\vert_{total}$	Integrated square value of ΔV_{RMS} in an area
Q	Optimized function used to find optimum value of magnetic charge factor
m_{RMS}	RMS of magnetic charge
$DivA = \nabla \cdot A$	Divergence of Vector A
$GradU = \nabla U$	Gradient of Scalar U
$RotA = CurlA = \nabla \times A$	Rotational of Vector A
H	Magnetic field intensity[A/m]
B	Magnetic flux density [Web/m^2]

- xi -

Collection @ chosun

J	Electric current density[A/m^2]
Js	Current density of source[A/m^2]
Je	Current density of eddy current[A/m^2]
E	Electric field intensity [V/m]
D	Electric flux density [C/m^2]
ρ	Electric charge density [C/m^3]
ε	Electric permittivity [F/m]
μ	Absolute permeability[H/m]
$μ_0$	Permeability in free space[H/m]
$μ_r$	Relative permeability
σ	Conductivity [S/m]
ξ	Magnetic charge factor depends on shape of crack
$ξ_0$	Maximum magnetic charge factor
α	Angle between the tangential line of the profile of a crack.
β	Angle between the eddy current and X-axis
δ	Skin depth
f	Operating frequency

초 록

비파괴 평가를 위한 교류형 자기카메라의 다이폴 모델 기반 시뮬레이션 기법에 관한 연구

비파괴평가는 항공기, 원자력발전소, 석유화학플랜트 및 철도 등과 같은 대형기기 구조물에 내재한 결함을 검출하고, 정량적으로 평가하기 위한 중요한 수단이다. 비파괴평가를 위해서는 결함주변에서 발생하는 물리량의 변화에 대한 시뮬레이션이 필요하며, 이를 위하여 지금까지 유한요소해석법과 수치해석법이 개발되었다. 이러한 시뮬레이션기법은 실제 비파괴검사시스템을 이용한 방법에 비하여 쉽고, 빠르며, 경제적이면서도, 신호를 예측할 수 있으므로 꼭 필요한 기술 중 하나이다. 또한, 실제 비파괴검사시스템을 설계할 때, 필요한 유용한 정보를 사전에 확보하여 해당 시스템을 최적 설계할 수 있다. 그러나, 지금까지의 시뮬레이션은 컴퓨터의 대형 용량은 물론 계산속도를 높이기 위한 하드웨어적인 성능의 우수성도 요구되었으며, 그럼에도 불구하고 시뮬레이션에 소요되는 시간이 길다는 단점이 있었다. 본 연구에서는 이러한 용량, 성능, 속도와 같은 단점을 극복하기 위하여, 다이폴모델을 이용한 시뮬레이션 기법을 제안한다. 특히, 비파괴검사시스템의 하나인 교류형 자기카메라에 의한 결함 평가를 시뮬레이션의 대상으로 하였다. 도전성 시험편의 결함 주변에 발생하는 교류자기장의 분포를 영상화하여, 결함의 형상 및 크기를 예측하였으며, 단일균열 및 다중균열을 동시에 시뮬레이션할 수 있도록 하였다. 시뮬레이션은 평판형 시험편에 직사각형, 삼각형, 타원형, 스텝형의 단면형상을 가지는 결함을 대상으로 하였다. 또한, 배관형 시험편의 경우에는 내면 및 이면결함을 대상으로 시뮬레이션하였다. 다이폴모델을 이용한 시뮬레이션 기법의 유용성과 성능을 검증하기 위하여, 유한요소해석에 의한 시뮬레이션 및 교류형 자기카메라에 의한 실험결과를 비교하였다.

레 민 후이

지도교수 : 이 진 이

조선대학교 일반대학원 제어계측공학과

ABSTRACT

Simulation Method based-on Dipole Model for the AC-type Magnetic Camera in the Nondestructive Testing and Evaluation

Nondestructive evaluation (NDE) is an important methodology for quantifying cracks in engineering structures such as airplane, nuclear power plants, petroleum and gas systems, and railways. Several simulation methods such as finite element method and analytical method have been developed for using in NDE. The simulation is necessary because it is easy, signal predictable, fast and economic when compare with a real NDE system. Moreover, the simulation is useful in the design state of NDE systems because it helps to predict signal, optimize the system factor such as number of sensor, coiling method and size. Among many advantages of the simulation methods, they have weak points of slow simulation, taking much computer resource and complication of implementation. This study proposes an improvement of dipole model method for simulation of magnetic camera in NDE. The method is used to simulate an alternating magnetic field around cracks on a conductive specimen and to estimate the shape and volume of the crack. Several crack shapes such as rectangular, triangular, elliptical, circular, and stepped sectional shape in plate specimen, and hole-type inner and outer diameter cracks in a pipe are simulated in this study. Single crack or multiple cracks can be simulated in one simulation. The dipole model method enables faster and simpler simulation and evaluation of crack size than the conventional simulation methods such as the finite element method. The dipole model performance is verified by comparing its simulation results with simulation results of a finite element method and experimental results obtained using an AC-type magnetic camera. The shape and volume of crack are evaluated using the simulation methods and the experimental method in the study.

Le Minh Huy

Advisor: Prof. Jinyi Lee, PhD

Dept. of Control and Instrumentation Eng.,

Graduate School of Chosun University.

CHAPTER 1 INTRODUCTION

This chapter introduces some widely used techniques in nondestructive testing (NDT) and evaluation (NDE) methodology. The very basic concept and principle of each technique will be presented. Several techniques are penetrant testing (PT), radiography testing (RT), ultrasonic testing (UT), and electromagnetic testing (EMT). The thesis concentrates on the electromagnetic testing methodology in which the magnetic particle testing (MT), magnetic flux leakage testing (MFLT) and eddy current testing (ECT) methods are mostly applied in practical. Among various types of EMT system, magnetic camera has been developing recently. The briefly principle and application of magnetic cameras will be presented. For simulation of EMT systems, three kinds of simulation methods have been using as numerical method, analytical method and dipole model method. The development, advantages and disadvantages of these simulation methods will be presented in this chapter. Also, the objective of the thesis with a target of improvement of dipole model method for simulation of magnetic cameras will be proposed in here.

1.1. Nondestructive Testing and Evaluation

Nondestructive testing (NDT) methodology is the process of inspecting, testing materials without destroying or harmful to the material. Nondestructive Evaluation (NDE) methodology is known as a higher level methodology than the NDT. NDE is not only inspecting but also quantitative evaluation of material characteristics and flaws size and shape. The NDT and NDE (NDT&E) are both used to ensure the integrity, safety and maintenance of engineering systems. In the heavy industries such as airplane, power generation, automotive and railway, NDT&E are used widely and become more and more important, nowadays. There are a lot of NDT&E methods, some of the most used are penetrant testing (PT), neutron radiographic testing (NRT), thermal/infrared testing (IR), ultrasonic testing (UT), radiographic testing (RT), and electromagnetic testing (EMT). This section briefly summarizes some NDT&E methods, their basic operating principle and characteristics.

1.1.1. Penetrant Testing (PT)

The basic principle of penetrant testing (PT) is when a visible or fluorescent dye is applied to the surface of inspecting objects; it penetrates into the flaws on the surface. When the liquid in the surface is removed, the some liquid is remained inside the flaws. With fluorescent dyes, ultraviolet light is used to make the fluorescent brightly, or with visible dyes, a color contrast between the penetrant makes easy to see the flaws [1]-[3].

Fig. 1-1 shows four basic steps in PT method [4]. The first step, a penetrant material is applied in the surface of inspecting objects, waiting for a specific period of time. The second step, carefully clean the penetrant material on the surface. Then, a light coating of developer is then applied to the surface and given time to allow the penetrant from any flaws to seep up into the developer, creating a visible indication. The last step, inspector indicates flaws by visual the contrast light from the remained penetrant material in flaws.
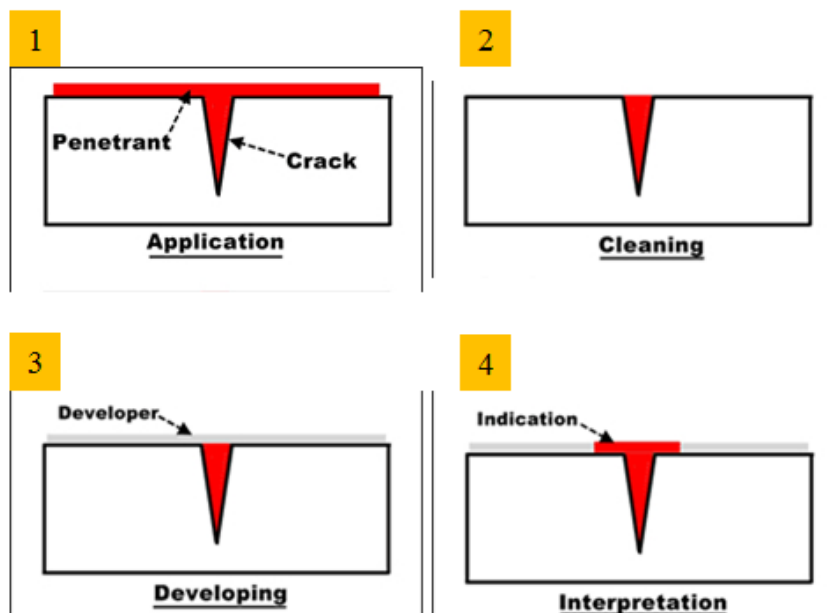
Fig. 1-1 Four basic steps of Penetrant Testing.

The PT method is a simple method, and not required much time for training the inspector. However, it is used only for detecting surface flaws. It also required waiting time, supplied penetrant material, cleaning inspecting material surface and not quantitative flaws.

1.1.2. Radiographic Testing (RT)

This technique involves using penetrating gamma- or X-ray radiation on inspecting materials. The radiation passes through the object being inspected, and captured by a recording film or detector placed against the opposite side of that object [4]-[9]. The material thickness and density changes cause of flaws are indicated as lighter or darker areas on the detector.

Fig. 1-2 shows a sample of RT for an object with different thickness and discontinuity of material [5]. The changes of intensity of image indicate the discontinuity and thickness changes. The RT systems are expensive, complicated, and require specific precaution to avoid radiation hazards.
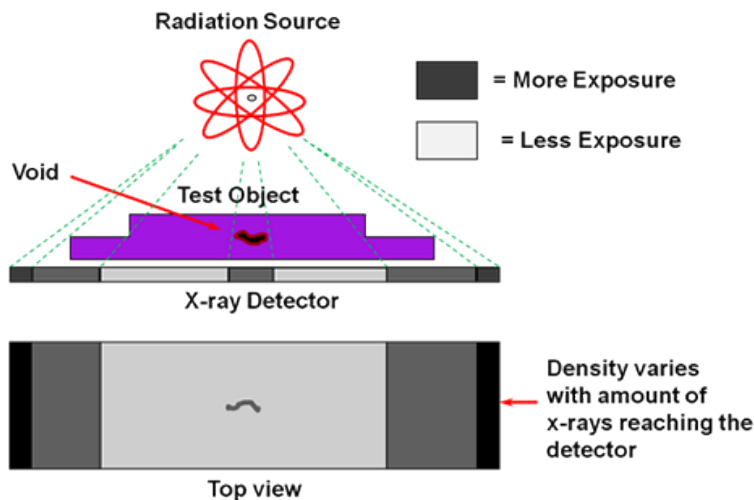
Fig. 1-2 A sample of Radiographic Testing

1.1.3. Ultrasonic Testing (UT)

In Ultrasonic testing technique, high-frequency acoustic elastic waves are transmitted into a material to detect flaws or changes of material properties [10]-[13]. The most commonly used UT technique is pitch-catch method and pulse echo method. The pulse generates a longitudinal wave or transverse wave (shear wave) travels in inspecting object. The sound wave is either transmitted to another transducer (pitch-catch, Fig. 1-3 (a)) or reflected back to the original transducer (pulse-echo, Fig. 1-3 (b) [14]. The distance from the discontinuity is calculated by travel time and speed of the sound in the inspecting object. The frequencies of sound used in UT are usually over than 1MHz that cannot be heard or difficult to travel through the air. The lower frequencies have greater penetrating power but less sensitivity. Fig. 1-4 shows a simulation of signal-time response from ultrasonic testing using pulse-echo method [15].
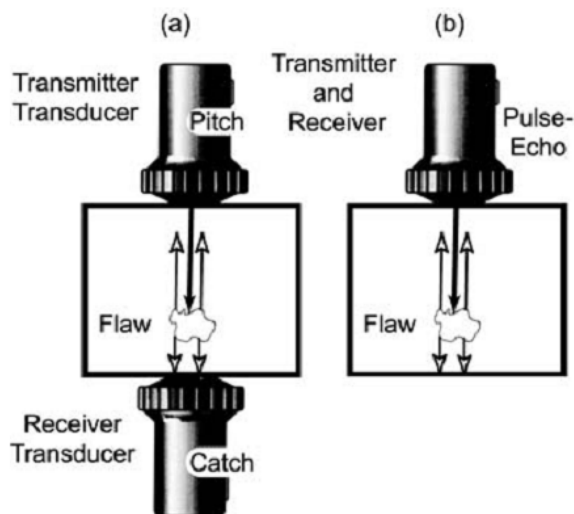
Fig. 1-3 Two basic methods for transmitting and receiving ultrasound: (a) separate transducers, and (b) single transducer [14].
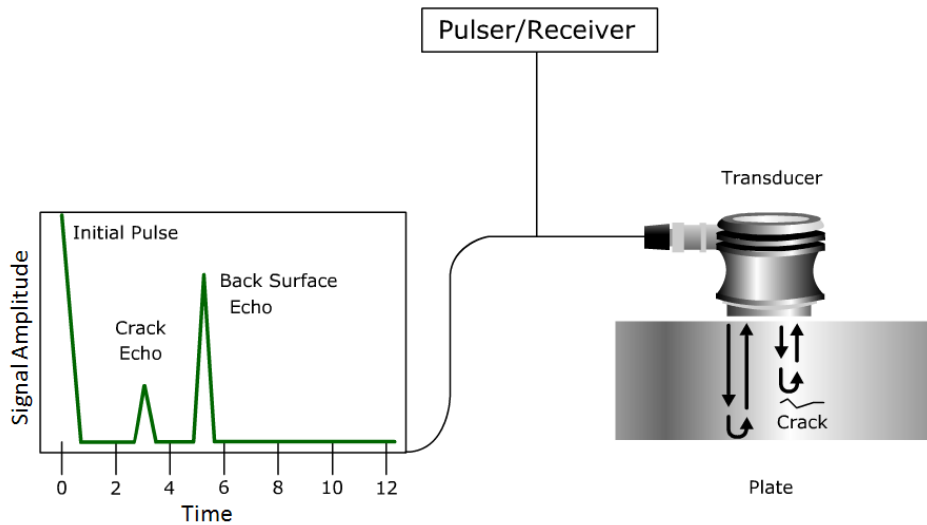
Fig. 1-4 A simulation of signal-time response from ultrasonic testing using pulse-echo method [15].

The UT is widely used in aircraft, pipeline and railway systems because of its high performance and reliability. The UT has many advantages such as sensitivity to the both surface and subsurface of flaws, high depth of penetrant, single-sided access is possible when using pulse-echo method, highly accurate and evaluation of flaws. However, it also include some limitation such as surface must be accessible to transmit ultrasound, requires coupling medium to promote sound to testing object, required skill and training for inspector, and difficult to use for coarse grained materials (low sound transmission) such as cast iron.

1.1.4. Electromagnetic Testing (EMT)

There are many methods are used in electromagnetic testing such as: magnetic particle testing (MT), magnetic flux leakage testing (MFLT), eddy current testing (ECT, pulse-ECT). The basic principle of EMT is the magnetic field is distorted due to the existence of flaws in metal materials. Using various kinds of magnetic sensors or magnetic particles, the distorted fields are measured, evaluated or observed. The present of flaws in metal object could be inspected and quantitative such as size and shape.

- 5 -

The EMT has many advantages such as highly accurate, reliability, very fast and quantitative flaws size and shape. It is not necessary to use coupling medium as in UT. However, the most limitation of EMT is only can be used in metal material which have high permeability or high conductivity. It is unable to use in plastics or woods.

Magnetic particle testing (MT) is used to inspect surface or very near surface defects [16]-[18]**Error! Reference source not found.**. The inspecting object is magnetized with a DC magnetic field. If there is any surface or near surface defects in the object, the defects will create a magnetic flux leakage field. When magnetic particles such as iron particles are applied to the surface, the particles will be attracted and cluster at the magnetic flux leakage field. Thus, the defects will be inspected. The MT is only can estimate the length of defect; otherwise, the depth cannot be estimated. Fig. 1-5 shows the basic principle of MT [4], and Fig. 1-6 shows a sample of MT method inspecting cracks at a fastener hole [19].
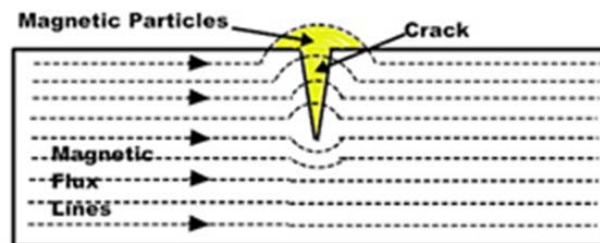
Fig. 1-5 Principle of magnetic particle testing [4].

Fig. 1-6 Magnetic particle wet fluorescent indication of cracks in a fastener hole [19].

Magnetic flux leakage testing (MFLT) is widely used in ferromagnetic material which has high permeability [20]-[25]. Fig. 1-7 shows the basic principle of MFLT [26]. When a magnetic flux from a magnetizer is supplied to the specimen, a magnetic flux leakage (MFL) is produced due to present of cracks. The MFL is measured by various kinds of magnetic sensors such as Hall sensor, giant magnetoresistance sensor (GMR) and anisotropic magnetoresistance sensor (AMR). The quantitative of cracks such as size and shape could be estimated by the measured signal from magnetic sensor. The performance of MFLT system highly depends on the sensitivity of magnetic sensor, size and resolution of sensor, and lift-off which is distance from sensor to the surface of specimen.
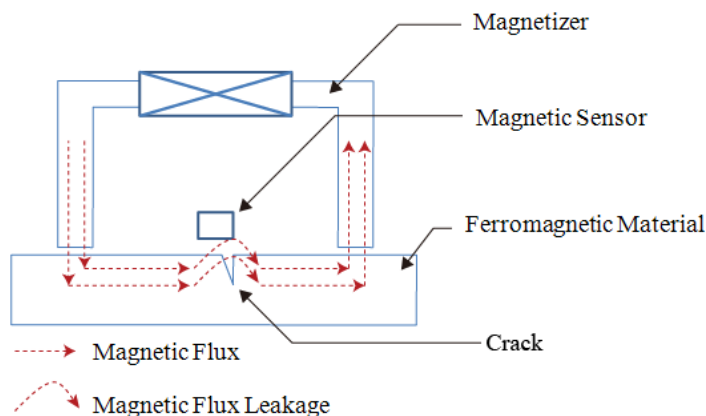
Fig. 1-7 Principle of magnetic flux leakage testing [26].

Eddy current testing (ECT) has been developed for a several decades to inspect and quantitative cracks in conductive materials such as in aircraft structures and steam generators [27]-[30]. The basic principle of ECT is shown in Fig. 1-8 [31]. When a coil with AC input current is put close to a conductive material, an eddy current is induced in the material. If there is a crack in the material, the eddy current is distorted and produces a magnetic field to the coil. Thus, the impedance of the coil is changed. By measuring the changes of impedance of the coil, the crack could be inspected. We can use single coil or double coil in which one is primary coil, another is sensing coil. Furthermore, magnetic

sensors could be used to measure the changes of magnetic field. In this case, magnetic sensors is usually put in the center of the coil and theirs saturation is taken into account.
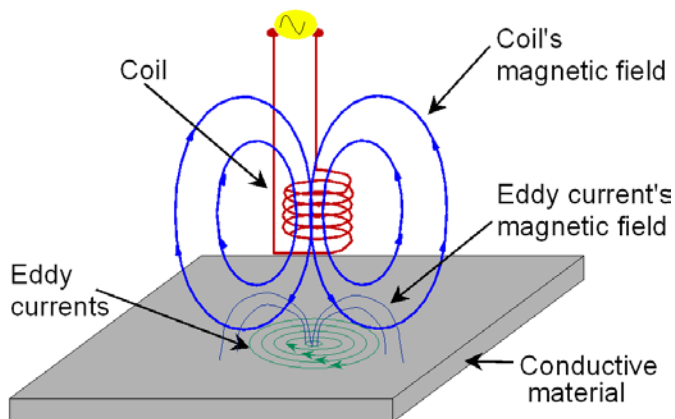
Fig. 1-8 Principle of eddy current testing [31].

Fig. 1-9 shows an impedance plane of ECT [32]. ECT signal is specific sensitive to the lift-off. And for different kinds of material, the response is also quite different. For example, when the coil is moved from the air near to a conductive material such as aluminum, the resistance of the coil increases but the reactance decreases. Because the eddy current is induced in the conductive material takes energy of the coil as the resistance of the coil increases; otherwise, the eddy current produces opposite magnetic field to the coil that reduces magnetic field in the coil, then the reactance of the coil is reduced. If there is a crack in the aluminum, the fewer eddy current is formed. Thus, the resistance will go back down and reactance will go back up. For a magnetic material such as steel, the resistance of the coil keeps same behavior with conductive material but the reactance increases. Because the magnetic material concentrates the magnetic field of the coil, that increase the inductance of the coil. If there is a crack in the steel, the lower magnetic field concentrates into the steel and the resistance go back down. The reactance will go back up like the behavior in the aluminum material.
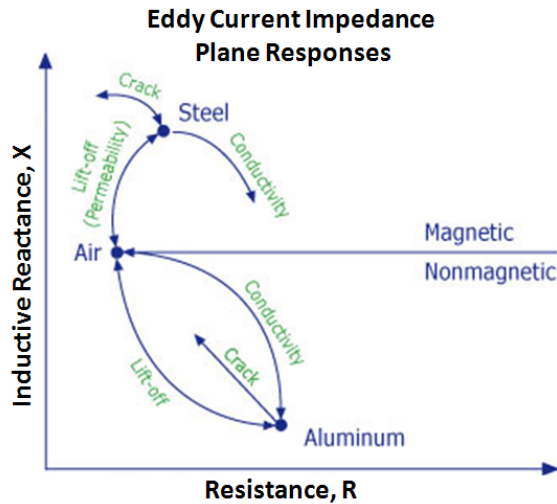
Fig. 1-9 Impedance plane of ECT [32].

1.2.   Magnetic Camera

Magnetic camera has been being developed by Lee et al. [32]-[49] since the last decades. The general schematic of magnetic camera is shown in Fig. 1-10. It has a magnetic source, magnetic lens, magnetic sensors, A/D converter, Interface and a computer with software. The term "**Magnetic Camera**" is used because its components are similar to the optical camera. Fig. 1-11 shows the corresponded components of magnetic camera with optical camera. Instead of visual the light of optical camera, magnetic camera visualizes the magnetic field. The magnetic camera has magnetic source corresponding to optical source, magnetic lens corresponding to optical lens, magnetic sensor (Hall, GMR) corresponding to image sensor (CCD, CMOS), and image processing & display.
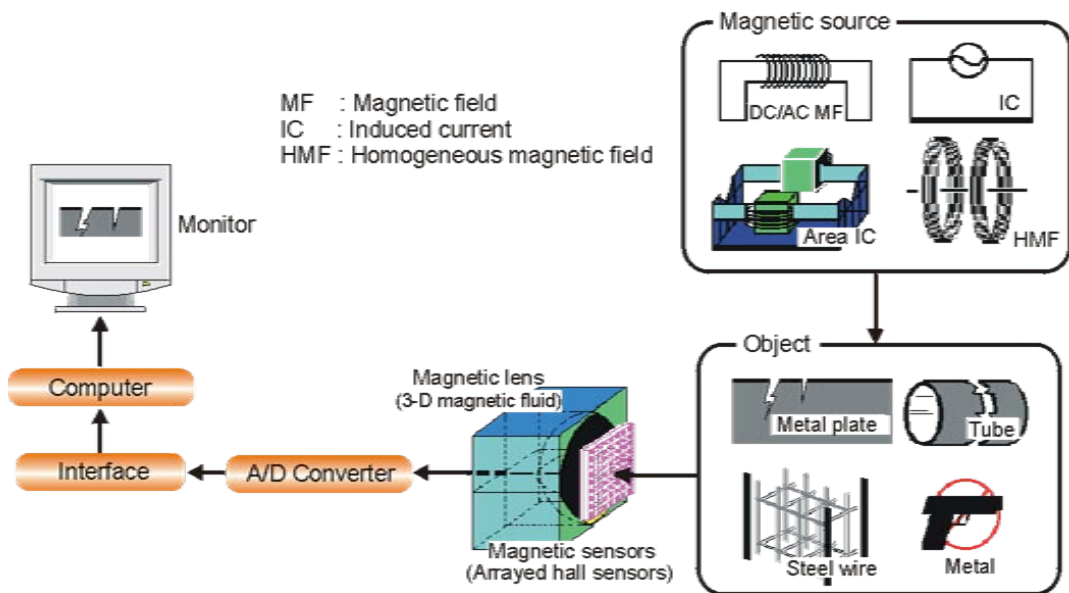
Fig. 1-10 General schematic of magnetic camera

Fig. 1-11 Corresponded components of magnetic camera with optical camera.

Based on magnetic source types, magnetic camera is classified in two types: DC-type and AC-type. The DC-type magnetic camera is used to visualize a magnetic field created by direct current (DC) or a permanent magnet. A lower frequency than 300 Hz also can be visualized by using DC-type magnetic camera due to high speed imaging circuits. The DC-type magnetic camera is used in MFLT. The AC-type magnetic camera can visualize magnetic field at several ten kHz due to response frequency domain of magnetic sensor. However, the AC-type magnetic camera can measure only the root-mean-square of

magnetic field. It is different with the conventional ECT methods, in which amplitude and phase of magnetic field or impedance plane is measured. The magnetic camera has some advantages such as: high resolution due to small size of magnetic sensor, real-time imaging, easy operating, and easy analyzing data. The magnetic camera have been applied in the train wheel system for inspect surface defects in the wheel, multilayer structure in aircraft for inspect far-side corrosion, piping system, etc. The crack size, position and shape could be estimated.

1.3.   Simulation of Electromagnetic Testing

Simulation of electromagnetic testing is especially used for design NDT system, prediction of measurement signal, quantitative cracks size and shape (inverse problems). There are three categories of electromagnetic simulation methods: numerical simulation, analytical simulation and dipole model, as classified in Fig. 1-12.
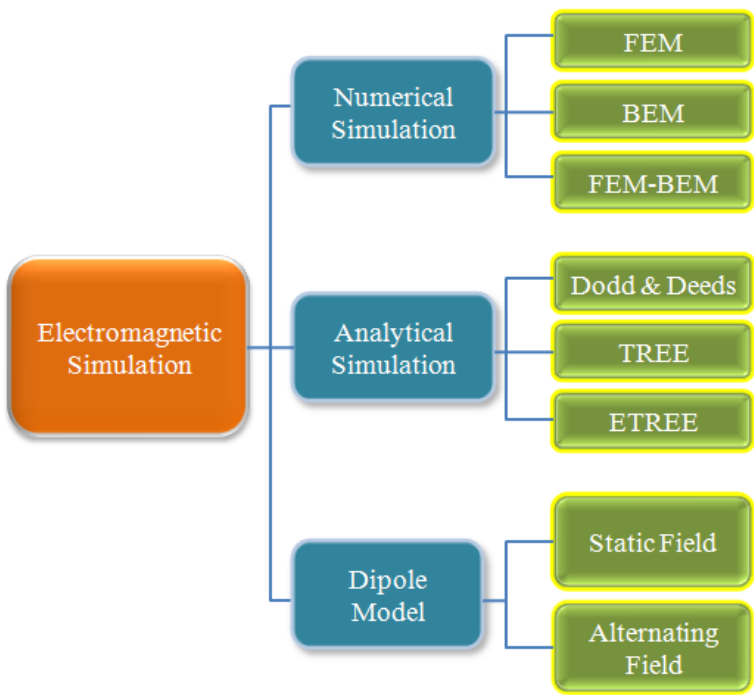
Fig. 1-12 Categories of electromagnetic simulation methods

1.3.1. Numerical Simulation

Numerical simulation solves the electromagnetic problems by Partial Differential Equations (PDEs). It is flexible to model complex geometrical components and nonlinearity material. However, it is necessary to discrete region of components to small element making time-consuming and low accuracy. There are several methods such as Finite Element Method (FEM) [50], Boundary Element Method (BEM) [51], and Hybrid Method which combines FEM and BEM [52]-[53]. The FEM is started with Finite Difference Method (FDM) which was introduced by Dodd and Deeds [54] in the simulation of eddy current. The FDM was then replaced by FEM because of limitation in complicated geometries. The BEM was developed after the FEM with application of boundary condition that limits the simulation geometries. And then, the hybrid methods which combine FEM with BEM were developed to overcome the limitation of FEM and BEM. Several researchers have developed FEM over the years. Takagi et al. [55]-[56] used magnetic vector potential and an edge-based FEM to simulate a multi-coil probe. They also used a quasi-static form of Maxwell's equations for time harmonic fields to simulate a remote field probe. Gotoh et al. [57] used a 3-D edge-based hexahedral nonlinear FEM to simulate differential search coils. Xin et al. [58] used reduced magnetic vector potential to simulate a rotated magnetic field. Nowadays, there are a lots of commercial FEM software such as: COMSOL [59], MAGNET [60], and ANSYS [61]. They have easy-to-use graphical interface, automatic meshing and computing algorithms, and multiple post-processing for display and analysis results. In this thesis, I will introduce and use ANSYS software to simulate the EMT problems.

1.3.2. Analytical Simulation

Analytical simulation provides a "closed-form" solution to the governing partial differential equations which are derived from four Maxwell's equations. It provides a fast and accurate solution than numerical simulation. However, it is limited in complicated geometries. The Analytical simulation started with simulation of eddy current by Dodd and Deeds [54] in 1960. It has disadvantage of the presence of infinite integrals in the

Collection @ chosun

calculation, thus, it is time-consuming. The Truncated Region Eigenfunction Expansion (TREE) method was then developed by Theodoulidis [62]-[63] to apply in finite region of interest. The TREE method has been applied to several eddy current problems including inspection of a right angled conductive wedge [64], edge of a conductive plate [65], and finite length coils and rods [66]. The extended TREE method then developed to simulate magnetic field for a magnetic-sensor-based ECT system. It was applied to simulate magnetic field in multilayered structures [67].

1.3.3. Dipole Model

Dipole Model was categorized in static field model (for MFLT) and alternating field model (for ECT). Dipole model was first proposed by Zatsepin and Shcherbinin [68] (1966) to model magnetic flux leakage (MFL) of surface cracks. When a static magnetic field is applied to a specimen with a crack, the crack is considered to be filled by dipoles with dipole moments oriented opposite to the direction of the applied magnetic field. The model enables analysis MFL from a simple crack with rectangular cross-section by placing a point or line dipole on the crack wall. Shcherbinin and Pashagin [69] (1974) derived analysis for the field of a plane dipole to represent the MFLT field of a 3-D rectangular cross-section crack. However, they only applied this method for studying of maximum amplitudes of line scan signals of z- and y-components along the symmetry axis of the crack (let assume in Descartes coordinate, x-axis indicates the length of crack, y-axis indicates the width of crack, and z-axis indicates the depth of crack). Forster [70] (1986) derived the model with induced surface charge density as a function of applied field, ferromagnetic permeability, and defect sizes for 2-D rectangular cross-section. And, in the same time, Edward and Palmer [71] by solving Laplace equation for ellipsoidal cavity in a ferromagnet, derived analogous results for 2-D cracks with semi-elliptical cross-section. In 1998, Mandal and Atherton [72] used experiment for studying the effect of line-pressure-induced hoop stress on line-scan MFL of a pit crack, and compared with simulation models of Zatsepin-Scherbinin and Edwards-Palmer.

In early of the last decades, dipole model was taken into account for quantitative evaluation of shape and size of simple geometrical cracks. Minkov et al. [73]-[74]

- 13 -

proposed that the magnetic charge density varies along the depth of crack; it is higher at the defect tip compared to the defect mouth. They modeled this variation linearly for 3-D crack with rectangular cross-section. The size and shape of 3-D cracks were then estimated by least square estimation between experiment and simulation results [75]. Mandache and Clapham [76] used dipole model with uniform surface magnetic charge density to model MFL field of a single and multiple cylindrical pit defects. The length of crack was estimated by using location of peaks of radial MFL component along the center of the crack. Dutta et al. [77]-[78] used dipole model for a 3-D cylindrical hole-type crack. Three components of MFL were taken into account. They verified the simulation by experiment with scanning of Hall sensor elements. The radius of crack was estimated by peak-to-peak distance of z-component signal for a range of lift-offs.

Lee et al. [79]-[81] used dipole model to simulate magneto-optical imager with horizontal and vertical direction of external magnetic field. The dipole model was verified by experiment of magneto-optical imager and FEM. Several types of 3-D crack shape such as rectangular, triangular, stepped cross-section were taken into account. The volume of crack was estimated by using optical intensity. Le et al. [82]-[83] extended the simulation for various directions of crack and multiple cracks. After that, they developed the first model for alternating magnetic field, which was used to simulate magneto-optical eddy current imager (MOI) [82], [46] (2011). The dipole magnetic charges were assumed to appear also in the tip surfaces of crack, not only in the wall surfaces as in the MFL. The distribution of magnetic dipoles depends on distribution of eddy current instead of magnetic flux leakage as in the MFL. The magnetic charge density was exponentially decreased in depth of crack by the same way with eddy current intensity in skin effect. In the simulation results compared with the MOI results, only 3-D rectangular cross-section cracks with a change of depth was taken into account. However, the MOI has only one bit data (0-white color, 1-black color). Thus, the quantitative evaluation of crack is limited.

1.4.   Objectives of Thesis

This thesis proposes the developments of dipole model for simulation of magnetic camera in the EMT. The thesis focuses on simulation of alternating magnetic field which is an extension of the previous dipole model. The dipole model will be improved in geometry of specimen and crack shape and performed for simulation of scanning state of a magnetic camera. The dipole model for various crack shapes in a flat specimen such as rectangular, triangular, elliptical, stepped, and circular cross-section will be presented. Simulation of inner and outer diameter (ID and OD) hole-type cracks in a small-piping system such as heat exchanger also will be presented. Simulation of scanning state of a bobbin-type magnetic camera will be performed for ID and OD hole-type cracks in a small-piping system. The dipole model results is compared with FEM using ANSYS commercial software and verified by experiments of magnetic cameras. The advantages of dipole model compared with FEM such as faster simulation time, easy setup and operating, and more accurate will be presented. Furthermore, quantitative evaluation of crack size and shape also will be done using dipole model.

CHAPTER 2 FINITE ELEMENT METHOD AND PREVIOUS DIPOLE MODEL METHOD

2.1.   Electromagnetic Field

This section briefly presents the general differential form and integral form of Maxwell's equations. The meaning of each Maxwell's equation is explained and be demonstrated by geometric representation for easy understanding. Three constitutive equations are also presented, which help to complete the finite form of Maxwell's equations. The integral form of Maxwell's equations is useful to be applied in the numeric calculation. In the next part of the section, the skin effect is derived from Maxwell's equations. The skin effect is known as the most widely used effect in the Nondestructive testing and Evaluation. In the final parts, two common methods for simulation of static magnetic field (MFLT) and dynamic magnetic field (ECT) will be presented, which are scalar potential magnetic field and vector potential magnetic field methods.

2.1.1.   Maxell Equations

Electromagnetic (EM) is described by four Maxell's equations and the constitutive relations. The four Maxell's equations are gathering of the EM phenomena were established by other scientists such as Ampere (1775-1836), Gauss (1777-1855), Faraday (1791-1867) and Lenz (1804-1865). There were some incompatibilities on the formulations. Maxell (1831-1855) introduced an additional displacement current term to the Ampere's law. The additional term shows the prediction of light to propagate as electromagnetic waves. The syntheses of the EM are just in a simple formalism with four equations Eq. (2-1)-(2-4) [84]-[87].

$$\text{rot}\mathbf{H} = \mathbf{J} + \frac{\partial \mathbf{D}}{\partial t} \qquad \text{(Maxell-Ampere's law)} \qquad (2\text{-}1)$$

$$\text{div}\mathbf{B} = 0 \qquad \text{(Gauss' law - magnetic)} \qquad (2\text{-}2)$$

$$\text{rot}\mathbf{E} = -\frac{\partial \mathbf{B}}{\partial t} \qquad \text{Faraday's law} \qquad (2\text{-}3)$$

$$\text{div}\mathbf{D} = \boldsymbol{\rho} \qquad \text{(Gauss' law-electric)} \qquad (2\text{-}4)$$

The electrical continuity equation can be derive by applying divergence on the both sides of Eq. (2-1), we have:

$$\text{div}(\text{rot}\mathbf{H}) = \text{div}\mathbf{J} + \text{div}\frac{\partial \mathbf{D}}{\partial t} \qquad (2\text{-}5)$$

Using the mathematical of divergence and rotational, for any vector $\mathbf{H}$ we have: $\text{div}(\text{rot}\mathbf{H}) = 0$, Eq. (2-5) becomes:

$$0 = \text{div}\mathbf{J} + \frac{\partial}{\partial t}\text{div}D \qquad (2\text{-}6)$$

Utilizing Eq. (2.4), we have continuity equation:

$$\text{div}\mathbf{J} = -\frac{\partial \boldsymbol{\rho}}{\partial t} \qquad (2\text{-}7)$$

The graphic demonstrates the Eq. (2-7) is shown in Fig. 2-1. The accumulate charge appears in volume V leads to different current between output and input. In general, the term $\partial\boldsymbol{\rho}/\partial t$ is zero and therefore we obtain $\text{div}\mathbf{J} = \mathbf{0}$. That means the conduction current is conservative. This does not happen when there is an accumulation of charges in the device, $\partial\boldsymbol{\rho}/\partial t \neq 0 (I_1 \neq I_2)$. In fact, in practically all electromagnetic devices, the current injected into the device is equal to the current leaving it $(I_1 = I_2)$ [84].
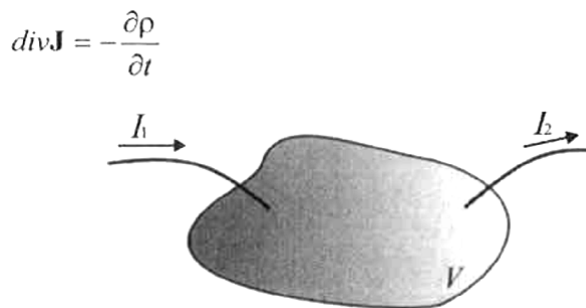
Fig. 2-1 Accumulate charge in volume V due to nonzero divergence of current density.

The first equation (2-1) is called Maxwell-Ampere's law. A rotational magnetic field can create a split into induction current ($\mathbf{J}$) and a time variation of electric flux density ($\partial\mathbf{D}/\partial t$). Maxwell (in 1862) added the last term in the equation (2-1). This term enabled to derive the electromagnetic wave equation in later 1865. It explains that the light is an electromagnetic wave. If there is no electric flux density or electric flux density is constant

in time. The term $\partial \mathbf{D} / \partial t$ is zero. Thus, we have rot$\mathbf{H} = \mathbf{J}$. The geometric of the H and J is demonstrated in Fig. 1-9; the H and J are connected by a rotational relationship (rot) [84].
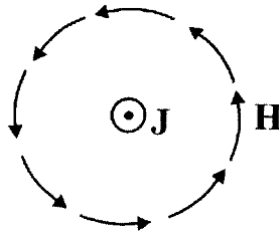
Fig. 2-2 Relation between induced current density and magnetic field intensity

The second equation (2-2) is called Gauss' law for magnetic field. The magnetic flux is conservative. The total magnetic flux entering to a volume is equal to the magnetic flux leaving the volume. Using Stokes' theorem, existing vector potential A so that $\mathbf{B} =$ rot$\mathbf{A}$. The vector potential A is widely used in the many simulation problems [84].

The third equation (2-3) is called Faraday's law. The changes of magnetic field in time induce an electromagnetic field around magnetic flux. This law combined with the Maxwell-Ampere's law, we see the interaction between magnetic field and electric field that is called electromagnetic field. The geometry relationship of Eq. (2-2) is shown in Fig. 2-3 [84].
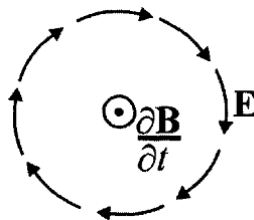
Fig. 2-3 Relation between derivative of magnetic flux density and electric field intensity

The forth equation (2-4) is called Gauss' law for electric field. The electric flux density is not conservative, that is, the entering and leaving to a volume of electric flux are not equal, as described in Fig. 2-4. The total divergence of electric flux density in a volume is equal to the total electric charge in that volume.
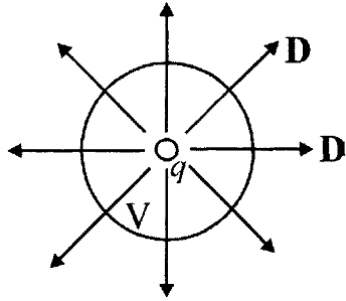
Fig. 2-4 Electric flux of a magnetic charge

2.1.2.   Constitutive Relations

In time-varying fields, only three equations in the five equations (four Maxwell's equations and one continuity equation) are independent. Either the first three equations (2-1)-(2-3), or the first two equations (2-1)-(2-2) with the continuity equation (2-7) can be chosen as such independent equations. Thus, the number of equation is less than the number of unknowns. With the constitutive relations, the Maxwell's equations become definitely.

The constitutive relations describe the macroscopic properties of the medium being considered [84]-[87]:

$$\mathbf{D} = \varepsilon \mathbf{E} \tag{2-8}$$

$$\mathbf{B} = \mu \mathbf{H} \tag{2-9}$$

$$\mathbf{J} = \sigma \mathbf{E} \tag{2-10}$$

where the permittivity (ε), permeability (μ) and conductivity (σ) are tensors for anisotropic media and scalars for isotropic media. For inhomogeneous media, they are functions of position.

2.1.3.   Integral Form of Maxwell's Equations

The four Maxwell's equations establishes generally phenomenon in the electromagnetic field. The short notations give the simple and easy understand the phenomenon. However, in practical, we should derive another form as integral form to solve the electromagnetic problems. This section summaries a simple and briefly way to

- 19 -

transform the four general Maxwell's equations to integral equation, which was introduced in many text book relate to electromagnetic field [84]-[87], [88]. This way is based on the divergence theorem and Stokes's theorem.

Eq. (2-1): $\text{rot}\,\mathbf{H} = \mathbf{J} + \partial\mathbf{D}/\partial t$. For the constant or no electric flux density: $\text{rot}\,\mathbf{H} = \mathbf{J}$. For the flux through an open surface $\mathbf{S}$, in both sides we have:

$$\int_S \text{rotH}\cdot dS = \int_S \mathbf{J}\cdot dS$$

and using Stokes' theorem with L(S) is close line delimiting of surface S.

$$\int_S \text{rot}\mathbf{H}\cdot d\mathbf{S} = \int_{L(S)} \mathbf{H}\cdot d\mathbf{l}$$

Finally, we have:

$$\oint_{L(S)} \mathbf{H}\cdot dl = \mathbf{I} \qquad (2\text{-}11)$$

The second equation: $\text{div}\mathbf{B} = 0$. Take integral in a volume V we have

$$\int_V \text{div}\mathbf{B}dV = 0$$

Using divergence's theorem, we have:

$$\oint_{S(V)} \mathbf{B}\cdot d\mathbf{S} = \mathbf{0} \qquad (2\text{-}12)$$

It shows that the total magnetic flux density in a close surface S(V) delimiting of volume V is conservative.

The third equation: $\text{rotE} = -\partial B/\partial t$. Take integral in an open surface S, we have:

$$\int_S \text{rot}\mathbf{E}\cdot d\mathbf{S} = -\int_S \frac{\partial \mathbf{B}}{\partial t}\cdot d\mathbf{S}$$

Using Stokes' theorem, we have:

$$\oint_{L(S)} \mathbf{E} \cdot \mathrm{dl} = -\int_S \frac{\partial \mathrm{B}}{\partial t} \cdot \mathrm{d}\mathbf{S} = -\frac{\mathrm{d}}{\mathrm{dt}} \int_S \mathbf{B} \cdot \mathrm{d}\mathbf{S} = -\frac{\mathrm{d}\emptyset}{\mathrm{dt}}$$

Finally, we have:

$$\int_{L(S)} \mathbf{E} \cdot \mathrm{dl} = -\frac{\mathrm{d}\emptyset}{\mathrm{dt}} \tag{2-13}$$

It shows that the changes of magnet flux in an open surface induce electric field intensity in the close line delimiting that surface (Faraday's law).

The last equation: div$\mathbf{D}$ = ρ. Take integral in a volume V, we have:

$$\int_V \mathrm{div}\mathbf{D}\mathrm{dV} = \int_V \rho \, \mathrm{d}\mathbf{V}$$

Using divergence theorem, we have:

$$\oint_{S(V)} \mathbf{D} \cdot \mathrm{d}\mathbf{S} = \mathbf{q} \tag{2-14}$$

It shows that the electric flux density through a closed surface S(V) is equivalent to the total electric charge in the volume V.

Summary the integral form of Maxwell's equations:

$$\oint_{L(S)} \mathbf{H} \cdot \mathrm{dl} = \mathbf{I} \tag{2-11}$$

$$\oint_{S(V)} \mathbf{B} \cdot \mathrm{d}\mathbf{S} = \mathbf{0} \tag{2-12}$$

$$\int_{L(S)} \mathbf{E} \cdot \mathrm{dl} = -\frac{\mathrm{d}\emptyset}{\mathrm{dt}} \tag{2-13}$$

$$\oint_{S(V)} \mathbf{D} \cdot \mathrm{d}\mathbf{S} = \mathbf{q} \tag{2-14}$$

2.1.4. Skin Effect

From Faraday's law in Eq. (2-3) $\mathrm{rot}\mathbf{E} = -\partial\mathbf{B}/\partial t$, by substituting the constitutive relation for electrical field $\mathbf{J} = \sigma\mathbf{E}$, and constitutive relation for magnetic field $\mathbf{B} = \mu\mathbf{H}$, we have:

$$\frac{1}{\sigma}\mathrm{rot}\mathbf{J} = -\mu\frac{\partial\mathbf{H}}{\partial t}$$

Using rotational for both sides, we have:

$$\frac{1}{\sigma}\mathrm{rot}\,\mathrm{rot}\mathbf{J} = -\mu\frac{\partial}{\partial t}\mathrm{rot}\mathbf{H}$$

Using first equation (2-1) , for low frequency domain, the term $\partial\mathbf{D}/\partial t = 0$, then $\mathrm{rot}\mathbf{H} = \mathbf{J}$, we have:

$$\mathrm{rot}\,\mathrm{rot}\mathbf{J} = -\sigma\mu\frac{\partial\mathbf{J}}{\partial t}$$

Using continuity equation $\mathrm{div}\mathbf{J} = 0$, the term $\mathrm{rot}\,\mathrm{rot}\mathbf{J} = \mathrm{grad}\,\mathrm{div}\mathbf{J} - \nabla^2\mathbf{J} = -\nabla^2\mathbf{J}$

Finally, we have [84]:

$$\nabla^2\mathbf{J} = \sigma\mu\frac{\partial\mathbf{J}}{\partial t} \tag{2-15}$$
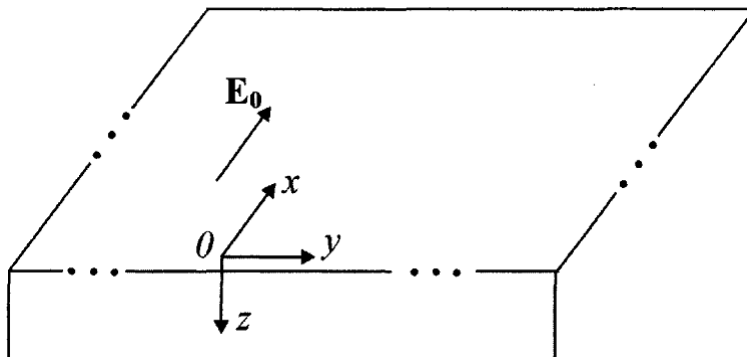
Fig. 2-5 Electric fiend intensity parallel to a semi-infinite conducting material [84].

Eq. (2-15) is Poisson's equation. Note that the obtained equation is used only for linearity and isotropy of materials in which the term $1/\sigma$ are constant with location. It is difficult to obtain the solution in Eq. (2-15). For a simple case as described in Fig. 2-5, sinusoidal electric field intensity $\mathbf{E_o}$ is supplied to the x-direction of a conductor (σ). An electric current density $\mathbf{J_o} = \sigma\mathbf{E_o}$ appeared below the surface, in the conductor. Using complex notation, the current density in conductor is: $\mathbf{J} = \mathbf{J_o}e^{j\omega t}$, where ω is angle frequency of $\mathbf{E_o}$. Then we have:

$$\frac{\partial \mathbf{J}}{\partial t} = j\omega\mathbf{J_o}e^{j\omega t} = j\omega\mathbf{J}$$

The Eq. (2-15) becomes:

$$\nabla^2\mathbf{J} = j\omega\sigma\mu\mathbf{J} \tag{2-16}$$

Since electric field intensity $\mathbf{E_o}$ is in x-direction. Thus, $\mathbf{J}$ has only one component in the x-direction and varies in the z-direction. The differential form of Eq. (2.16) becomes:

$$\frac{\partial^2 J_x(z,t)}{\partial z^2} = j\omega\sigma\mu J_x(z,t) \tag{2-17}$$

Let $\delta = 2/\sqrt{\mu\sigma\omega}$ is called skin depth, we have:

$$\frac{\partial^2 J_x(z,t)}{\partial z^2} - \frac{2j}{\delta^2}J_x(z,t) = 0 \tag{2-18}$$

The solution of Eq. (2.18) is [84]:

$$J_x(z,t) = J_0 e^{-z/\delta}\cos(\omega t - z/\delta)$$

- 23 -
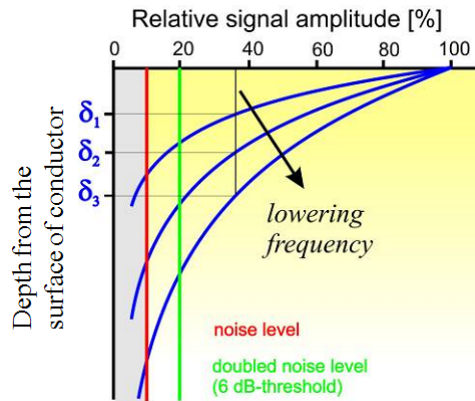
Fig. 2-6 Strength of induced current due to depth from surface of conductor and changes of exciting frequency [88].
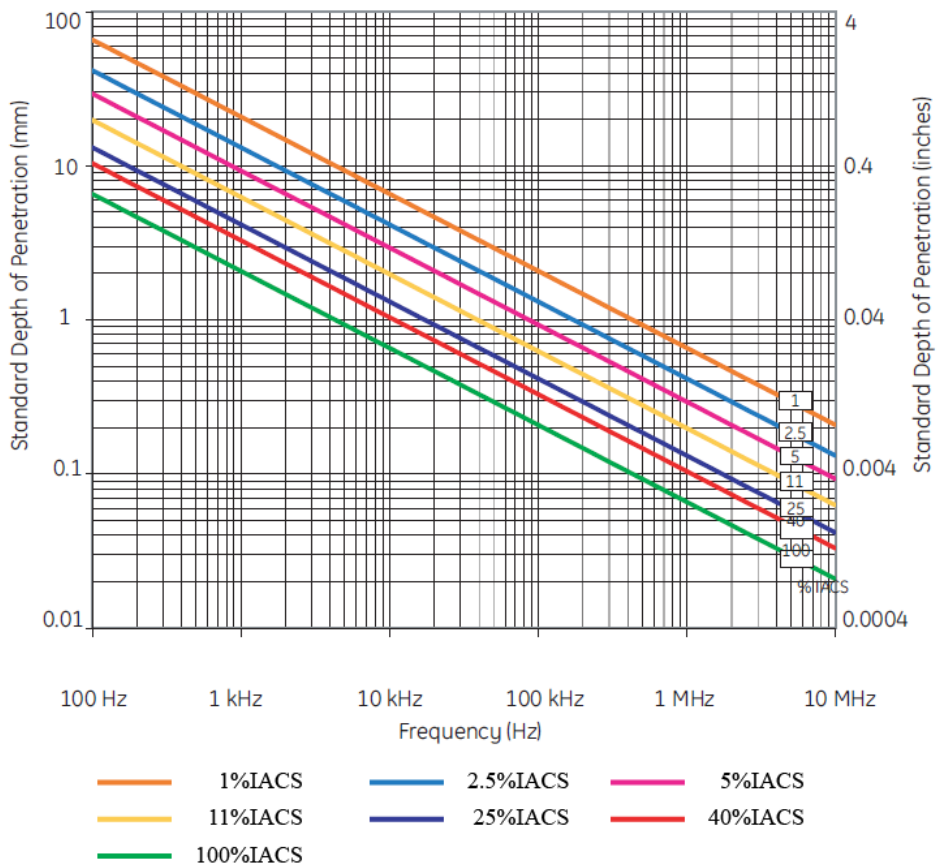
Fig. 2-7 Standard skin depth of materials with exciting frequency [26]

This solution of Eq. (2.18) shows that, the induced current strength exponentially decrease and the phase lag (-z/δ) linearly increase with the depth from the surface of conductor. At the depth of δ from the surface of conductor, the eddy current strength decrease 37% (=e^{-1}). The skin effect depends on permeability and conductivity of material, and frequency of exciter. The higher frequency, the smaller skin depth meanwhile the more concentrate of induced current in the surface of material, as shown in Fig. 2-6 [88]-[90]. The standard skin depths of some conductive materials with exciting frequency are shown in Fig. 2-7 [89], [90], [26]. The conductivity of the materials is shown in Table 2-1. The IACS is International Annealed Copper Standard with conductivity of 58 MSm-1 respect to 100% IACS [26].

Table 2-1 Conductivity of the primary metal [26]

Metal Type	Conductivity	
	%IACS	[MSm^{-1}]
Aluminium (pure)	61	35.4
Aluminium Alloy, 2014-T6	38 ~ 40	22 ~ 23.2
Brass, 70Cu 29Zn 1Sn	25	14.5
Copper (pure)	100	58
Copper-Nickel 70/30	5	2.9
Copper-Nickel 90/10	12.9	6.9
Inconel 600	1.7	0.99
Phosphor Bronze	11	6.4
Stainless steel (300 series)	2.3 ~ 2.5	1.3 ~ 1.5
Titanium	1 ~ 4.1	0.6 ~ 2.4

The skin effect is very useful and widely used in quantitative evaluation in eddy current testing. Due to the changes of signal amplitude according to the exciting frequency or the changes of phase lag of measurement signal, the position of flaws under surface of material is estimated. However, it is also a limitation for eddy current testing. Because the penetration of induced current strength exponentially decreases with the depth from the surface of material, the ECT only can detect surface or near surface flaw.

2.1.5.   Scalar Potential Magnetic Field

Scalar potential magnetic field is applied in static magnetic field problems [84]. Particularly, it is applied in magnetic flux leakage (MFLT) in NDT. In the static magnetic field problems, the magnetic field is constant in time, thus, the induced current **J** in the first Maxwell's equation is zero. Then, we have:

$$\text{rot}\mathbf{H} = 0$$

Therefore, it is possible to define a scalar potential V so that:

$$\mathbf{H} = -\text{grad}V$$

By using magnetic field continuity relation and second Maxwell's equation:

$$\mathbf{B} = \mu\mathbf{H}$$

$$\text{div}\mathbf{B} = 0$$

We have:

$$\text{div}\mu\mathbf{H} = \text{div}\mu(-\text{grad}V) = 0$$

which can be written as [84]:

$$\frac{\partial}{\partial x}\mu\frac{\partial V}{\partial x} + \frac{\partial}{\partial y}\mu\frac{\partial V}{\partial y} + \frac{\partial}{\partial z}\mu\frac{\partial V}{\partial z} = 0 \tag{2-19}$$

Eq. (2-19) is called 3-D Laplace's equation.

2.1.6. Vector Potential Magnetic Field

For field which has current sources **J**, the scalar potential method cannot be applied. Because, in the scalar potential formulation, the current source **J** required to be zero (**J**=0). Therefore, another method which is called vector potential magnetic field was used [84]. From the Stokes' theorem: $\text{div}\mathbf{B} = 0$ (B is conservative) then exists vector **A** so that $\mathbf{B} = \text{rot}\mathbf{A}$. Vector **A** is called vector potential.

Using first Maxwell's equation $\text{rot}\mathbf{H} = \mathbf{J}$, and magnetic continuity relation $\mathbf{B} = \mu\mathbf{H}$, we have:

$$\text{rot}\frac{1}{\mu}\text{rot}\mathbf{A} = \mathbf{J} \tag{2-20}$$

Eq. (2-20) is Poisson's equation. It is second-order differential equation.

In the case of the field domain include conductor or current source various in times (AC), there is induced current in the field. Thus, the **J** includes two current source **J**s and induced current in conductor **J**e: $\mathbf{J} = \mathbf{J}s + \mathbf{J}e$. Therefore, Eq. (2.20) becomes:

$$\text{rot}\frac{1}{\mu}\text{rot}\mathbf{A} = \mathbf{J}s + \mathbf{J}e$$

Note that, the $\mathbf{J}e = \sigma\mathbf{E}$ with **E** is electric field intensity in the conductor.

Using third Maxwell's equation: $\text{rot}\mathbf{E} = -\partial\mathbf{B}/\partial t$, we have:

$$\text{rot}\mathbf{E} = -\frac{\partial\mathbf{B}}{\partial t} = -\frac{\partial}{\partial t}\text{rot}\mathbf{A}$$

or

$$\text{rot}\left(\frac{\mathbf{J}e}{\sigma} + \frac{\partial\mathbf{A}}{\partial t}\right) = 0$$

There is exists scalar potential V so that

$$\mathbf{J}e + \sigma\frac{\partial\mathbf{A}}{\partial t} = -\text{grad}\mathbf{V}$$

Considering that **E** is generated only by the time variation of **B**, then $\text{grad}\mathbf{V} = 0$. Finally, we have:

$$\text{rot}\frac{1}{\mu}\text{rot}\mathbf{A} + \sigma\frac{\partial\mathbf{A}}{\partial t} = \mathbf{J}s \tag{2-21}$$

In the eddy current testing, the signal sources are sinusoidal forms. Thus, the term $\partial \mathbf{A}/\partial t = j\omega \mathbf{A}$ in complex plane. Eq. (2-21) in complex term will become [84]:

$$\text{rot}\frac{1}{\mu}\text{rot}\mathbf{A} + \sigma j\omega \mathbf{A} = \mathbf{J}s \tag{2-22}$$

This is a Poisson's equation.

2.2.   Simulation in ANSYS Software

This section presents the simulation of electromagnetic field in finite element method by using ANSYS commercial software. The ANSYS software uses scalar potential magnetic field [91]-[95] and vector potential magnetic field [96]-[102] as mentioned in the previous section for simulation of static magnetic field and dynamic magnetic field, respectively. It is necessary to use several boundary conditions for accuracy solving the electromagnetic problems which were proposed in several publications [103][104]-[105]. One of the big problems in FEM is meshing method of components. A good meshing method provides accuracy simulation results, fast simulation and reduces computer resources. In this section, I present several meshing methods using in ANSYS software respect to specific application. Some simulation results also are presented in this section, which are simulations of eddy current testing (for dynamic magnetic field). The simulation for static magnetic field is not presented in here because it was presented in my Master's thesis [82]. The simulations are performed for sheet-type induced current with a rectangular crack shape, and cylinder-type magnetic camera with several hole-type cracks in a pipe.

2.2.1.   Procedure of Simulation

ANSYS software provides FEM simulation for various kinds of field such as structural analysis, multi-body analysis, thermal analysis, fluids analysis, electromagnetic field analysis, and coupled field analysis [61]. The general procedure of simulation in ANSYS software is shown in Fig. 2-8. It includes modeling, material attribution, meshing, check quality of meshing, apply power source (forces, currents, fluids etc.), choose suitable

simulation method and analysis results in post-processing. The simulation can be performed by graphic user interface (GUI) method, command method (coding) or mixing between GUI and command method. Modeling of components can be completed in ANSYS software or using others 3-D graphic design software such as Auto CAD, Solidworks, 3-D Max and Catia etc. ANSYS command method is flexible for modification of components size and simulation implementation. However, it is more difficult and time-consuming to model complicated shape of components than using 3-D graphic design software. We should define a finite space for environment such as the air to reduce simulation time. After modeling, material properties respect to simulation field is applied for each component. For example, with low frequency electromagnetic field, magnetic permeability and electrical conductivity are necessary.
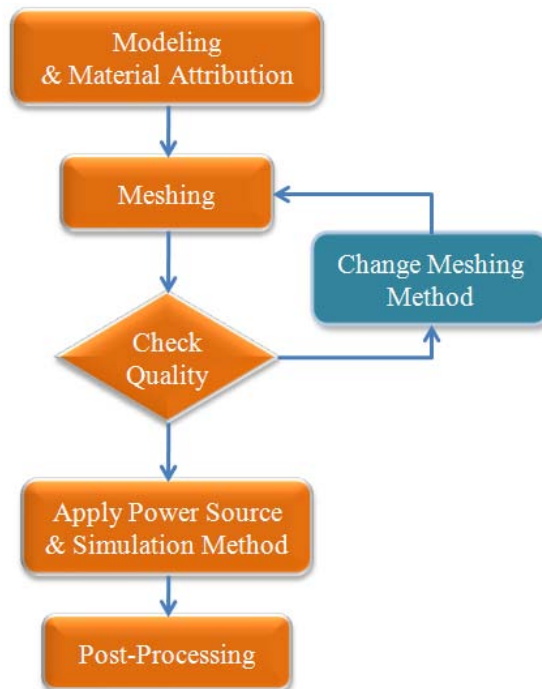
Fig. 2-8 Procedure of simulation in ANSYS Software

PLANE13
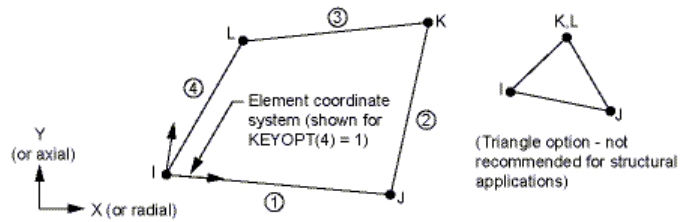
PLANE53
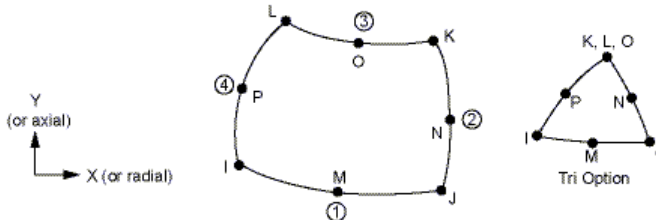
SOLID97
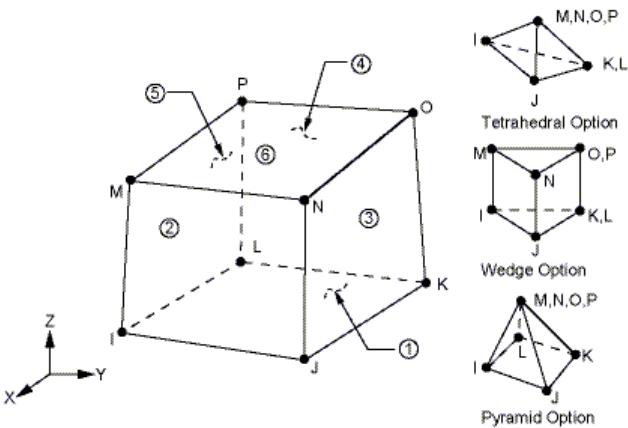
SOLID117
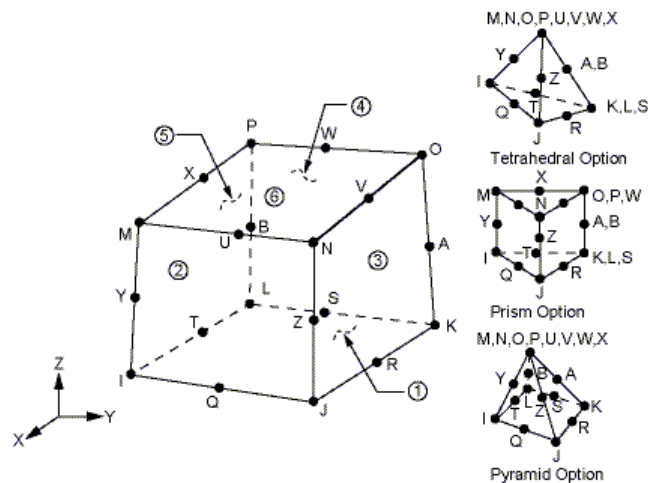
Fig. 2-9 Several element types used in ANSYS electromagnetic software.

Meshing component is one of the most important and difficult steps. A good meshing method provides accuracy simulation results, fast simulation and reduces computer resources. Several element types are implemented in ANSYS software for electromagnetic field, are PLANE13 and PLANE53 for 2-D field, SOLID97 and SOLID117 for 3-D field [106]. The illustration of each element type is shown in Fig. 2-9.

PLANE13 models 2-D magnetic field. It has 4 nodes with 4 degrees of freedom per node. The element has nonlinear magnetic capability for modeling B-H curve or permanent magnet demagnetization curves. It can be also in 2-D thermal, electrical, piezoelectric and structural field.

PLANE53 models 2-D (planar and asymmetric) magnetic field. It has 8 nodes and 4 degrees of freedom per node: z-component of magnetic vector potential, time-integrated electric scalar potential, electric current, and electromotive force. It is based on the magnetic vector potential formulation and applicable to the low-frequency magnetic field: magnetostatics, eddy current (AC time harmonic and transient analyses), voltage forced magnetic field (static, AC time harmonic and transient analyses), and electromagnetic-circuit coupled fields (static, AC time harmonic and transient analyses). The element has nonlinear magnetic capability for modeling B-H curve or permanent magnet demagnetization curves. It can be also in 2-D thermal, electrical, piezoelectric and structural field.

SOLID97 models 3-D magnetic field. It has 8 nodes and 5 degrees of freedom per node: magnetic vector potential (3 degrees), time-integrated electric potential or electric potential (1 degree), and electromotive force (1 degree). SOLID97 is based on magnetic vector potential formulation with the Coulomb gauge, and is applicable in low-frequency magnetic field: magnetostatic, eddy current (AC time harmonic and transient analyses), voltage forced magnetic field (static, AC time harmonic and transient analyses), and electromagnetic-circuit coupled fields (static, AC time harmonic and transient analyses). The element has nonlinear magnetic capability for modeling B-H curve or permanent magnet demagnetization curves.

SOLID117 models 3-D magnetic field. It has 20 nodes with 12 edge-flux degrees of freedom and one at each midside node. The eight corner nodes carry the time-integrated

electric potential or the electric potential. SOLID117 is based on the edge-flux formulation, and applies to the low-frequency magnetic field analyses: magnetostatics, eddy currents (AC time harmonic and transient analyses). The element has nonlinear magnetic capability for modeling B-H curves or permanent magnet demagnetization curves for static and transient analyses.

After having a good meshing, apply power source to the components and select simulation method. The power source could be static current density or static voltage for a coil in static field, amplitude of current density or voltage and frequency for harmonic field. The result is analyzed in post-processing stage with various types of data such as magnetic field intensity (**H**), magnetic flux density (**B**), eddy current density (**J**), magnetic force, etc.

2.2.2.   3-D Rectangular Shape of Crack on a Flat Specimen

Fig. 2-10 shows the model of sheet-type induced current (STIC) modeled in Solidworks (2009) software and ANSYS software (Ver. 11.0 SP1 UP20070830, EMAG). The model has the two cores which combined of 30 small slide cores in each. The two coils turned around these cores and were supplied by alternative current (AC). An alternative magnetic field was appeared around the two cores and induced sheet-type current on sheet type copper sheet [32], [38]. The sensing area and specimen were place under the sheet type copper sheet. Thus, the eddy current appeared in the specimen and distorted around a rectangular cross-section crack. All the components were place inside the rectangular cuboid of air (environment). The components have the properties using in ANSYS program, were shown in the Table 2-2.

Table 2-2 Properties of equipments of STIC using in ANSYS

Item	Material	Magnetic Properties	Size (mm)	Meshing size (mm)	ANSYS model type
Specimen	Aluminum	MURX1.000022 RSVX 2.82e-8	40 × 100 × 1	1	SOLID117
Core	Silicon Steel	MURX 4000 RSVX 4.72e-8	25 × 40 × 0.35 2 cores with 30 slides of each.	2	SOLID117
Coil	Copper	MURX0.999994 RSVX 1.68e-8	21 × 28 × 11 2 coils × 17 turns × 2.5A	2	SOLID117
Sheet type copper plate	Copper	MURX0.999994 RSVX 1.68e-8	28 × 126.4 × 44 thickness 0.2	1	SOLID117
Sensing area	Air	MURX 1	40 × 100 × 1	1	SOLID117
Crack	Air	MURX 1	1 × 10 × 4	2	SOLID117
Environment	Air	MURX 1	50 × 170 × 70	5	SOLID117

Modeling in Solidworks Solidworks is easy and quick tool for modeling and modify models.	
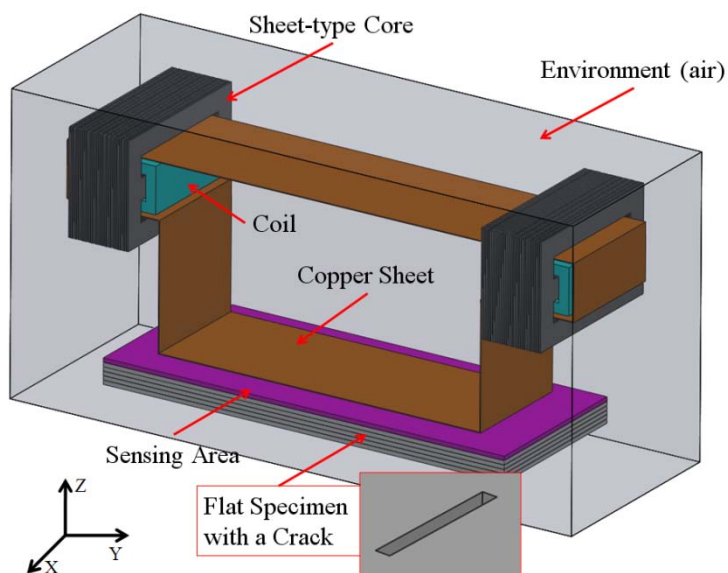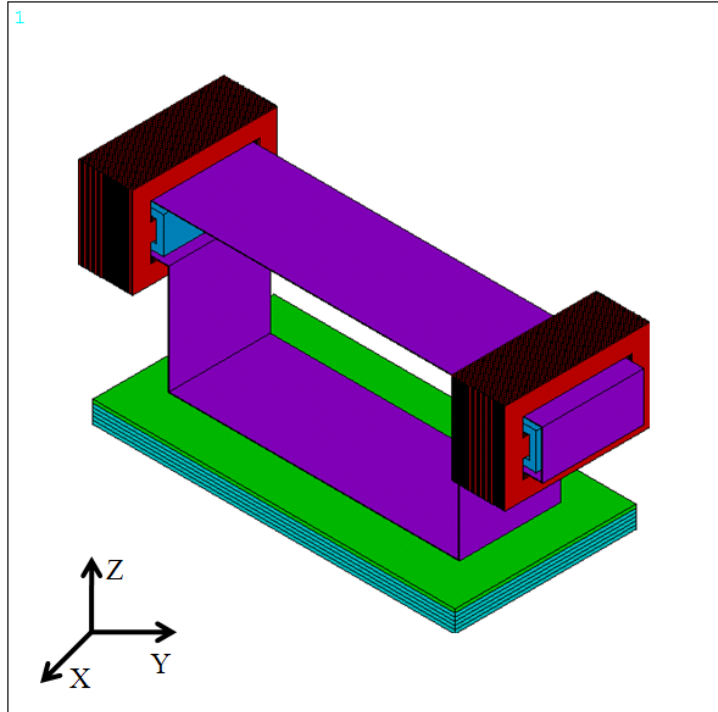
Import model to ANSYS (hide air-environment) The models are then imported to ANSYS by several formats: IGES, Catia, Catia V5, Pro/E, UG, SAT, PARA. The IGES format is the best suitable for solid components.	
Meshing in ANSYS (hide air-environment) Select each component and choose a suitable meshing method and meshing size. A good meshing result brings an accurate simulation results.	
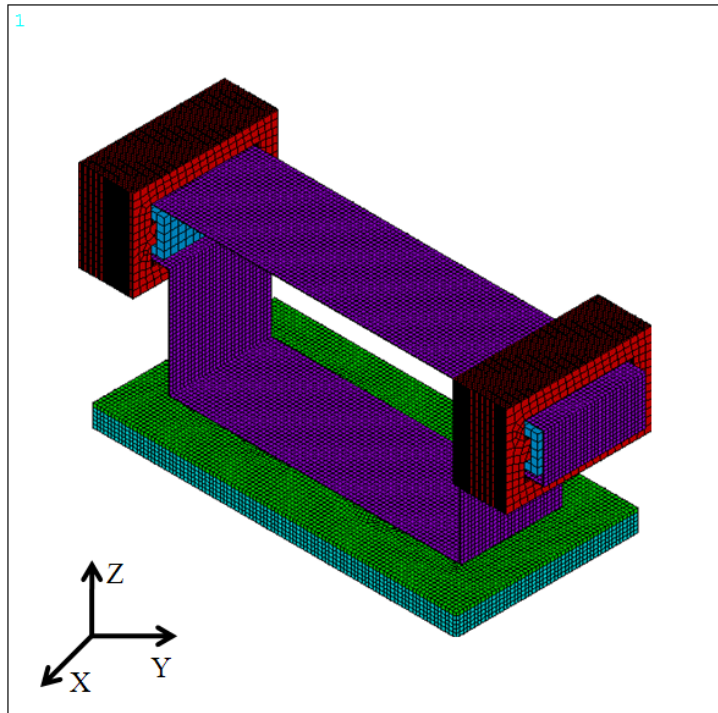
Meshing of specimen with a rectangular cross-section crack in the middle.	
Fig. 2-10 Modeling and meshing of STIC	
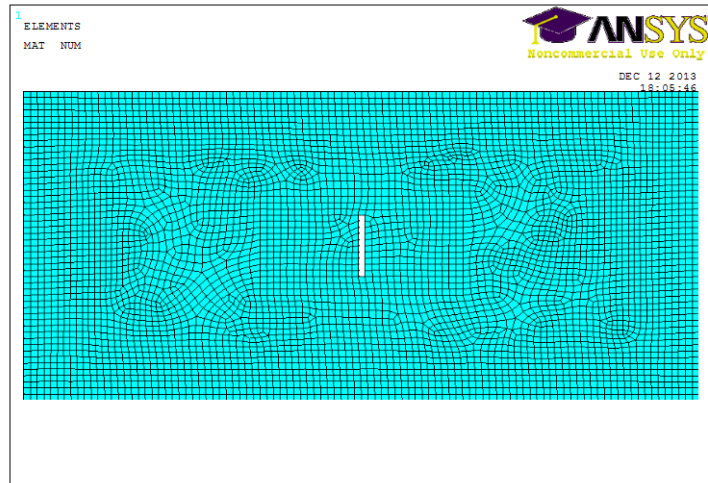
Fig. 2-11 shows the simulation results using ANSYS software. The harmonic source type was used in the simulation. The frequency of 1 kHz, 5 kHz, 10 kHz, 20 kHz, and current of 2.5 A (I) were supplied into the coils. In ANSYS software, the source is current density (J) which relates to current by: $\mathbf{J} = \mathbf{I}/S$, with S is area of surface in which current is supplied. $\mathbf{J}e$ is induced current density in specimen which is shown in top view and front view. The $\mathbf{J}e$ in high frequency (10 kHz and 20 kHz) is higher than that in 1 kHz and 5 kHz, because magnetic field concentrates at high frequency. Thus, the distorted current was high at 10 kHz and 20 kHz and low at 1 kHz and 5 kHz. We can observe the skin effect in the front view of $\mathbf{J}e$. The intensity of $\mathbf{J}e$ all frequencies decreased with the increase of penetrates depth in specimen.

The results of magnetic flux density were shown in contour plot for the three components (B_X, B_Y, B_Z) and sum of them (B): $B = \sqrt{B_X^2 + B_Y^2 + B_Z^2}$. The magnetic field was concentrated around tips of the crack making possibility of inspection of the crack using magnetic sensors. By using same color scale for all frequencies, we cannot observe the crack in B_X component and sum magnetic field B at 1 kHz. However, when we change the color scale, we can see the crack image, as shown in the two last images. We observe

that with the increase of frequencies, the magnetic density increased and more concentrated around the crack. At low frequencies (1 kHz and 5 kHz), the magnetic field from edges of specimen affects to the magnetic field of the crack, thus it makes difficult to inspect the crack. However, the two magnetic fields were clearly separated at high frequency (10 kHz and 20 kHz), thus the crack images which are magnetic field of crack were clear. Comparing magnetic density of each component, we observe that B_Y component is the smallest and B_X component is the highest. However, the cracks image in B_Y component are the most clear and cracks image in B_X component is the worst clear. Thus, I recommend that we should use high sensitive magnetic sensor such as GMR and AMR sensors to measure B_Y component, then, the inspection probability will be high. And, for measure B_X and B_Z components, we can use lower sensitive magnetic sensor but higher range of measurement such as Hall sensor. In practical, only two components of magnetic field are measured, which are B_Y and B_Z components, because crack image in B_X component is not clear.

	1 kHz	5 kHz	10 kHz	20 kHz	
Je Top View					←15E+4 [A/mm²] ←5E+4
Je Front View					←15E+4 [A/mm²] ←5E+4
B_Y					← 3E-5 [T] ←2.5E-5

B_Z				
B_X				
B				

B_X (1 kHz) - Auto Scale

We can see crack by changing color scale

B (1 kHz) - Auto Scale

We can see crack by changing color scale

$$B = \sqrt{B_X^2 + B_Y^2 + B_Z^2}$$

Fig. 2-11 Simulation results for a rectangular crack with 1, 5, 10, and 20 kHz using ANSYS software
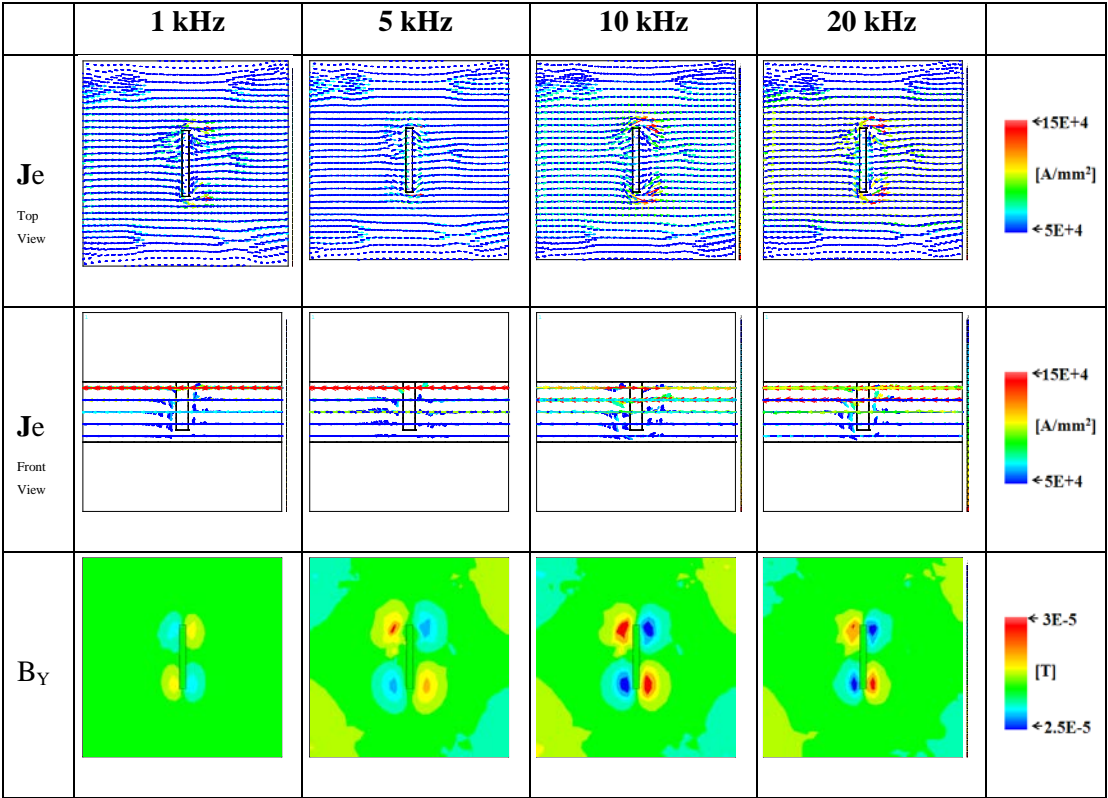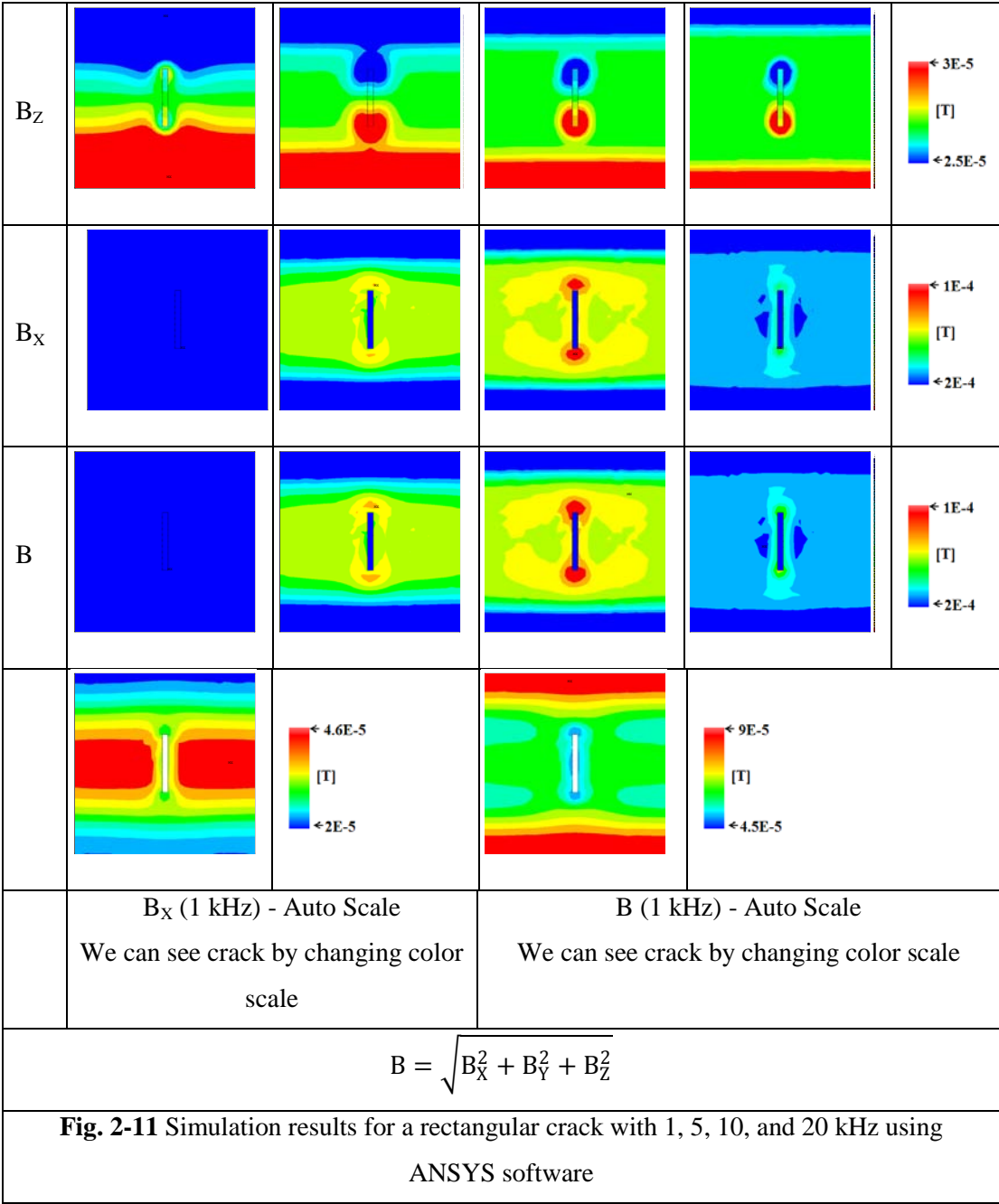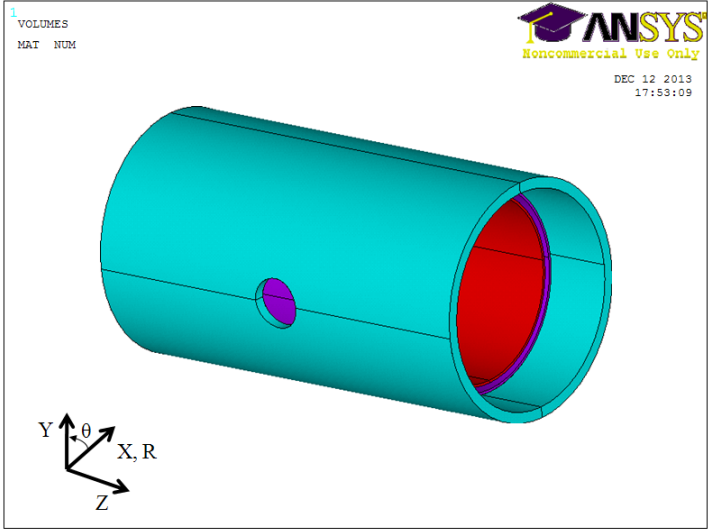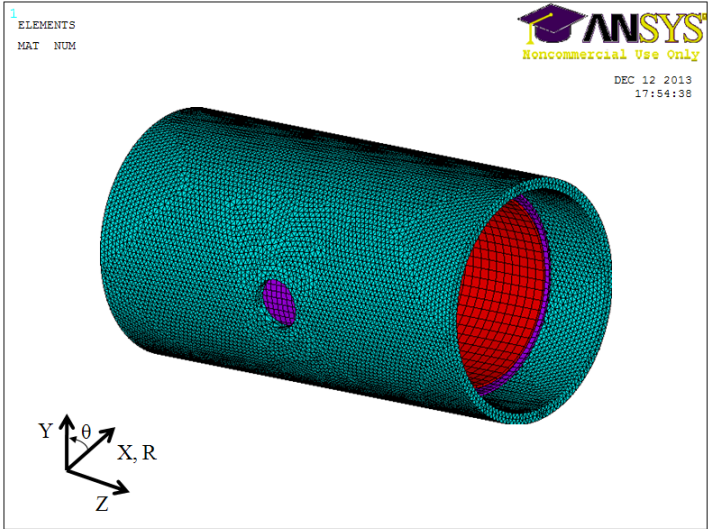
2.2.3. Cracks on Pipe Specimen

Fig. 2-12 shows a model of a crack inspection in a pipe [122]. This is a simulation for corrosions in small piping system (i.e. heat exchanger). The model was built in Solidworks (2009) software and ANSYS ver. 11.0 SP1 UP20070830 EMAG. The model was firstly built in Solidworks for easy modeling and then import to ANSYS software by IGES format. The terms R, θ and Z are the radial, circumferential, and axial directions, respectively, in the cylindrical coordinate system. A Cartesian coordinate system XYZ has Z- and X- axis same with Z- and R- axis of cylindrical coordinate system, respectively. Table 2-3 provides components sizes, magnetic properties of materials, meshing size for each component and modeling type in ANSYS software.

Modeling in Solidworks Solidworks is easy and quick tool for modeling and modify models.	

Import model to ANSYS (hide air-environment) The models are then imported to ANSYS by several formats: IGES, Catia, Catia V5, Pro/E, UG, SAT, PARA. The IGES format is the best suitable for solid components.	
Meshing in ANSYS (hide air-environment) Select each component and choose a suitable meshing method and meshing size. A good meshing result brings an accurate simulation results.	
Fig. 2-12 Modeling and meshing of Cylinder-type magnetic camera	

Table 2-3 Properties of components used in the ANSYS software

Components	Material	Relative Permeability	Electrical Resistivity	Size [mm]	Meshing [mm]	Model type
Pipeline specimen	Titanium	1.00005	5.2E–7 [m/S]	ϕ_{Out} 19 × 35 ϕ_{In} 17.28 × 35	0.43	SOLID 117
Outer Diameter Cracks	Air	1	-	Detail in Table 2-4	0.43	SOLID 117
Sensing area(Cylinder sensor)	Air	1	-	ϕ15 × 24.96 × 0.2	0.78	SOLID 117
Environment	Air	1	-	40 × 50 × 40	5	SOLID 117
Bobbin coil	Air	1	-	ϕ16.4 × 24.96 × 0.2	0.5	SOLID 117

Fig. 2-13 shows the meshing of three types of crack which usually appear in heat exchanger piping system [122]. The size, material, and simulation parameters are listed in Table 2-1. The titanium pipe has an outer diameter of 19 mm, inner diameter of 17.28 mm and length of 35 mm. The bobbin coil was modeled with 140 turns, an outer diameter of 16.4 mm, thickness of 0.2 mm, and length the same as the length of the Cylinder sensor which is 24.96 mm. I performed the simulation at low frequency that an alternating current with amplitude of 0.6 at 5 kHz supplied to the bobbin coil. Several hole-type through and outer-diameter (OD) cracks and circumferential cracks were modeled. The detail sizes are shown in Table 2-4.

| Circumferential Crack | These types of crack are simulation of far-side corrosions which usually appear in heat exchanger piping system. |

Fig. 2-13 Meshing of several types crack
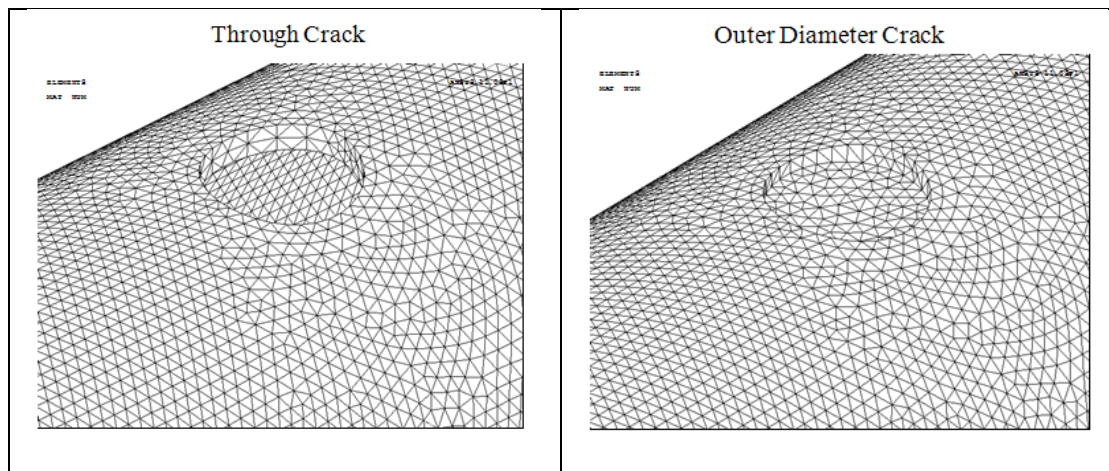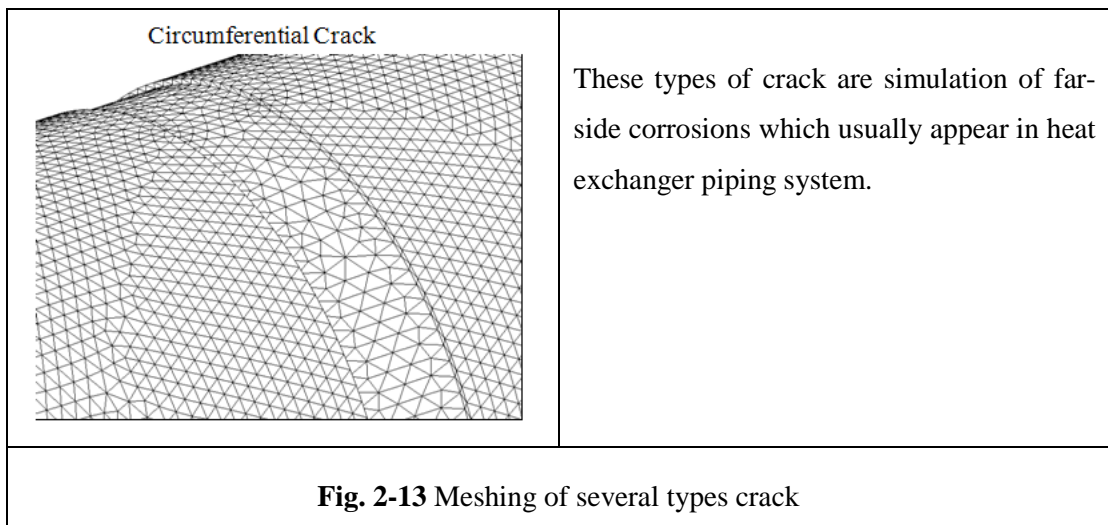
Table 2-4 Size and shape of cracks on titanium pipe

No.	Shape	Depth [mm]	Depth [%]	Diameter [mm]	Volume [mm^3]
1	OD	0.315	37%	1.5	0.543
2	Through	0.860	100%	1.5	1.521
3	OD	0.499	58%	1.8	1.242
4	OD	0.697	81%	1.8	1.746
5	OD	0.315	37%	2.7	1.666
6	OD	0.499	58%	2.7	2.719
7	OD	0.697	81%	2.7	3.852
8	Through	0.860	100%	2.7	4.936
9	OD	0.315	37%	4.6	4.067
10	OD	0.499	58%	4.6	8.285
11	OD	0.697	81%	4.6	10.415
12	Through	0.860	100%	4.6	14.409

ANSYS software can display various types of data such as eddy current and magnetic flux density, magnetic field intensity, and magnetic force etc. The eddy current in specimen **J**e was displayed in vector field as shown in Fig. 2-14. The crack is hole-type through crack with 4 mm of diameter. The eddy current has smallest value in the two tips of the pipe because they are near the two tips of the bobbin coil. In the middle of the pipe, the eddy current was uniform, where are also the middle of the bobbin coil. The presence of a hole-type through crack obstructed the eddy current flow. Thus, the eddy current

turned around the crack. It concentrated on the left- and right- hand sides of the crack respect to the eddy current flow direction.

Fig. 2-15 shows the magnetic flux density in the three components (BX, BY and BZ), radial component (B_R) and the sum of magnetic field (B). The magnetic field concentrates on the left- and right-hand sides of the crack respect to the eddy current flow, in which the eddy current is concentrated. In the B_X component, we can observe most clearly distribution of magnetic field around the crack than other components (B_Y, B_Z). Thus, the possibility of crack detection is highest. The B_Y component, which is tangential direction of the pipe, has a little lower value than the B_X component. Thus, the possibility of crack detection is lower than using B_X component. However, the distributions of B_X and B_Y are not uniform respect to the axial of the pipe due to the pipe shape. The B_Z component, which is axial direction of the pipe, has highest value because it includes additional highly magnetic field from the bobbin coil. However, this component of magnetic field has a uniform distribution to the axial direction of the pipe. This component can be used in NDT if we use magnetic sensor with a high range of measurement of magnetic field. The axial component of magnetic field (B_R), which is combination of B_X and B_Y components as described in Eq. (2-23), has uniform distribution to the axial direction of the pipe and clearly observation the distribution around the crack. Thus, the B_R component has highly potential in detection of the crack.

$$B_R = \sqrt{B_X^2 + B_Y^2}$$ (2-23)

- 42 -

Je	
Je (Zoom in of crack)	
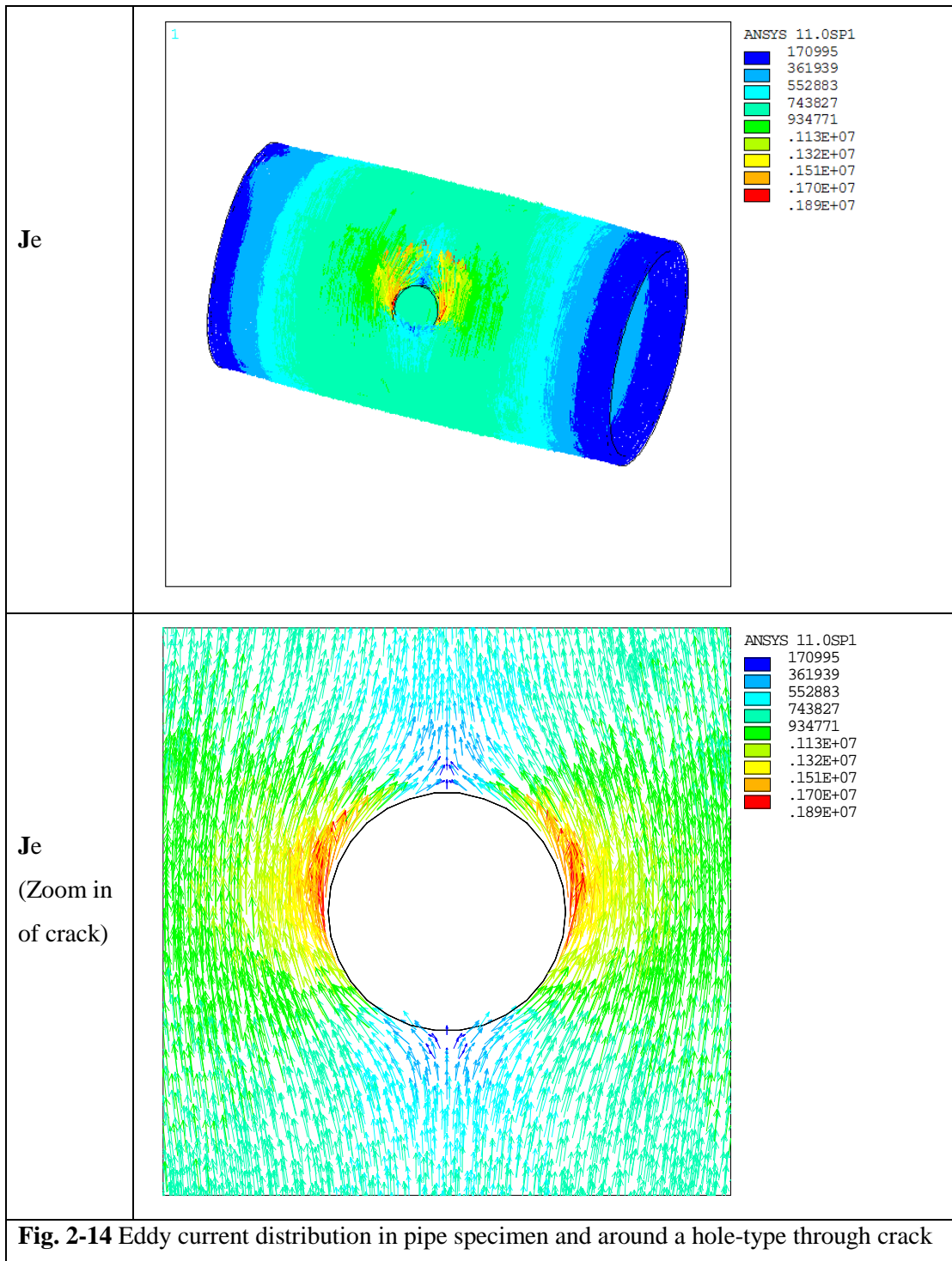
Fig. 2-14 Eddy current distribution in pipe specimen and around a hole-type through crack

B$_X$ In Cartesian coordinate system	
B$_Y$ In Cartesian coordinate system	

B$_Z$ In Cartesian coordinate system	
B$_r$ In Cylindrical coordinate system	

B	

$$B_R = \sqrt{B_X^2 + B_Y^2}$$

$$B = \sqrt{B_X^2 + B_Y^2 + B_Z^2}$$

Fig. 2-15 Distribution of eddy current vector and magnetic flux density in titanium pipe for 4 mm diameter hole-type through crack simulated by ANSYS software.
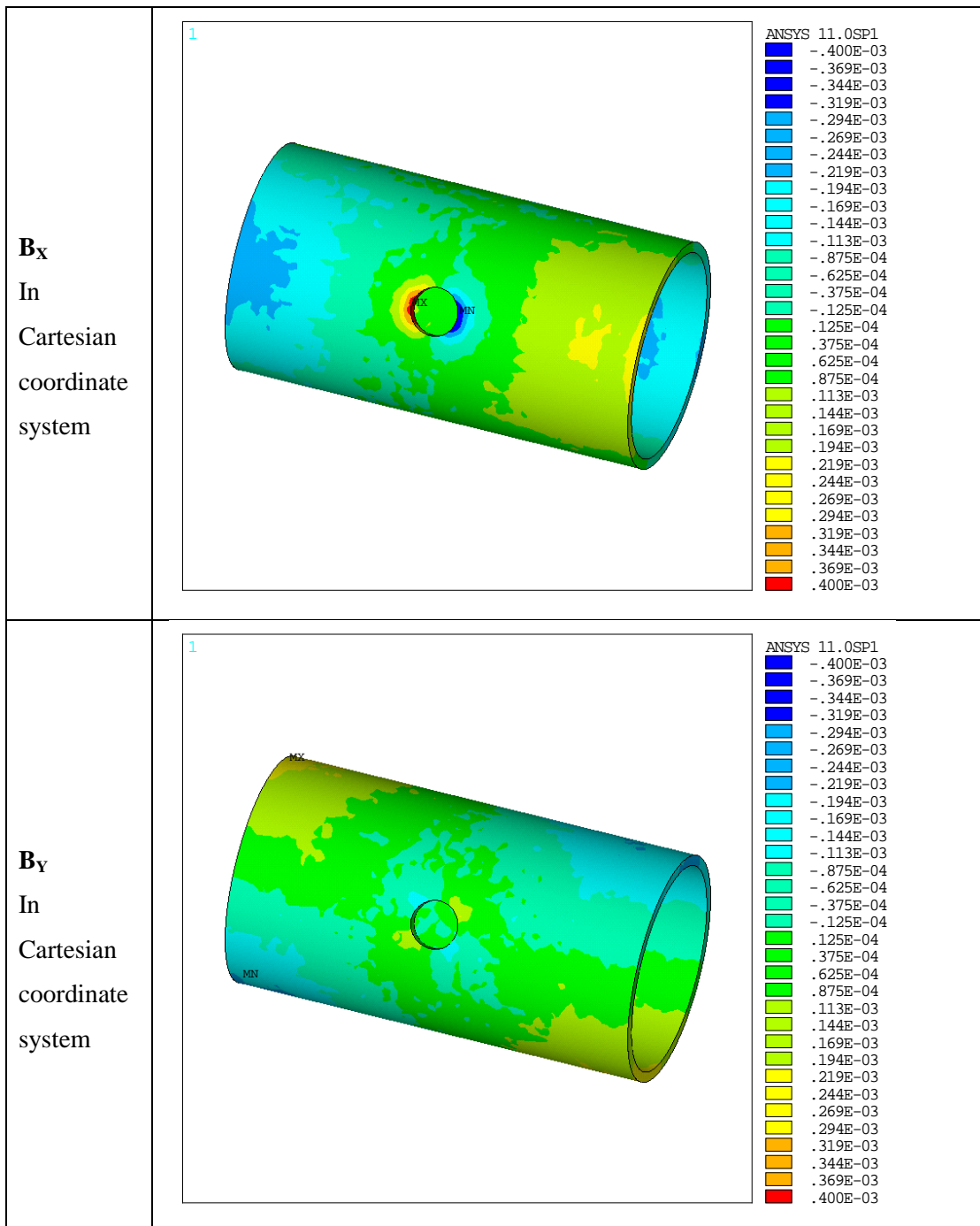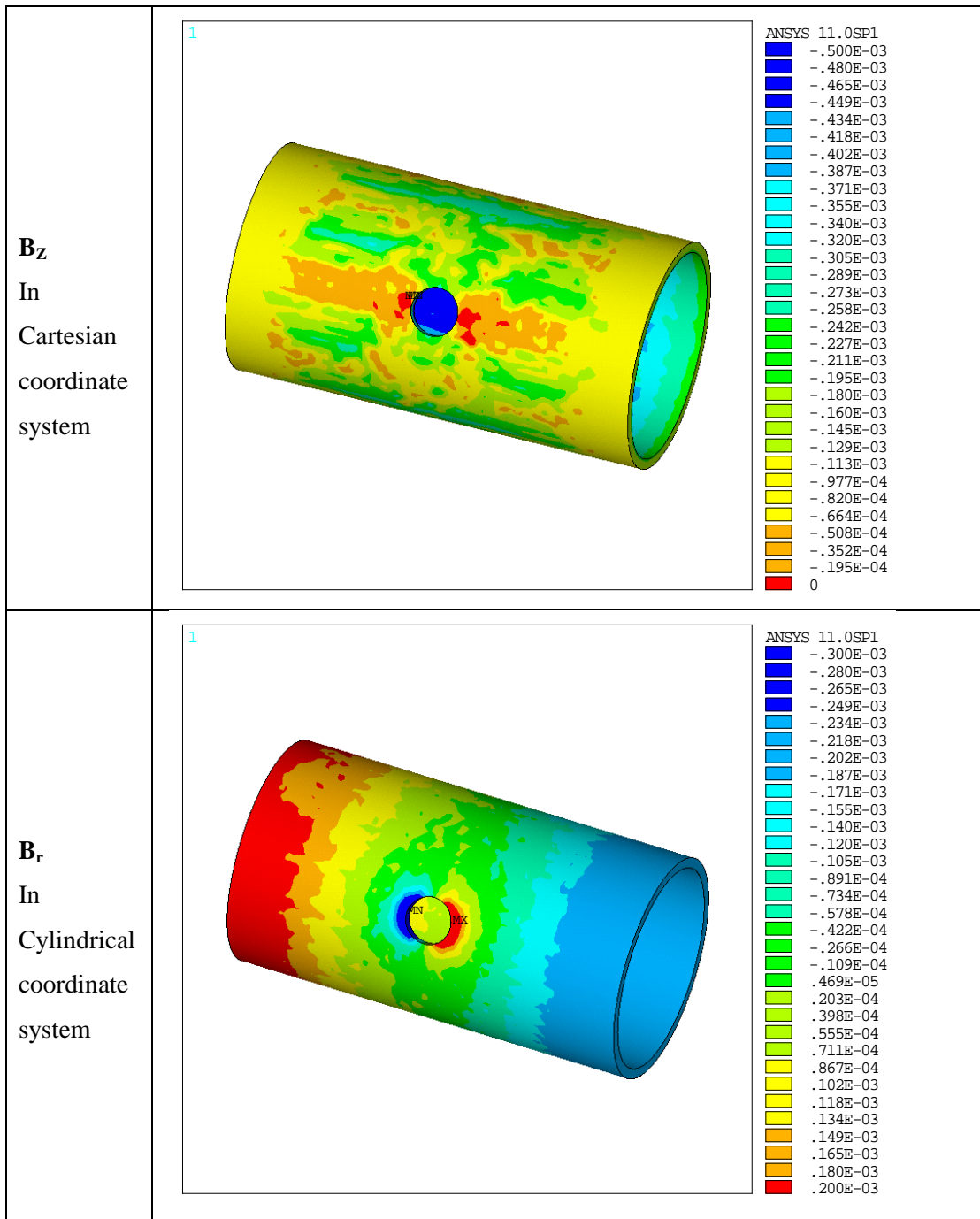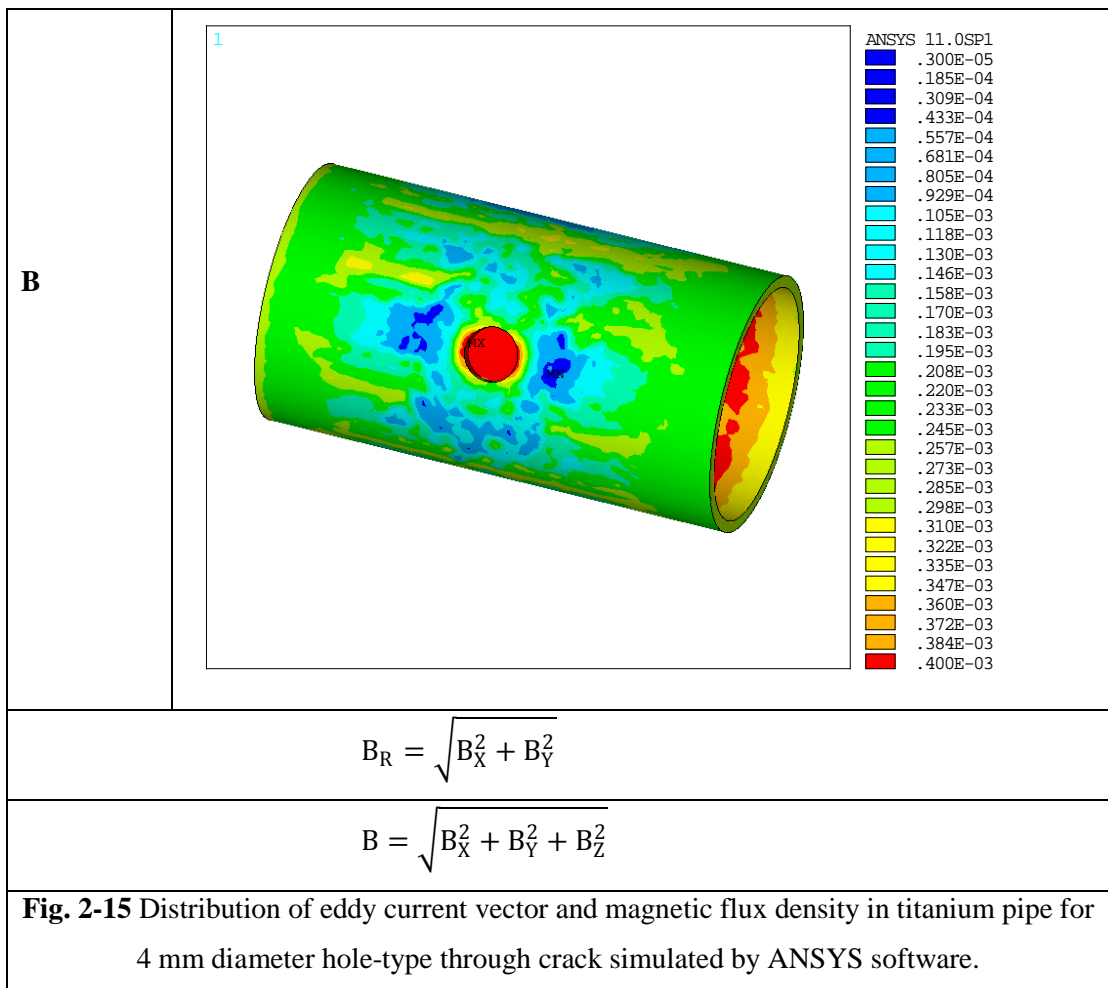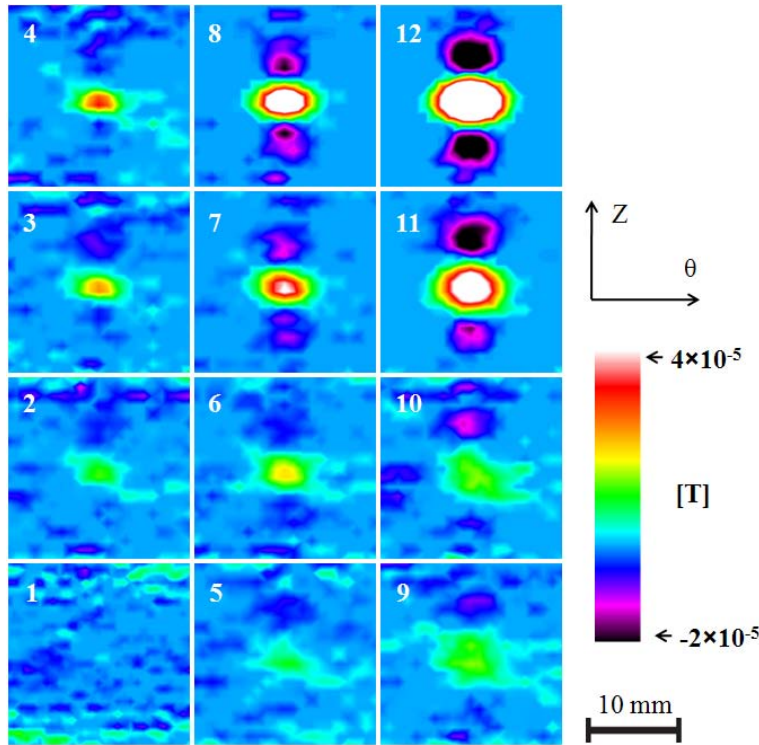
Fig. 2-16 Crack images in B_R-component magnetic flux density simulated by using ANSYS software

Fig. 2-16 shows the simulation results for cracks in Table 2-4 with B_R-component magnetic flux density [122]. The B_R was calculated from B_X- and B_Y-components in Cartesian coordinate system, as expressed in Eq. (2-23). The cracks in each column have the same depth but different diameters, and the cracks in each row have the similar diameter but different depths. The image of a crack is the distribution of the differential magnetic field (ΔB_R, Eq. (2-24)) around that crack, which has 2 fairly symmetric groups and an oval-shape in the center. The distribution area of ΔB_R increases with an increase in crack diameter, as seen by glancing over the figure from left to right. When glancing over the figure from bottom to top, the value of ΔB_R is seen to increase with an increase in crack depth. However, the images of the results were not clear. This is due to the accumulated errors in the FEM simulation, and meshing size of components.

$$\Delta B_R(Z, \theta) = B_R(Z, \theta + \Delta\theta) - B_R(Z, \theta) \qquad (2\text{-}24)$$

- 47 -

2.3. Previous Dipole Model Method

This section summarizes some results of the previous dipole model method. The dipole model was only applied for magnetic flux leakage testing (MFLT), DC and AC magneto-optical testing. Several crack shapes such as rectangular, triangular, elliptical, stepped cross-section view were modeling and simulated with applied of horizontal and vertical of DC magnetic fields [82], [83]. The dipole model method has advantages than finite element method, which are simple simulation equation, no need meshing of components, easy implement and fast simulation. However, the previous DM is still limited at the alternating magnetic field, which was done for only a rectangular crack in the magneto-optical testing [46], [82]. Thus, the development of DM for alternating magnetic field and more types of crack shape is necessary, which is the target of the thesis. The further development of the dipole model will be presented in the next chapter.

2.3.1. Static Magnetic Field

2.3.2.1. Horizontal Magnetization
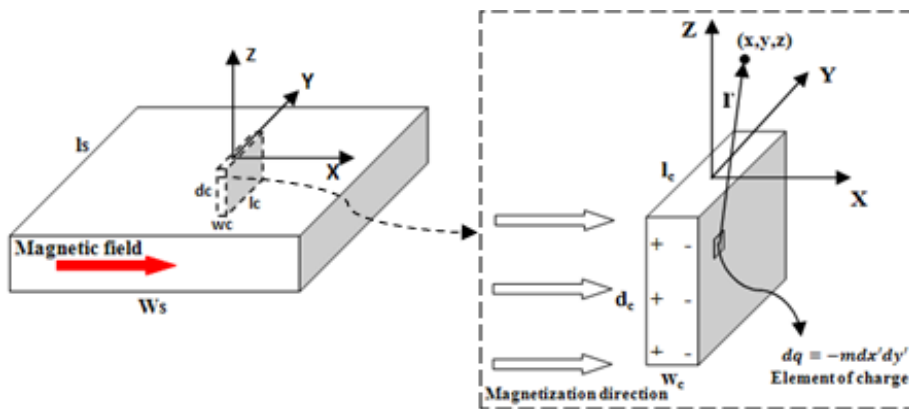
Fig. 2-17 Dipole model of a crack in the case of horizontal magnetization

Fig. 2-17 shows the dipole model and Cartesian coordinate system for the case of horizontal magnetization. The XY plane is represented on the surface of the specimen, the Y-direction is parallel with the length direction of the crack, the magnetization direction is in the X-direction, and the Z-direction is presented as the vertical direction to the surface of

specimen. DMA assumes that magnetic charges exist on both walls of a crack. The magnetic charge of area $dx'dy'$ on the back wall is $dq = -mdx'dy'$. This magnetic charge induces a magnetic flux density at point $\mathbf{r}$(x, y, z), d$\mathbf{B}$, is calculated by Eq. (2-25) [82], [83].

$$d\vec{\boldsymbol{B}} = \frac{dq}{4\pi r^3}\vec{\boldsymbol{r}} \tag{2-25}$$

The total magnetic flux density at point $\mathbf{r}$ (x, y, z) which is induced by magnetic charges on the two walls of crack can be described [82], [83]:

$$\vec{\boldsymbol{B}} = \frac{1}{4\pi}\int_{\frac{-l_c}{2}}^{\frac{l_c}{2}}\int_{-d_c}^{0}\frac{m\vec{\boldsymbol{r_1}}}{|\vec{\boldsymbol{r_1}}|^3}dz'dy' - \frac{1}{4\pi\mu}\int_{\frac{-l_c}{2}}^{\frac{l_c}{2}}\int_{-d_c}^{0}\frac{m\vec{\boldsymbol{r_2}}}{|\vec{\boldsymbol{r_2}}|^3}dz'dy' \tag{2-26}$$

with $\vec{\boldsymbol{r_1}} = \left(x + \frac{w_c}{2}, y - y', z - z'\right)$, $\vec{\boldsymbol{r_2}} = \left(x - \frac{w_c}{2}, y - y', z - z'\right)$

$$|\vec{\boldsymbol{r_1}}|^3 = \left[\left(x + \frac{w_c}{2}\right)^2 + (y - y')^2 + (z - z')^2\right]^{3/2}$$

$$|\vec{\boldsymbol{r_2}}|^3 = \left[\left(x - \frac{w_c}{2}\right)^2 + (y - y')^2 + (z - z')^2\right]^{3/2}$$

where, m, l_c, w_c, d_c and z are the magnetic charge per unit area, and the length, width, depth of the crack and the lift-off, respectively. Magnetic charge is a function of shape, size, and strength of magnetization.

The three components of the MFL can be calculated by the Eqs. (2.27)-(2.29) [82], [83]:

$$B_X = \frac{1}{4\pi}\int_{\frac{-l_c}{2}}^{\frac{l_c}{2}}\int_{-d_c}^{0}m\left(\frac{|\vec{\boldsymbol{r_{1x}}}|}{|\vec{\boldsymbol{r_1}}|^3} - \frac{|\vec{\boldsymbol{r_{2x}}}|}{|\vec{\boldsymbol{r_2}}|^3}\right)dz'dy' \tag{2-27}$$

$$B_Y = \frac{1}{4\pi}\int_{\frac{-l_c}{2}}^{\frac{l_c}{2}}\int_{-d_c}^{0}m|\vec{\boldsymbol{r_{1y}}}|\left(\frac{1}{|\vec{\boldsymbol{r_1}}|^3} - \frac{1}{|\vec{\boldsymbol{r_2}}|^3}\right)dz'dy' \tag{2-28}$$

$$B_Z = \frac{1}{4\pi}\int_{\frac{-l_c}{2}}^{\frac{l_c}{2}}\int_{-d_c}^{0}m|\vec{\boldsymbol{r_{1z}}}|\left(\frac{1}{|\vec{\boldsymbol{r_1}}|^3} - \frac{1}{|\vec{\boldsymbol{r_2}}|^3}\right)dz'dy' \tag{2-29}$$

Furthermore, when the crack is moved (x_{offset}, y_{offset}) and rotated by θ_c from its center on the XY plane, the relocated crack position in the new plane $X_R Y_R$, as shown in Fig. 2-18 can be expressed as the equation (2-30). Thus, the **B** is changed to $\boldsymbol{B}cos\theta_c$ [82], [83].
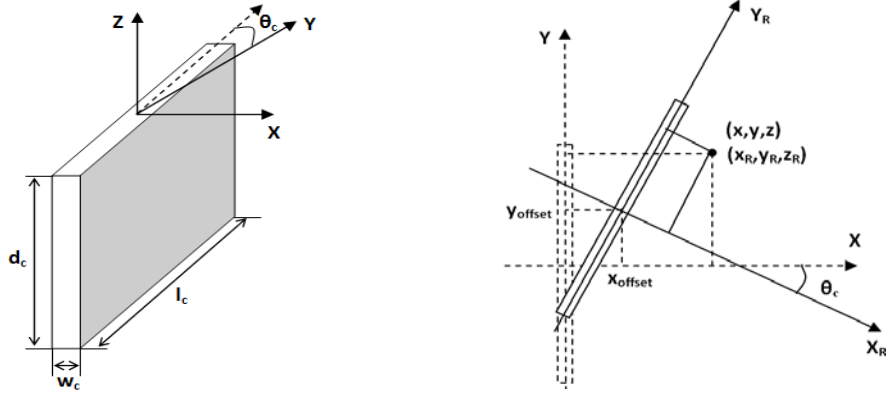
Fig. 2-18 Relocating position of crack

$$x_R = (x - x_{offset})cos\theta_c - (y - y_{offset})\,sin\theta_c$$
$$y_R = (x - x_{offset})sin\theta_c + (y - y_{offset})\,cos\theta_c \tag{2-30}$$

To simulate the multiple cracks (n cracks), we can use the principle of superposition of magnetic field. In which, the total magnetic field ($\boldsymbol{B}_{total}$) at one point is the sum of partial magnetic fields ($\boldsymbol{B}_i$) as the equation (2-31).

$$\boldsymbol{B}_{total}(x, y, z) = \sum_{i=1}^{n} \boldsymbol{B}_i(x, y, z) \tag{2-31}$$

With another crack type, we assume it is sum of small rectangular cracks as shown in Fig. 2-19. Thus, the magnetic field can be expressed by equation (2-31). In here, I give some simple crack type such as triangle crack, elliptical crack and step crack. These cracks are divided into small rectangular cracks. By this method, the accuracy is depending on the number of divided rectangular crack.

(a) Triangle crack   (b) Elliptical crack   (c) Step crack
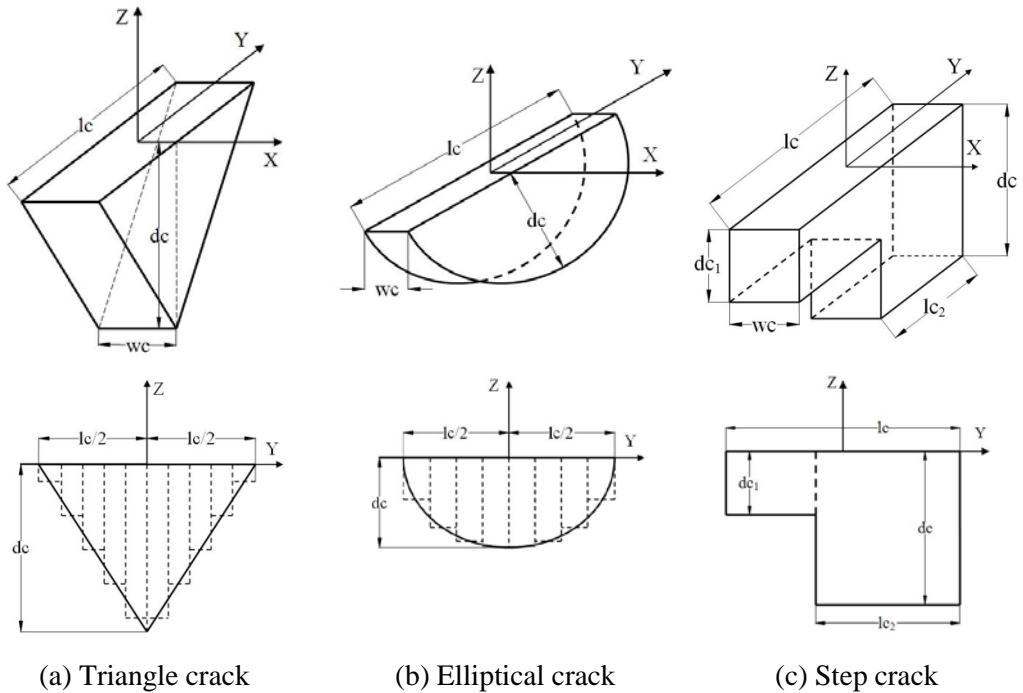
Fig. 2-19 Different crack shapes and their division method

The 3-D models of crack were modeled in a Dipole Model Software [82], [83], as shown in Fig. 2-20. Each crack has 1 mm of width, 10 mm of length, and 1 mm of depth. The step of the stepped crack has depth of 0.5 mm and length of 5 mm. The lift-offs were 1 mm, and the magnetization direction perpendicular with the length of cracks ($\theta_c = 0$).

The simulation results are shown in Fig. 2-21. Each crack was simulated separately. The magnetic charge was assumed to be uniform; the value is 1 Wb/m^2. The time of simulation for every crack was under 1s. We can observe the different MFLs of different crack shapes. The MFL of rectangular crack has a flat top and bottom. The MFL of triangular and elliptical cracks have a sharp at top and bottom, but the MFL of elliptical crack are less sharp than that of the triangular crack. The MFL of stepped crack has stepped shape at top and bottom. We can observe these more clearly by using 2-D top and side view in Fig. 2-22. We can clearly distinguish the rectangular and stepped cracks but difficult for triangular and elliptical cracks. The triangular and elliptical cracks have similar profile of MFL correspond to the similar shape of the cracks.
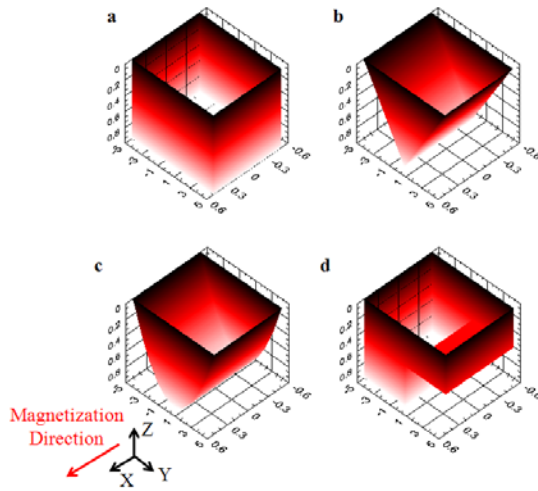
Fig. 2-20 Modeling of rectangular (a), triangular (b), elliptical (c), and stepped (d) cross-section of crack in Dipole Model Software. Unit [mm]
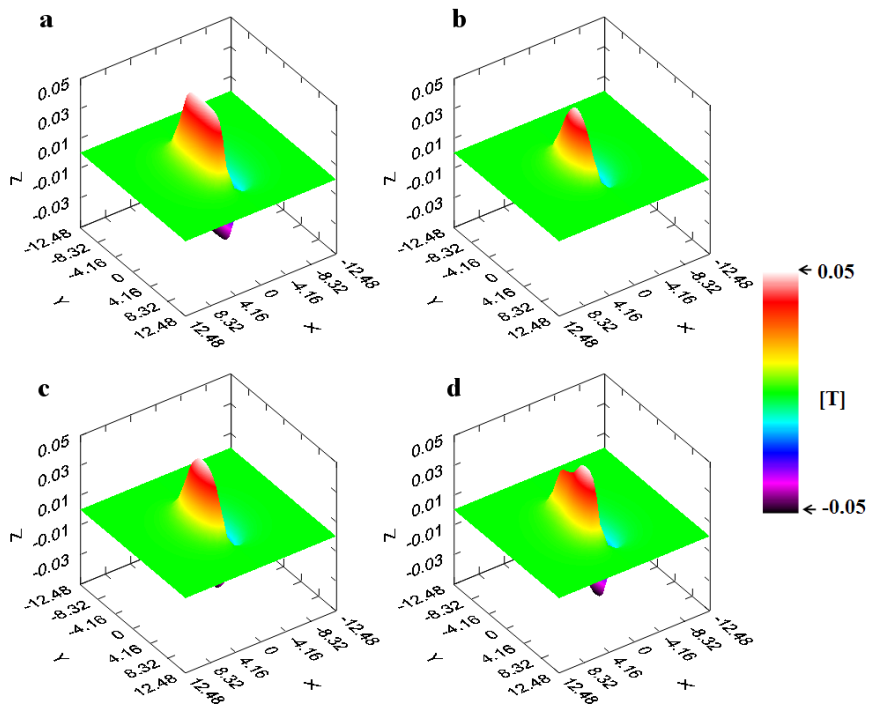
Fig. 2-21 3-D view simulation results of rectangular (a), triangular (b), elliptical (c), and stepped (d) cross-section of crack in the case of horizontal magnetization.
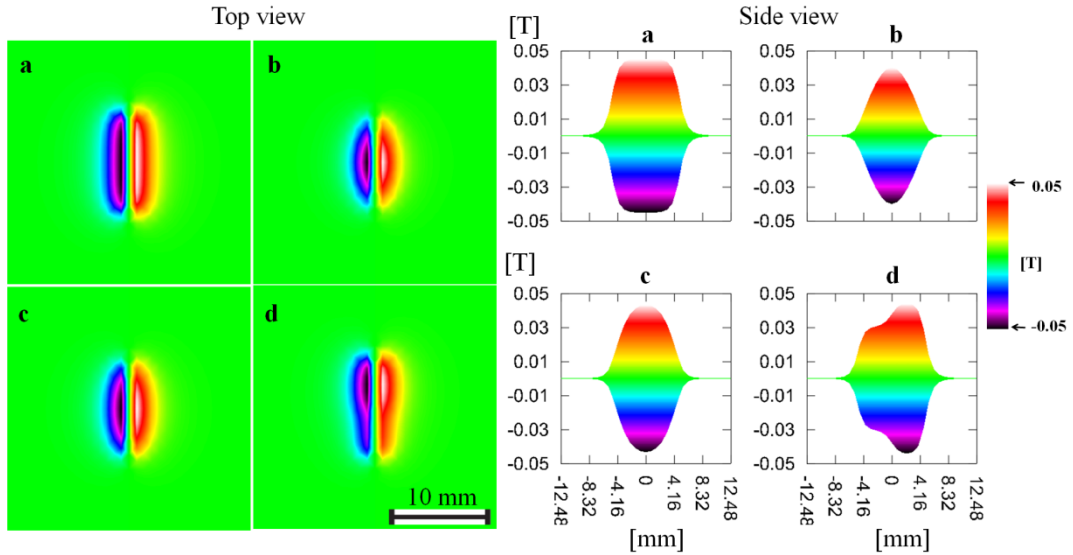
Fig. 2-22 2-D views simulation results of rectangular (a), triangular (b), elliptical (c), and stepped (d) cross-section of crack in the case of horizontal magnetization.

2.3.2.2. Vertical Magnetization

In some applications, vertical magnetic field is used for magnetizing the inspecting objects and the vertical component of magnetic field is usually measured. For example, in inspection of cracks on the wheels of a train [123], the vertical permanent magnets were arrayed in the rail for magnetizing the wheel. The changes of magnetic field due to presence of cracks were measured by using a number of Area Integrated Hall Sensors Array (AIHaS). In application of magneto-optical imager (MOI), the vertical magnetic field was also used [1], [80]. The width and length of a crack could be inspected regardless of the length direction of the crack.

The dipole model of crack in the case of vertical magnetization is shown in Fig. 2-23 [82], [83]. The magnetic charge (m) is assumed to be uniform occurs on the surface of specimen and at the bottom of crack. We can consider that m is distributed on the whole surface of specimen by width w_S and length l_S (the magnetic flux density would be $B_{Z,all}$). And at the bottom of crack by width w_c and length l_c at the distance in the Z-direction (the magnetic flux intensity would be $B_{Z,crack}$). At the bottom of this crack, m is distributed

- 53 -

with width w_c, length l_c and at the d_c distance in the Z-direction (the magnetic flux intensity would be $B_{Z,under}$). Fig. 2-24 shows the model for calculation of the magnetic field of an area magnetic charge. Similar with the method used in the case of horizontal magnetic field, for an area (w × l) magnetic charge, the magnetic flux density at point $\mathbf{r}$(x, y, z) by Z-direction can be expressed by equation (2-32) [78], [79]. The distribution of magnetic field of the overall can be calculated by the equation (2-33). If the crack is rotated or relocated position, the new position of the crack is calculated by equation (2-31). And, the distribution of magnetic field is not affected by the direction of the crack (the length direction of the crack) because the magnetization direction is always perpendicular to the length of the crack.
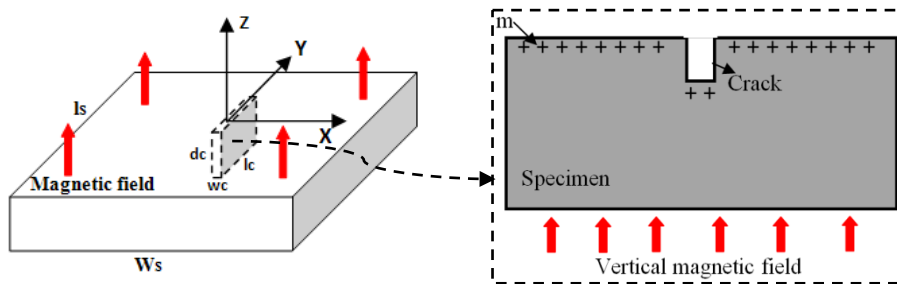
Fig. 2-23 Dipole model of crack in the case of vertical magnetization
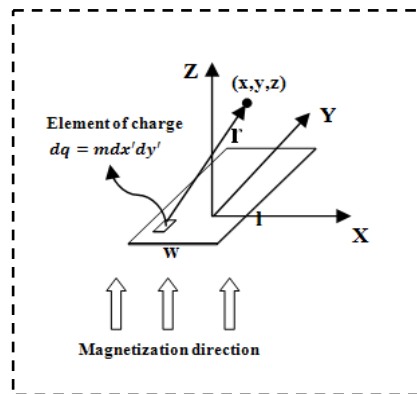
Fig. 2-24 Calculation of magnetic field by an area magnetic charge

$$B_z = \frac{1}{4\pi} \int_{\frac{-l_c}{2}}^{\frac{l_c}{2}} \int_{-d_c}^{0} m \frac{|\overrightarrow{r_z}|}{|\vec{r}|^3} dz' dy' \qquad (2\text{-}32)$$

with $\vec{r} = (x - x', y - y', z)$

$|\vec{r}|^3 = [(x - x')^2 + (y - y')^2 + z^2]^{3/2}$

$$B_{Z,total} = B_{Z,all} - B_{Z,crack} + B_{Z,under} \qquad (2\text{-}33)$$

Fig. 2-25 and Fig. 2-26 show the simulation results for cracks, which are used in the case of horizontal magnetization. The distribution of magnetic field (DMF) of cracks has only one region value that is lower than that in the non-crack area. The DMF shape has similar to the shape of crack. The DMF of the rectangular crack has a flat bottom and look like a trapezium shape. The DMF the triangular and elliptical crack has one peak and its shape likes a half of an ellipse. However, the shape of DMF of the triangular crack is sharper than that of the elliptical crack. The DMF of the stepped crack has a step as the stepped crack. Thus, we can distinguish the crack shape due to the shape of DMF.

In practical applications, we must use a width range of measurement of magnetic sensors for measuring the vertical component of magnetic field in the case of vertical magnetization. But, in the case of horizontal magnetization, we can use much smaller range of measurement. Because the measuring magnetic field in the vertical magnetization is about 4 times higher than in the case of horizontal magnetization, which is shown in the simulation results. However, the changes of the magnetic field due to crack in the both cases of magnetization is similar, which is about 0.1 mT. Thus, the sensitivity of magnetic sensors can be similar for the both cases. Therefore, the horizontal magnetization method is frequently used than the vertical magnetization method.
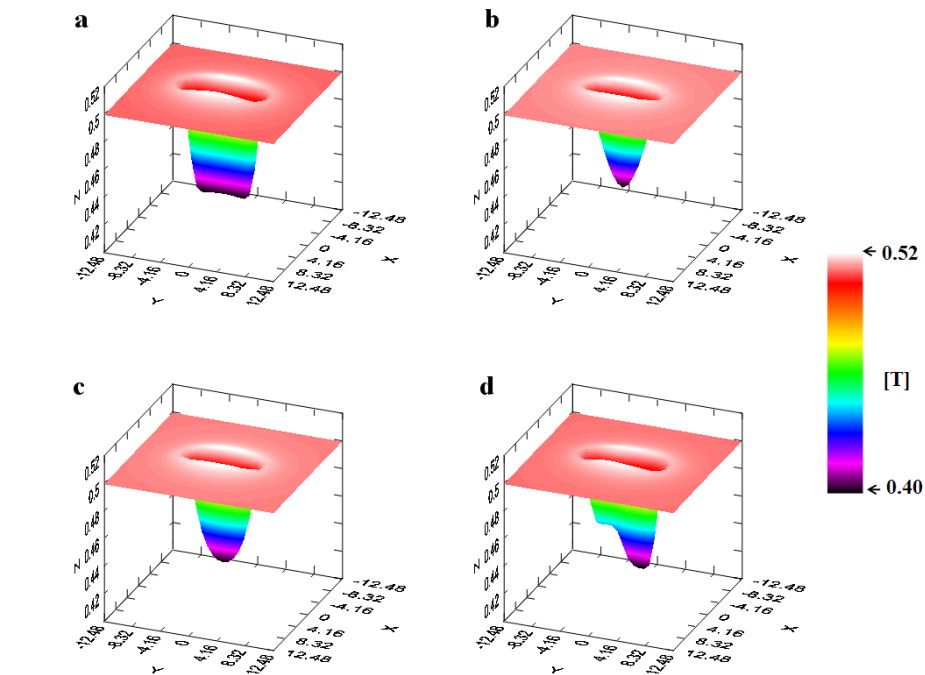
Fig. 2-25 3-D view simulation results of rectangular (a), triangular (b), elliptical (c), and stepped (d) cross-section of crack in the case of vertical magnetization.
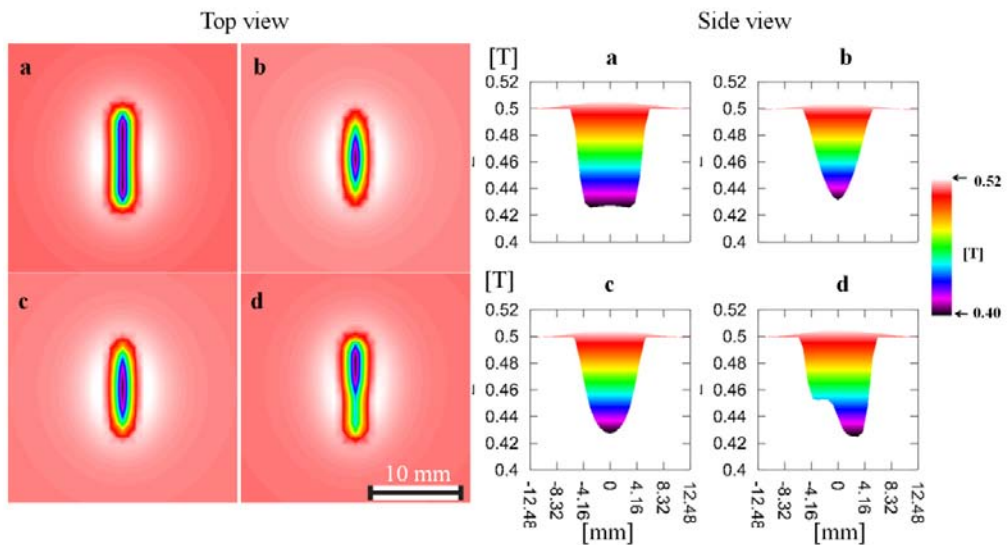
Fig. 2-26 2-D view simulation results of rectangular (a), triangular (b), elliptical (c), and stepped (d) cross-section of crack in the case of vertical magnetization.

2.3.2. Alternating Magnetic Field

In the simulation of magnetic distribution for static magnetic field, the crack was assumed to be filled by dipoles with dipole moments oriented opposite to the direction of the applied magnetic field, as shown in Fig. 2-27(a). In contrast, the dipoles was assumed to be appeared in the walls and tips of the crack corresponding to the distribution of eddy current around the crack, as shown in Fig. 2-27(b).

(a) Static magnetic field   (b) Alternative magnetic field
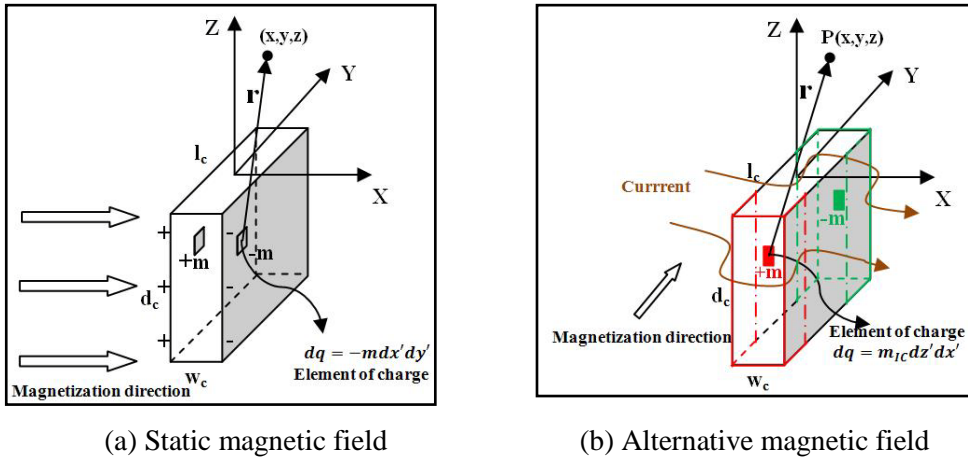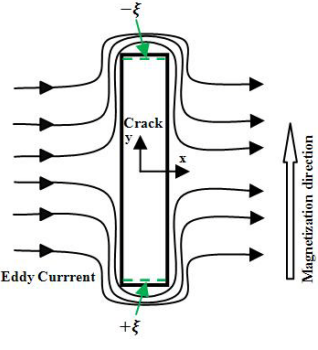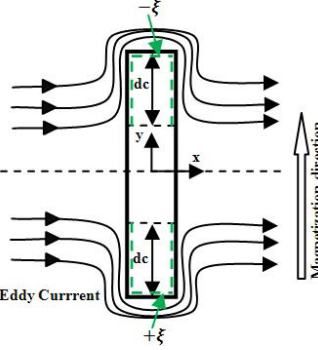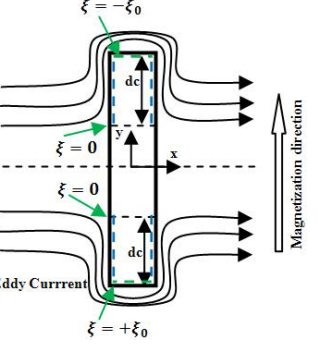
Fig. 2-27 Dipole model

In the static magnetic field, magnetic charge depends on shape, size of crack and strength of the applied magnetic field, as shown in Eq. (2-34). However, the magnetic charge also depends on the skin effect in the alternating magnetic field. When an alternating magnetic field is applied to a conductive specimen, an eddy current is produced in the specimen, which has strength exponentially decrease with increase of depth from the surface of specimen. The skin effect was discussed detail in the previous section. Thus, the magnetic charge was assumed having same behavior as the eddy current, that is, the magnetic charge also exponentially decrease with the increase of the depth from the surface of specimen, as described in Eq. (2-35) [46], [82]. The ξ was called magnetic charge factor, which is a function of shape and size of crack, and strength of eddy current.

$$m_{st} = m_{static}\,(shape, w_c, l_c, d_c) \tag{2-34}$$

$$m_{al} = \xi e^{-\frac{t}{\delta}} \tag{2-35}$$

$$\xi = \xi(\,shape, w_c, l_c, d_c) \tag{2-36}$$

First assumption	Second assumption	Third assumption
$\xi(tips) = \pm\xi_0$	$\xi(tips) = \pm\xi_0$ $\xi(walls) = \pm\xi_0$	$\xi(tips) = \pm\xi_0$ $\xi(y-) = +\xi_0 \dfrac{-y - l_c/2 + d_c}{d}$ $\xi(y+) = -\xi_0 \dfrac{y - l_c/2 + d_c}{d}$

Fig. 2-28 Three assumptions of distribution of magnetic charges on a rectangular crack

In the previous study, a rectangular cross-section crack was modeled with three assumptions, as shown in Fig. 2-28 [46]. The first assumption, magnetic charge uniformly appears on tips of crack. The second assumption, magnetic charge uniformly appears on walls and tips of crack, in which the length of the magnetic charge area on the walls are equal to the crack depth (d_c). The third assumption, the areas of magnetic charge is same with in the second assumption, however, the magnetic charges only uniform in the tips but linearly distribute in the walls.

The magnetic field intensity was calculated for each case shown in Eqs. (2-37)-(2-39) [46], [82].

with $\quad \overrightarrow{r_1} = (x - x^{'}, y + lc/2, z - z^{'}), \overrightarrow{r_2} = (x - x^{'}, y - lc/2, z - z^{'})$

$\quad\quad\quad \overrightarrow{r_3} = (x + wc/2, y - y', z - z^{'}), \overrightarrow{r_4} = (x - wc/2, y - y', z - z^{'})$

First assumption:

$$H_z = \frac{\xi}{4\pi\mu} \int_{-w_c/2}^{w_c/2} \int_{-d_c}^{0} m|\overrightarrow{r_{1z}}| \left(\frac{1}{|\overrightarrow{r_1}|^3} - \frac{1}{|\overrightarrow{r_2}|^3} \right) dz^{'} dx^{'} \tag{2-37}$$

Second assumption:

$$H_z = \left[\frac{\xi}{4\pi\mu} \int_{-w_c/2}^{w_c/2} \int_{-d_c}^{0} m|\overrightarrow{r_{1z}}| \left(\frac{1}{|\overrightarrow{r_1}|^3} - \frac{1}{|\overrightarrow{r_2}|^3} \right) dz' dx' \right. \tag{2-38}$$

$$+ \frac{\xi}{4\pi\mu} \int_{\frac{-l_c}{2}}^{\frac{-l_c}{2}+d_c} \int_{-d_c}^{0} m|\overrightarrow{r_{3z}}| \left(\frac{1}{|\overrightarrow{r_3}|^3} + \frac{1}{|\overrightarrow{r_4}|^3} \right) dz' dy'$$

$$- \frac{\xi}{4\pi\mu} \int_{\frac{l_c}{2}-d_c}^{\frac{l_c}{2}} \int_{-d_c}^{0} m|\overrightarrow{r_{3z}}| \left(\frac{1}{|\overrightarrow{r_3}|^3} + \frac{1}{|\overrightarrow{r_4}|^3} \right) dz' dy'$$

Third assumption: magnetic flux density is calculated by substitute magnetic charge factor in the third assumption into that in the second assumption to Eq. (2-38) [46], [82].

The simulation results were compared with experiment results of the MOI [46], [82]. A rectangular cross-section crack with size of $0.7 \times 10 \times 3$ mm in an aluminum alloy (Al7075) plate was used. The magnetic charge factor, frequency, permeability and electrical conductivity of aluminum alloy, saturated magnetic field of magneto-optical film (MOF), bias magnetic field, and temperature in experiment environment are shown in Table 2-5. The experiment and simulation results are shown in Fig. 2-29. The third assumption shows the best agreement with the experiment result.

Table 2-5 Simulation parameters

Lift-Off (z)	1 [mm]	
Maximum magnetic charge factor (ξ_0)	First assumption	10^{-4} [Wb/m^2]
	Second assumption	2×10^{-5} [Wb/m^2]
	Third assumption	2×10^{-5} [Wb/m^2]
Frequency	25.6 kHz	
Permeability of Specimen (μ)	1.2566×10^{-6} [H/m]	
Electrical conductivity (σ)	3.5461×10^{7} [S/m]	
Saturated magnetic field of MOF (H_s)	0.3 [mA/m]	
Bias magnetic field (H_b)	0.05 [mA/m]	
Temperature (T)	24 [^{0}C]	

- 59 -
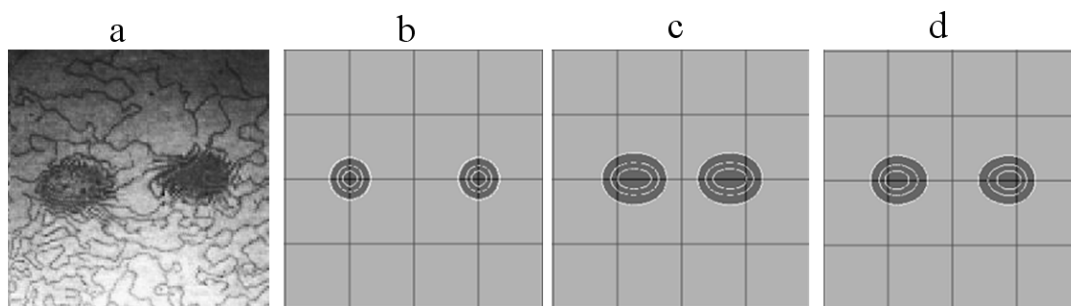
Fig. 2-29 Comparison between experiment (a) with simulation: firs assumption (b), second assumption (c), and third assumption (d).

The dipole model for alternating magnetic field was successful simulates the MOI results. However, there are still some limitations. The simulated crack was simple; it was just a rectangular cross-section shape. The maximum magnetic charge factor was uncertainty. And, the comparison was just in the shape of crack image, but not in quantitative because the limitation of quantitative of MOI; MOI has only one bit data: 1-black color, 0- white color. Therefore, it is necessary to improve the dipole model to overcome these limitations. The improvement will be discussed in the section 4.

CHAPTER 3 IMPROVED DIPOLE MODEL METHOD

When an eddy current flow approaches a crack, it will circulate around the tips and the bottom of the crack [46]. In the DM, the magnetic charge dipoles are assumed to occur along the path of the eddy current flows, which means that they occur on the surface and walls of the crack. Thus, the distribution of magnetic charges differs according to the shape of the crack and the direction of the eddy current. Positive and negative magnetic charges occur on the right- and left-hand side of the eddy current, respectively. In addition, the magnetic charges on the walls of the crack are complicated, given that they depend on the shape of the crack. However, the distribution of magnetic charges on the surface of the crack can be expressed by an equation. We suggest that the profile of the crack is a function $z' = F(y')$, as shown in Fig. 3-1. Thus, the RMS magnetic charge at point (y', z') on the profile surface of the crack can be described by Eq. (2-1) [46].
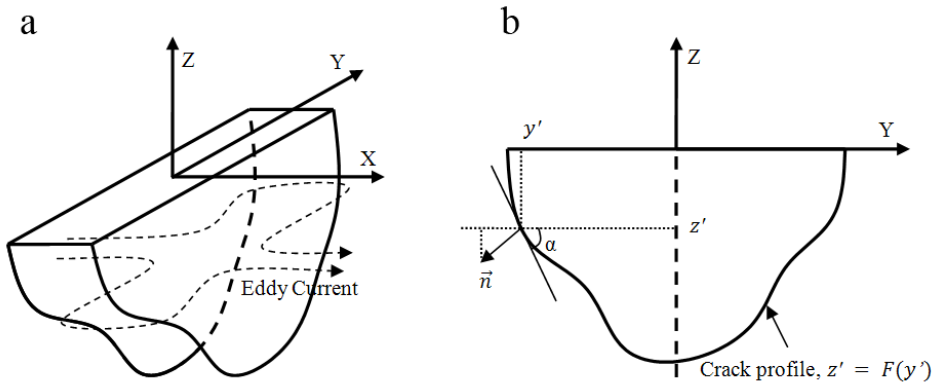
Fig. 3-1 Complex-shaped crack. (a) 3D view, (b) section view

$$m_{RMS} = \xi \cdot e^{\frac{z'}{\delta}} \cdot sin\alpha . cos\beta \qquad (z' < 0) \qquad \text{(3-1)}$$

$$sin\alpha = \frac{tan\alpha}{\sqrt{1 + tan^2\alpha}}$$

$$tan\alpha = -F'(y')$$

$$cos\beta = \angle(eddy\ current, X\ axis)$$

$$\delta = \frac{1}{\sqrt{\pi f \mu \sigma}}$$

here, δ, f, μ, σ are the skin depth, frequency of the alternating magnetic field, absolute permeability, and electrical conductivity of the specimen, respectively, where α is the angle between the tangential line at point (y', z') of the profile and the y-axis, β is the angle between the eddy current and x-axis, and F' is the differential of function F at point y', which is known as the angular coefficient of the tangential line. And, ξ is a magnetic charge factor that is positive or negative according to the position of point (y', z') on the right- or left-hand side of the eddy current flow, respectively.

3.1. Dipole Model of Cracks on a Flat Specimen

Several theoretical analyses have also been conducted for simulate cracks on flat specimen over the years such as finite element method (FEM) [81], [129]-[131], analytical modeling of PEC based on time-harmonic problems [99], [132], and extended truncated region eigenfunction expansion (ETREE) [133]. These methods produce results that are in have good agreement with the experimental results. However, these methods employ complex equations that lead to long simulation times.

The DM method was proposed to simulate an alternating magnetic field based on MOI [46]. This method uses simple equations that enable rapid calculations. In this section, we extend the DM for AC-type magnetic camera, which can model the 3-D distribution of an alternating magnetic field around a crack, and then characterize the crack. This section improves the DM method for simulation of several simple crack shapes: rectangular, triangular, elliptical and stepped on flat specimen.

3.1.1. Dipole Model of a Rectangular crack
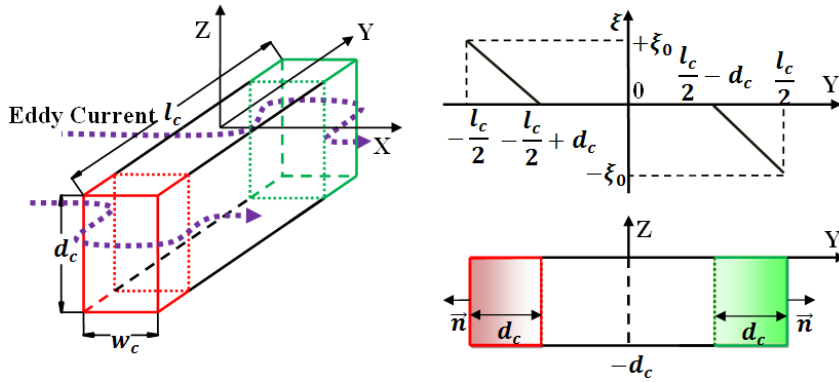
Fig. 3-2 Dipole model of rectangular cross-section crack

Fig. 3-2 shows the dipole model of the rectangular cross-section crack ($w_c \times l_c \times d_c$), the coordinate system and the distribution of the magnetic charge factor. The magnetic charge factor is uniform on the two crack tips, and varies linearly along the two crack walls at distance d_c from the tips [46]. The RMS magnetic charge at point (y', z') on these surfaces can be calculated by Eq. (3-2), where $\xi_R(y')$, $\xi_L(y')$ and $\xi(\pm l_c/2)$ are the magnetic charge factors on the right- and left-hand side of the wall and at the tips of the crack, respectively [46].

$$m_{RMS} = \xi(y') \cdot e^{\frac{z'}{\delta}} \tag{3-2}$$

$$\xi_R(y') = +\xi_0 \cdot \frac{-y' - l_c/2 + d_c}{d_c}$$

$$\xi_L(y') = -\xi_0 \cdot \frac{y' - l_c/2 + d_c}{d_c}$$

$$\xi(\pm l_c/2) = \mp\xi_0$$

The RMS magnetic field at point (x, y, z) (out-of-specimen) in the Z-direction is the sum of magnetic field induced from the two tips and walls of the crack, as expressed in the Eq. (3-3). Finally, the RMS magnetic field is expressed in Eq. (3-4) [46].

$$B_{RMS} = B_{Right\ Tip} + B_{Left\ Tip} + B_{Right\ Walls} + B_{Left\ Walls} \tag{3-3}$$

$$B_{Right\ Tip} = \frac{+\xi_0}{4\pi} \int_{-w_c/2}^{w_c/2} \int_{-d_c}^{0} \frac{e^{\frac{z'}{\delta}}(z-z')}{\{(x-x')^2 + (y+lc/2)^2 + (z-z')^2\}^{3/2}}$$

$$B_{Left\ Tip} = -\frac{\xi_0}{4\pi} \int_{-w_c/2}^{w_c/2} \int_{-d_c}^{0} \frac{e^{\frac{z'}{\delta}}(z-z')}{\{(x-x')^2 + (y-lc/2)^2 + (z-z')^2\}^{3/2}} dz'\,dx'$$

$B_{Right\ Walls}$

$$= \frac{\xi_0}{4\pi} \int_{\frac{-l_c}{2}}^{\frac{-l_c}{2}+d_c} \int_{-d_c}^{0} \frac{e^{\frac{z'}{\delta}}(z-z')}{\{(x+wc/2)^2 + (y-y')^2 + (z-z')^2\}^{3/2}} \frac{-y-l_c/2+d_c}{d_c} dz'\,dy'$$

$$+ \frac{\xi_0}{4\pi} \int_{\frac{-l_c}{2}}^{\frac{-l_c}{2}+d_c} \int_{-d_c}^{0} \frac{e^{\frac{z'}{\delta}}(z-z')}{\{(x-wc/2)^2 + (y-y')^2 + (z-z')^2\}^{3/2}} \frac{-y-l_c/2+d_c}{d_c} dz'\,dy'$$

$B_{Left\ Walls}$

$$= -\frac{\xi_0}{4\pi} \int_{\frac{l_c}{2}-d_c}^{\frac{l_c}{2}} \int_{-d_c}^{0} \frac{e^{\frac{z'}{\delta}}(z-z')}{\{(x+wc/2)^2 + (y-y')^2 + (z-z')^2\}^{3/2}} \frac{y-l_c/2+d_c}{d_c} dz'\,dy'$$

$$-\frac{\xi_0}{4\pi} \int_{\frac{l_c}{2}-d_c}^{\frac{l_c}{2}} \int_{-d_c}^{0} \frac{e^{\frac{z'}{\delta}}(z-z')}{\{(x-wc/2)^2 + (y-y')^2 + (z-z')^2\}^{3/2}} \frac{y-l_c/2+d_c}{d_c} dz'\,dy' \Bigg]$$

$$B_{RMS} = \xi_0 \sum_{i=0}^{1} \frac{(-1)^i}{4\pi} \int_{-w_c/2}^{w_c/2} \int_{-d_c}^{0} \frac{e^{\frac{z'}{\delta}}(z-z')}{\{(x-x')^2 + (y+(-1)^i l_c/2)^2 + (z-z')^2\}^{3/2}} dz'\,dx' \qquad (3\text{-}4)$$

$$+ \xi_0 \sum_{j=0}^{1} \sum_{i=0}^{1} \frac{1}{4\pi d_c} \int_{(-1)^j \frac{l_c}{2}}^{(-1)^j \left(\frac{l_c}{2}-d_c\right)} \int_{-d_c}^{0} \frac{e^{\frac{z'}{\delta}}(z-z')((-1)^j y' - l_c/2 + d_c)}{\{(x+(-1)^i w_c/2)^2 + (y-y')^2 + (z-z')^2\}^{3/2}} dz'\,dy'$$

3.1.2. Simulated Results of a Rectangular Crack

The simulation was performed for a rectangular cross-section crack, as modeling in Fig. 3-3. The crack has size of $1 \times 10 \times 3$ mm and was simulated in an aluminum alloy (Al7075) plate. The magnetic charge factor, frequency, permeability and electrical conductivity of aluminum alloy are shown in Table 3-1. The maximum magnetic charge factor was simply assumed to be 1 Wb/m^2. The frequency was 5 kHz corresponds to the skin depth of 1.2 mm.

Table 3-1 Simulation parameters

Lift-Off (z)	1 [mm]
Maximum magnetic charge factor (ξ_0)	1 [Wb/m^2]
Frequency	5 kHz
Permeability of Specimen (μ)	1.2566×10^{-6} [H/m]
Electrical conductivity (σ)	3.5461×10^{7} [S/m]
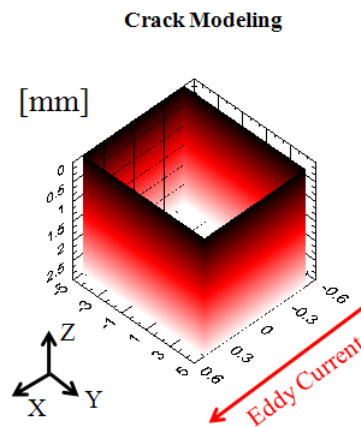
Fig. 3-3 Modeling of rectangular cross-section crack in dipole model software

Fig. 3-4 shows the simulation results of the RMS of vertical (Z-component) magnetic flux density (B_{RMS}) and its differential in the Y-direction (ΔB_{RMS}, Eq. (3-5)). In the B_{RMS} image, it has two peaks at the two tips of the crack, which is result of concentration of eddy current flux at the tips of crack. In the ΔB_{RMS} image, it has four peaks with two negative peaks in the middle of two positive peaks. In the both image of

- 65 -

B_{RMS} and ΔB_{RMS}, the images are symmetric to the two planes at the center of crack in the both X-axis and Y-axis, because the crack shape is symmetric in these planes.

$$\Delta B_{RMS} = B_{RMS}(i,j) - B_{RMS}(i,j-1) \qquad (3\text{-}5)$$

where i and j are index of data point in X- and Y-direction, respectively.
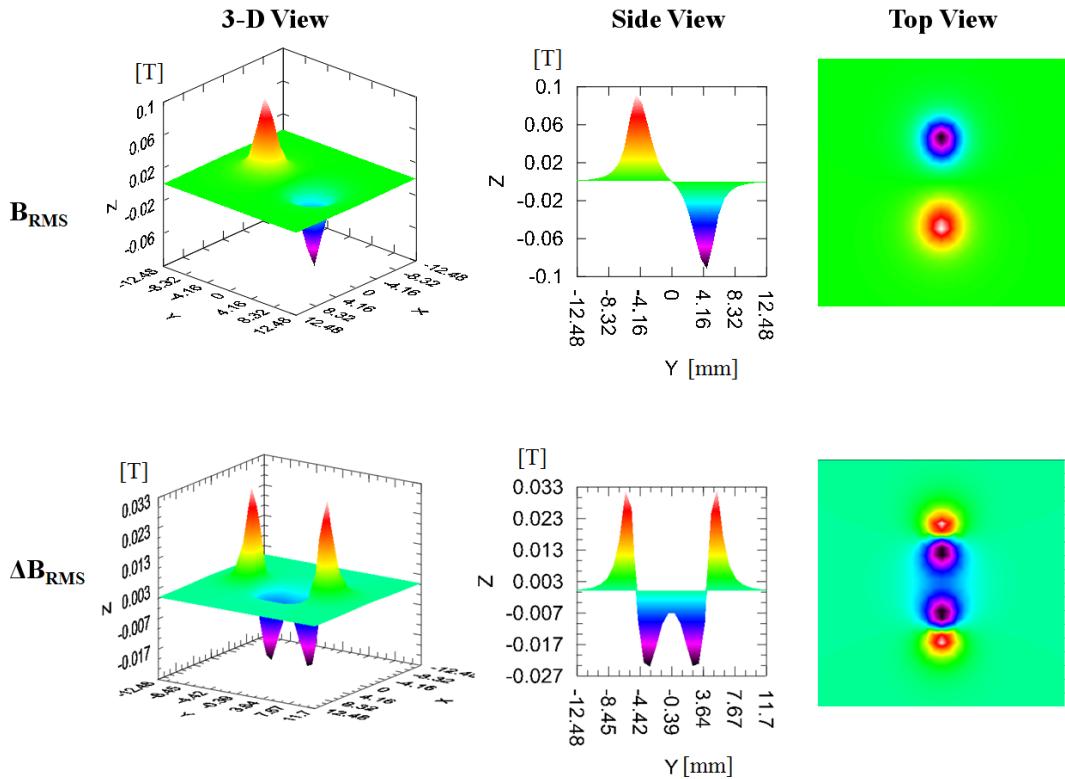
Fig. 3-4 Simulation results for rectangular cross-section crack in dipole model

3.1.3.   Dipole Model of a Triangular crack

Fig. 3-5 shows the dipole model of the triangular cross-section crack, the coordinate system and the distribution of the magnetic charge factor. The magnetic charge factor is uniform on the two side surfaces and varies linearly along the two walls of the crack. Thus, the RMS magnetic charge at point (y', z') on these surfaces can be calculated

- 66 -

by Eq. (3-6), where $\xi_w(y')$ and $\xi(\pm l_c/2)$ are the magnetic charge factors on the wall and at the tips of the crack, respectively [47].
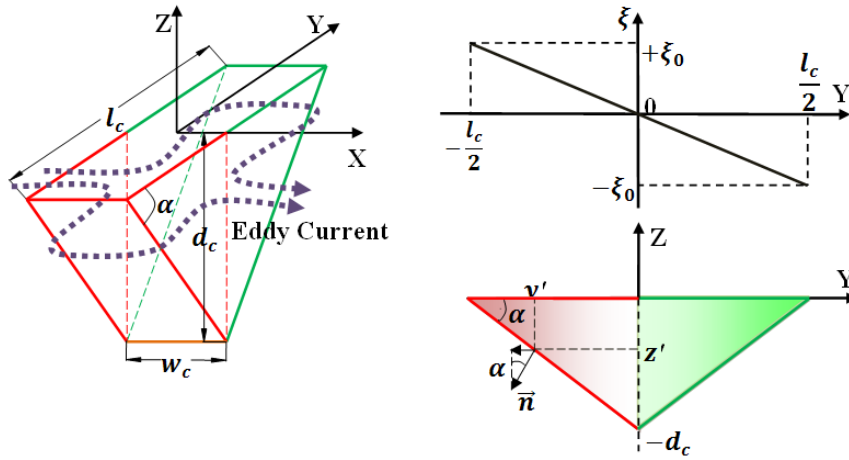
Fig. 3-5 Dipole model of a triangular cross-section crack

$$m_{RMS} = \xi(y') \cdot e^{\frac{z'}{\delta}} \cdot sin\alpha \tag{3-6}$$

$$sin\alpha = d_c / \sqrt{d_c^2 + (l_c/2)^2}$$

$$\xi_w(y') = \pm\xi_0 \cdot \frac{-2y'}{l_c}$$

$$\xi(\pm l_c/2) = \mp\xi_0$$

On the tips of the crack, an element with area $ds = dx' dz'/sin\alpha$ has the amount of magnetic charge dq, is expressed in Eq. (3-7) [47]:

$$dq = m_{RMS} ds = \frac{\xi(\pm l_c/2)e^{\frac{z'}{\delta}} sin\alpha dy' dz'}{sin\alpha} = \xi(\pm l_c/2)e^{\frac{z'}{\delta}} dx' dz' \tag{3-7}$$

The magnetic charge dq induced an RMS magnetic field at point $\vec{r}(x,y,z)$ upper the surface of specimen can be described by Eq. (3-8). Thus, the RMS magnetic field in Z-direction is expressed by Eq. (3-9) [47].

$$d\vec{\boldsymbol{B}} = \frac{\xi(\pm l_c/2)e^{\frac{z'}{\delta}}\vec{\boldsymbol{r}}}{4\pi|\vec{\boldsymbol{r}}|^3}dz'dx' \tag{3-8}$$

$$B_{Tz1} = \frac{\xi_0}{4\pi}\int_{-w_c/2}^{w_c/2}\int_{-d_c}^{0}\frac{e^{\frac{z'}{\delta}}(z-z')}{\left\{(x-x')^2 + (y+\frac{lc}{2d}z'+\frac{lc}{2})^2 + (z-z')^2\right\}^{3/2}}dz'dx' \tag{3-9}$$

$$-\frac{\xi_0}{4\pi}\int_{-w_c/2}^{w_c/2}\int_{-d_c}^{0}\frac{e^{\frac{z'}{\delta}}(z-z')}{\left\{(x-x')^2 + (y-\frac{lc}{2d}z'-\frac{lc}{2})^2 + (z-z')^2\right\}^{3/2}}dz'dx'$$

On the walls of the crack, an element with area $ds = dx'dz'$ has the amount of magnetic charge dq, is expressed in Eq. (3-10) [47]:

$$dq = m_{RMS}ds = \xi_w(y')e^{\frac{z'}{\delta}}sin\alpha dy'dz' = \xi_w(y')e^{\frac{z'}{\delta}}dx'dz' \tag{3-10}$$

The magnetic charge dq induced a RMS magnetic field at point $\vec{\boldsymbol{r}}(x,y,z)$ upper the surface of specimen can be described by Eq. (3-11). Thus, the RMS magnetic field in Z-direction is expressed by Eq. (3-12) [47].

$$d\vec{\boldsymbol{B}} = \frac{\xi_w(y')e^{\frac{z'}{\delta}}\vec{\boldsymbol{r}}}{4\pi|\vec{\boldsymbol{r}}|^3}sin\alpha dz'dx' \tag{3-11}$$

$$B_{Tz2} \tag{3-12}$$

$$= +\frac{\xi_0 sin\alpha}{4\pi}\int_{-l_c/2}^{0}\int_{-2\frac{dc}{lc}y'-dc}^{0}\frac{-2y'}{lc}\frac{e^{\frac{z'}{\delta}}(z-z')}{\{(x+w/2)^2 + (y-y')^2 + (z-z')^2\}^{3/2}}dz'dy'$$

$$+\frac{\xi_0 sin\alpha}{4\pi}\int_{-l_c/2}^{0}\int_{-2\frac{dc}{lc}y'-dc}^{0}\frac{-2y'}{lc}\frac{e^{\frac{z'}{\delta}}(z-z')}{\{(x-w/2)^2 + (y-y')^2 + (z-z')^2\}^{3/2}}dz'dy'$$

$$-\frac{\xi_0 sin\alpha}{4\pi}\int_{0}^{l_c/2}\int_{2\frac{dc}{lc}y'+dc}^{0}\frac{2y'}{lc}\frac{e^{\frac{z'}{\delta}}(z-z')}{\{(x+w/2)^2 + (y-y')^2 + (z-z')^2\}^{3/2}}dz'dy'$$

$$-\frac{\xi_0 sin\alpha}{4\pi}\int_{0}^{l_c/2}\int_{2\frac{dc}{lc}y'+dc}^{0}\frac{2y'}{lc}\frac{e^{\frac{z'}{\delta}}(z-z')}{\{(x-w/2)^2 + (y-y')^2 + (z-z')^2\}^{3/2}}dz'dy'$$

Finally, the total RMS magnetic field at point (x,y,z) (out-of-specimen) in the Z-direction can be calculated by Eq. (3-13) [47].

$$B_{RMS} = B_{Tz1} + B_{Tz2} \tag{3-13}$$

$$= \xi_0 \sum_{i=0}^{1} \frac{(-1)^i}{4\pi} \int_{-w_c/2}^{w_c/2} \int_{-d_c}^{0} \frac{e^{\frac{z'}{\delta}}(z-z')}{\left\{(x-x')^2 + (y+(-1)^i(\frac{l_c}{2d_c}z' + \frac{l_c}{2}))^2 + (z-z')^2\right\}^{3/2}} dz' dx'$$

$$+ \xi_0 \sum_{j=0}^{1} \sum_{i=0}^{1} \frac{\sin\alpha}{4\pi l_c} \int_{(-1)^j l_c/2}^{0} \int_{(-1)^j (2\frac{d_c}{l_c}y' + d_c)}^{0} \frac{e^{\frac{z'}{\delta}}(z-z')(-1)^j 2y'}{\left\{(x+(-1)^i w_c/2)^2 + (y-y')^2 + (z-z')^2\right\}^{3/2}}$$

3.1.4. Simulated Results of a Triangular Crack

The simulation was performed for a triangular cross-section crack, as modeling in Fig. 3-6. The crack has size of $1 \times 10 \times 3$ mm and was simulated in an aluminum alloy (Al7075) plate. The magnetic charge factor, frequency, permeability and electrical conductivity of aluminum alloy are same with those used in the rectangular crack, as shown in Table 2-1.
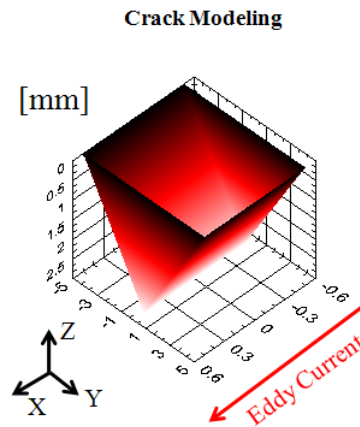
Crack Modeling

Fig. 3-6 Modeling of triangular cross-section crack in dipole model software
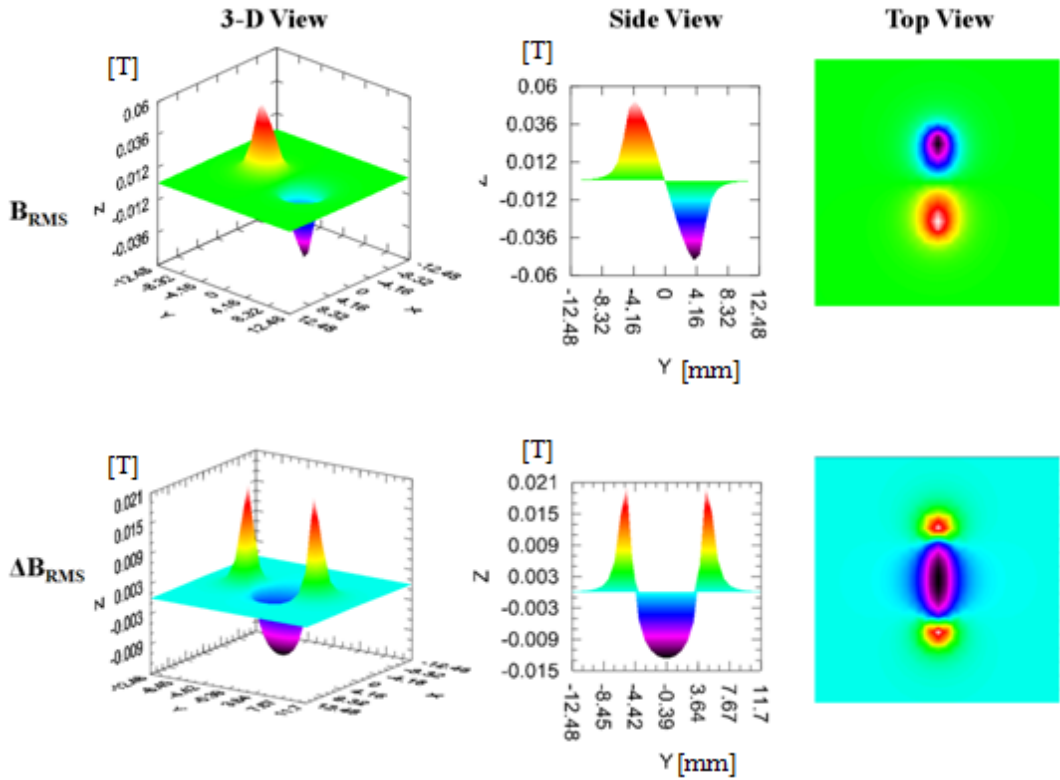
Fig. 3-7 Simulation results for triangular cross-section crack in dipole model

Fig. 3-7 shows the simulation results of the RMS of vertical (Z-component) magnetic flux density (B_{RMS}) and its differential in the Y-direction (ΔB_{RMS}, Eq. (3-5)). In the B_{RMS} image, it has two peaks at the two tips of the crack, which is same with the image of the rectangular crack. However, in the ΔB_{RMS} image, it has three peaks with one negative peak in the middle of two positive peaks. In the both image of B_{RMS} and ΔB_{RMS}, the images are symmetric to the two planes at the center of crack in the both X-axis and Y-axis, because the crack shape is symmetric in these planes.

3.1.5.   Dipole Model of an Elliptical crack

Fig. 3-8 shows the dipole model of the elliptical crack, the coordinate system and the distribution of the magnetic charge factor. The magnetic charge factor is constant on the elliptical surface and varies linearly along the two walls of the crack [47].
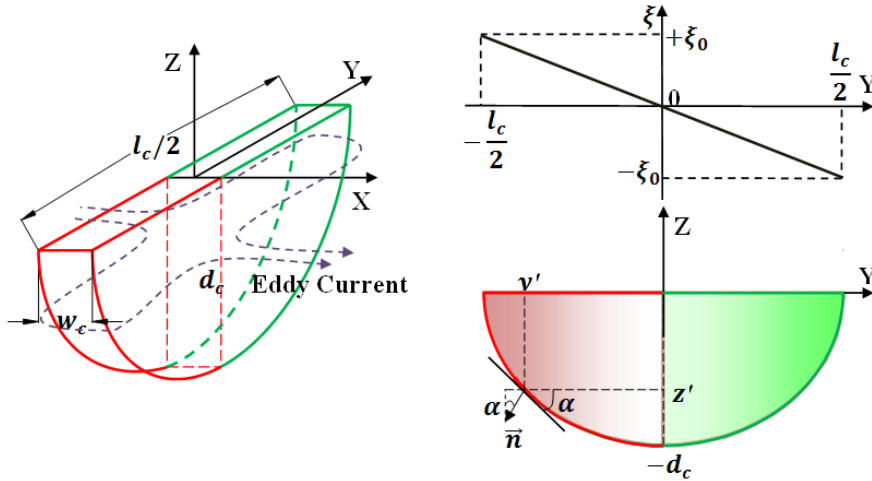
Fig. 3-8 Dipole model of elliptical cross-section crack

Considering, at the point (x', y', z') on the tips of the crack, the magnetic charge is [47]

$$m_{RMS} = \xi_0 e^{\frac{z'}{\delta}} sin\alpha$$

$$tg\alpha = \pm \frac{2dc}{lc}\frac{y'}{z'} \qquad (3\text{-}14)$$

$$sin\alpha = \frac{tg\alpha}{\sqrt{1 + tg^2\alpha}}$$

On the tips, an element with area $ds = dx' dz' /sin\alpha$ has the amount of magnetic charge [47]:

$$(3\text{-}15)$$

$$dq = m_{RMS} ds = \frac{\xi_0 e^{\frac{z'}{\delta}} sin\alpha dy' dz'}{sin\alpha} = \xi_0 e^{\frac{z'}{\delta}} dx' dz'$$

This magnetic charge induced a magnetic field at point $\vec{r}(x, y, z)$ upper the surface of specimen:

$$d\vec{B} = \frac{\xi_0 e^{\frac{z'}{\delta}}\vec{r}}{4\pi|\vec{r}|^3} dz' dx'$$

The total magnetic field at the point $\vec{r}(x, y, z)$ by Z-direction, was induced by magnetic charges at the two surface sides of the crack [47]:

$$B_{Ez1} = \frac{\xi_0}{4\pi}\int_{-w_c/2}^{w_c/2}\int_{-d_c}^{0}\frac{e^{\frac{z'}{\delta}}(z-z')}{\left\{(x-x')^2 + \left(y + \frac{lc}{2}\sqrt{1-(z'/dc)^2}\right)^2 + (z-z')^2\right\}^{3/2}} dz' dx' \qquad (3\text{-}17)$$

$$-\frac{\xi_0}{4\pi}\int_{-w_c/2}^{w_c/2}\int_{-d_c}^{0}\frac{e^{\frac{z'}{\delta}}(z-z')}{\left\{(x-x')^2 + \left(y - \frac{lc}{2}\sqrt{1-(z'/dc)^2}\right)^2 + (z-z')^2\right\}^{3/2}} dz' dx'$$

Magnetic charges appear on the two walls of crack can be described by equation [47]:

$$m_{RMS} = \xi_w(y)e^{\frac{z'}{\delta}}sin\alpha \qquad (3\text{-}18)$$

$\xi(y)$ is a function of variable y. Its value is linear from the center line of the walls. At the center line, $\xi_w(0) = 0$, and at the tips of crack $\xi_w(\pm lc/2) = \pm\xi_0$ as shown in the figure. It can be described by equation [47]:

$$\xi_w(y) = \pm\xi_0\frac{-2y}{lc} \qquad (3\text{-}19)$$

The magnetic field at point $\vec{r}(x, y, z)$ by Z-direction, was induced by magnetic charges on the two walls of crack is [47]:

$$d\vec{B} = \frac{\xi_w(y')e^{\frac{z'}{\delta}}\vec{r}}{4\pi|\vec{r}|^3}sin\alpha dz' dx'$$

B_{Ez2}

$$= +\frac{\xi_0}{4\pi}\int_{-l_c/2}^{0}\int_{-dc\sqrt{1-(2y'/lc)^2}}^{0}\frac{-2y'}{lc}\frac{e^{\frac{z'}{\delta}}(z-z')sin\alpha}{\{(x+w/2)^2 + (y-y')^2 + (z-z')^2\}^{3/2}} dz' dy' \qquad (3\text{-}20)$$

$$+\frac{\xi_0}{4\pi}\int_{-l_c/2}^{0}\int_{-dc\sqrt{1-(2y'/lc)^2}}^{0}\frac{-2y'}{lc}\frac{e^{\frac{z'}{\delta}}(z-z')sin\alpha}{\{(x-w/2)^2 + (y-y')^2 + (z-z')^2\}^{3/2}} dz' dy'$$

$$- \frac{\xi_0}{4\pi} \int_0^{l_c/2} \int_{-dc\sqrt{1-(2y'/lc)^2}}^0 \frac{2y'}{lc} \frac{e^{\frac{z'}{\delta}}(z-z')sin\alpha}{\{(x+w/2)^2 + (y-y')^2 + (z-z')^2\}^{3/2}} dz' dy'$$

$$- \frac{\xi_0}{4\pi} \int_0^{l_c/2} \int_{-dc\sqrt{1-(2y'/lc)^2}}^0 \frac{2y'}{lc} \frac{e^{\frac{z'}{\delta}}(z-z')sin\alpha}{\{(x-w/2)^2 + (y-y')^2 + (z-z')^2\}^{3/2}} dz' dy'$$

Finally, the total RMS magnetic field at point (x, y, z) (out-of-specimen) can be calculated by Eq. (3-21) [47].

$$B_{RMS} = B_{Ez1} + B_{Ez2}$$

B_{RMS}

$$= \xi_0 \sum_{i=0}^1 \frac{(-1)^i}{4\pi} \int_{-w_c/2}^{w_c/2} \int_{-d_c}^0 \frac{e^{\frac{z'}{\delta}}(z-z')}{\left\{(x-x')^2 + (y+(-1)^i\frac{lc}{2}\sqrt{1-(z'/d_c)^2})^2 + (z-z')^2\right\}^{3/2}} dz' dx' \qquad (3\text{-}21)$$

$$+ \sum_{j=0}^1 \sum_{i=0}^1 \frac{1}{4\pi l_c} \int_{(-1)^j l_c/2}^0 \int_{(-1)^j d_c\sqrt{1-(2y'/lc)^2}}^0 \frac{e^{\frac{z'}{\delta}}(z-z')(-1)^j 2y'sin\alpha}{\{(x+(-1)^i w_c/2)^2 + (y-y')^2 + (z-z')^2\}^{3/2}} dz' dy'$$

3.1.6.   Simulated Results of an Elliptical Crack

The simulation was performed for a elliptical cross-section crack, as modeling in Fig. 3-9 . The crack has size of $1 \times 10 \times 3$ mm and was simulated in an aluminum alloy (Al7075) plate. The magnetic charge factor, frequency, permeability and electrical conductivity of aluminum alloy are same with those used in the rectangular crack, as shown in Table 2-1.
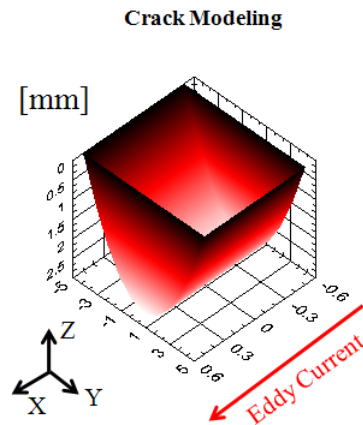
Fig. 3-9 Modeling of elliptical cross-section crack in dipole model software

- 73 -

Fig. 3-10 shows the simulation results of the RMS of vertical (Z-component) magnetic flux density (B_{RMS}) and its differential in the Y-direction (ΔB_{RMS}, Eq. (3-5). In the B_{RMS} image, it also has two peaks at the two tips of the crack, which is same with the image of the rectangular crack and triangular crack. In the ΔB_{RMS} image, it has four peaks with two negative peaks in the middle of the two positive peaks. However, the two negative peaks are connected each other. In the both image of B_{RMS} and ΔB_{RMS}, the images are symmetric to the two planes at the center of crack in the both X-axis and Y-axis, because the crack shape is symmetric in these planes.
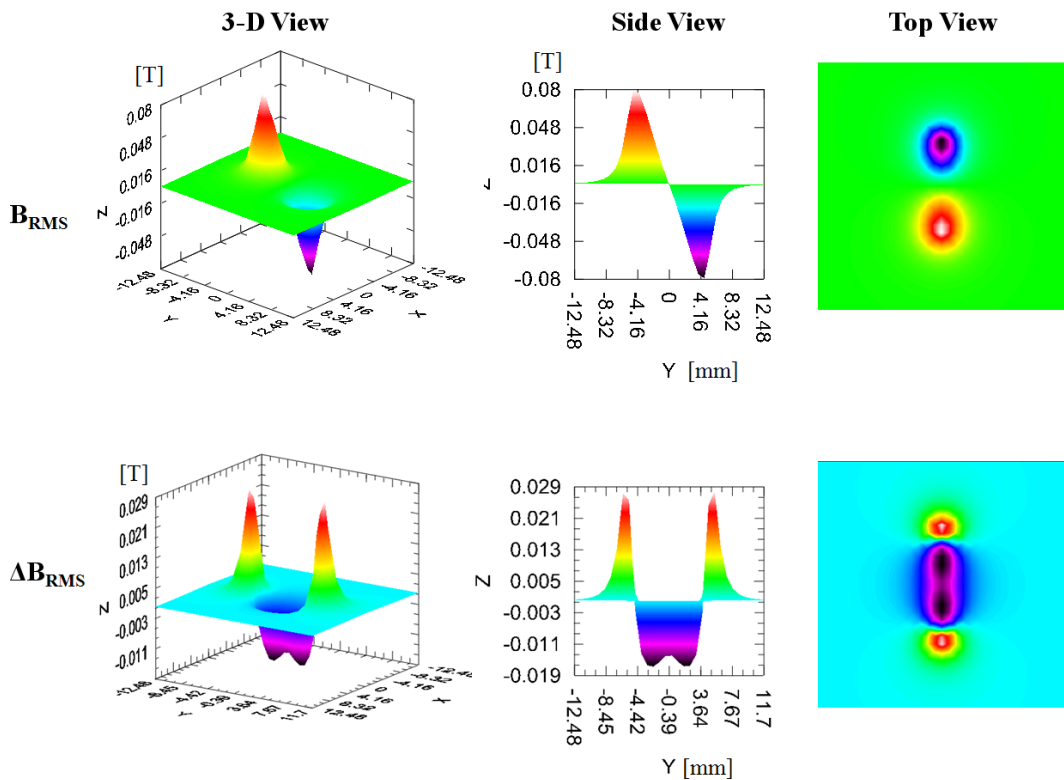
Fig. 3-10 Simulation results for elliptical cross-section crack in dipole model

3.1.7. Dipole Model of a Rectangular Stepped crack

Rectangular stepped crack can be considered to be a combination of many rectangular cracks (Rec_1 and Rec_2). Thus, we can still apply the equations used in the rectangular crack for rectangular stepped crack. Fig. 3-11 shows a model of rectangular stepped crack with one step. The step depth is a half of the maximum depth of the crack. It is considered as combination of two rectangular cracks. The distribution of the magnetic charge factor is shown in the upper of Fig. 3-11 [47].

Fig. 3-11 Dipole model of elliptical cross-section crack

The total RMS magnetic field at point (x, y, z) (out-of-specimen) can be calculated by Eq. (3-22) [47].

$$
\begin{aligned}
B_{SRz} = \Bigg| & \frac{+\xi_0}{4\pi} \int_{-w_c/2}^{w_c/2} \int_{-d_c/2}^{0} \frac{e^{\frac{z'}{\delta}}(z - z')}{\{(x - x')^2 + (y + lc/2)^2 + (z - z')^2\}^{3/2}} dz' dx' \\
& + \frac{\xi_0}{4\pi} \int_{\frac{-l_c}{2}}^{\frac{-l_c + d_c}{2}} \int_{-d_c/2}^{0} \frac{e^{\frac{z'}{\delta}}(z - z')}{\{(x + wc/2)^2 + (y - y')^2 + (z - z')^2\}^{3/2}} \frac{-2y - l_c + d_c}{d_c} dz' dy' \\
& + \frac{\xi_0}{4\pi} \int_{\frac{-l_c}{2}}^{\frac{-l_c + d_c}{2}} \int_{-d_c/2}^{0} \frac{e^{\frac{z'}{\delta}}(z - z')}{\{(x - wc/2)^2 + (y - y')^2 + (z - z')^2\}^{3/2}} \frac{-2y - l_c + d_c}{d_c} dz' dy' \\
& + \frac{\xi_0}{4\pi} \int_{-w_c/2}^{w_c/2} \int_{-d_c}^{-d_c/2} \frac{e^{\frac{z'}{\delta}}(z - z')}{\{(x - x')^2 + y^2 + (z - z')^2\}^{3/2}} dz' dx'
\end{aligned}
$$

(3-22)

$$+\frac{\xi_0}{4\pi}\int_0^{\frac{d_c}{2}}\int_{-d_c}^{-d_c/2}\frac{e^{\frac{z'}{\delta}}(z-z')}{\{(x+wc/2)^2+(y-y')^2+(z-z')^2\}^{3/2}}\frac{-2y+d_c}{d_c}dz'dy'$$

$$+\frac{\xi_0}{4\pi}\int_0^{\frac{d_c}{2}}\int_{-d_c}^{-d_c/2}\frac{e^{\frac{z'}{\delta}}(z-z')}{\{(x-wc/2)^2+(y-y')^2+(z-z')^2\}^{3/2}}\frac{-2y+d_c}{d_c}dz'dy'$$

$$-\frac{\xi_0}{4\pi}\int_{-w_c/2}^{w_c/2}\int_{-d_c}^{0}\frac{e^{\frac{z'}{\delta}}(z-z')}{\{(x-x')^2+(y-lc/2)^2+(z-z')^2\}^{3/2}}dz'dx'$$

$$-\frac{\xi_0}{4\pi}\int_{\frac{l_c}{2}-d_c}^{\frac{l_c}{2}}\int_{-d_c}^{0}\frac{e^{\frac{z'}{\delta}}(z-z')}{\{(x+wc/2)^2+(y-y')^2+(z-z')^2\}^{3/2}}\frac{y-l_c/2+d_c}{d_c}dz'dy'$$

$$-\frac{\xi_0}{4\pi}\int_{\frac{l_c}{2}-d_c}^{\frac{l_c}{2}}\int_{-d_c}^{0}\frac{e^{\frac{z'}{\delta}}(z-z')}{\{(x-wc/2)^2+(y-y')^2+(z-z')^2\}^{3/2}}\frac{2y-l_c+d_c}{d_c}dz'dy'\Biggr]$$

3.1.8.   Simulated Results of a Rectangular Stepped Crack

The simulation was performed for a rectangular stepped cross-section crack, as modeling in Fig. 3-12. The crack has size of $1\times10\times3$ mm and was simulated in an aluminum alloy (Al7075) plate. The step depth is 1.5 mm and the step length is 5 mm. The magnetic charge factor, frequency, permeability and electrical conductivity of aluminum alloy are same with those used in the rectangular crack, as shown in Table 2-1.
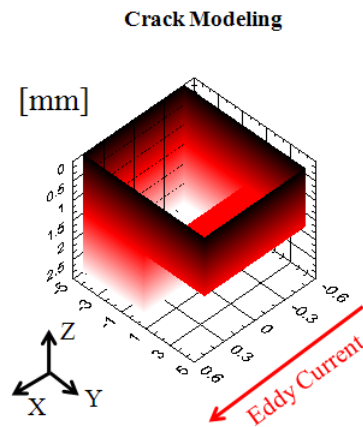
Crack Modeling

Fig. 3-12 Modeling of elliptical cross-section crack in dipole model software

Fig. 3-13 shows the simulation results of the RMS of vertical (Z-component) magnetic flux density (B_{RMS}) and its differential in the Y-direction (ΔB_{RMS}, Eq. (3-5)). In the B_{RMS} image, it also has two peaks at the two tips of the crack, which is same with the image of the rectangular, triangular, and elliptical cracks. However, these two peaks are not equal in absolute value. In the ΔB_{RMS} image, it has four peaks with two negative peaks in the middle of two positive peaks. However, the two negative peaks and the two positive peaks are not equal. This is because, the crack has a step, and then the higher depth part produces higher magnetic field. In the both image of B_{RMS} and ΔB_{RMS}, the images are just symmetric to the one plane at the center of crack in the Y-axis, because the crack shape is symmetric in this plane.
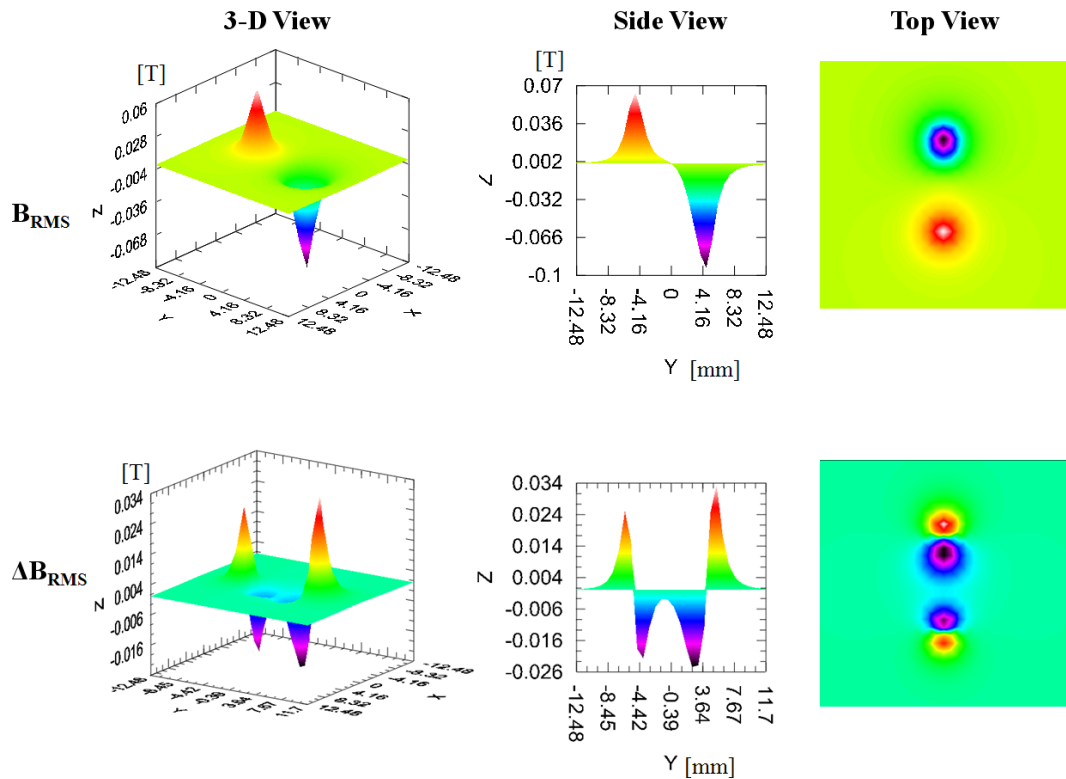
Fig. 3-13 Simulation results for elliptical cross-section crack in dipole model

3.1.9. Dipole Model of a Triangular Stepped crack

Triangular stepped crack can be considered to be a combination of rectangular cracks and triangular cracks. Thus, we can still apply the equations used in the rectangular crack and triangular crack for triangular stepped crack. Fig. 3-14 shows a model of triangular stepped crack with one step. The step depth is 1/3 of the maximum depth of the crack. It is considered as combination of two rectangular cracks (Rec_1 and Rec_2) with one triangular crack (Tri). The distribution of the magnetic charge factor is shown in the upper of Fig. 3-14 [47].
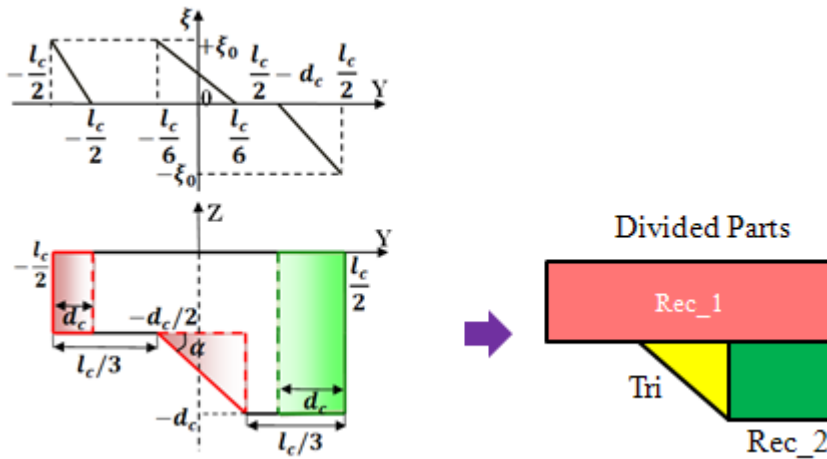
Fig. 3-14 Dipole model of elliptical cross-section crack

The total RMS magnetic field at point (x, y, z) (out-of-specimen) can be calculated by Eq. (3-23) [47].

$$B_{STz} = \left[\frac{+\xi_0}{4\pi} \int_{-w_c/2}^{w_c/2} \int_{-d_{c/2}}^{0} \frac{e^{\frac{z'}{\delta}}(z-z')}{\{(x-x')^2 + (y+lc/2)^2 + (z-z')^2\}^{3/2}} dz' dx' \right. \tag{3-23}$$

$$+ \frac{\xi_0}{4\pi} \int_{\frac{-l_c}{2}}^{\frac{-l_c+d_c}{2}} \int_{-d_{c/2}}^{0} \frac{e^{\frac{z'}{\delta}}(z-z')}{\{(x+wc/2)^2 + (y-y')^2 + (z-z')^2\}^{3/2}} \frac{-2y - l_c + d_c}{d_c} dz' dy'$$

$$+ \frac{\xi_0}{4\pi} \int_{\frac{-l_c}{2}}^{\frac{-l_c+d_c}{2}} \int_{-d_c/2}^{0} \frac{e^{\frac{z'}{\delta}}(z-z')}{\{(x-wc/2)^2 + (y-y')^2 + (z-z')^2\}^{3/2}} \frac{-2y - l_c + d_c}{d_c} dz' dy'$$

$$+ \frac{\xi_0}{4\pi} \int_{-w_c/2}^{w_c/2} \int_{-d_c}^{-d_c/2} \frac{e^{\frac{z'}{\delta}}(z-z')}{\left\{(x-x')^2 + (y+\frac{lc}{3d}z'+\frac{lc}{3})^2 + (z-z')^2\right\}^{3/2}} dz' dx'$$

$$+ \frac{\xi_0 \sin\alpha}{4\pi} \int_{-l_c/6}^{l_c/6} \int_{-\frac{3dc}{2lc}(y'+l/6)-dc/2}^{0} \frac{-3y'}{lc} \frac{e^{\frac{z'}{\delta}}(z-z')}{\{(x+w/2)^2 + (y-y')^2 + (z-z')^2\}^{3/2}} dz' dy'$$

$$+ \frac{\xi_0 \sin\alpha}{4\pi} \int_{-l_c/6}^{l_c/6} \int_{-\frac{3dc}{2lc}(y'+l/6)-dc/2}^{0} \frac{-3y'}{lc} \frac{e^{\frac{z'}{\delta}}(z-z')}{\{(x-w/2)^2 + (y-y')^2 + (z-z')^2\}^{3/2}} dz' dy'$$

$$- \frac{\xi_0}{4\pi} \int_{-w_c/2}^{w_c/2} \int_{-d_c}^{0} \frac{e^{\frac{z'}{\delta}}(z-z')}{\{(x-x')^2 + (y-lc/2)^2 + (z-z')^2\}^{3/2}} dz' dx'$$

$$- \frac{\xi_0}{4\pi} \int_{\frac{l_c}{2}-d_c}^{\frac{l_c}{2}} \int_{-d_c}^{0} \frac{e^{\frac{z'}{\delta}}(z-z')}{\{(x+wc/2)^2 + (y-y')^2 + (z-z')^2\}^{3/2}} \frac{y - l_c/2 + d_c}{d_c} dz' dy'$$

$$\left. - \frac{\xi_0}{4\pi} \int_{\frac{l_c}{2}-d_c}^{\frac{l_c}{2}} \int_{-d_c}^{0} \frac{e^{\frac{z'}{\delta}}(z-z')}{\{(x-wc/2)^2 + (y-y')^2 + (z-z')^2\}^{3/2}} \frac{2y - l_c + d_c}{d_c} dz' dy' \right]$$

3.1.10. Simulation Result of a Triangular Stepped crack

The simulation was performed for a rectangular stepped cross-section crack, as modeling in Fig. 3-15. The crack has size of $1 \times 10 \times 3$ mm and was simulated in an aluminum alloy (Al7075) plate. The step depth is 1.5 mm and the step length is 0.67 mm. The magnetic charge factor, frequency, permeability and electrical conductivity of aluminum alloy are same with those used in the rectangular crack, as shown in Table 2-1.

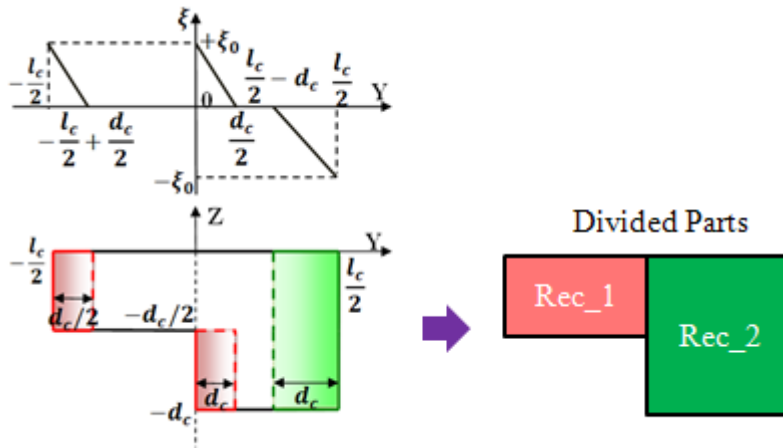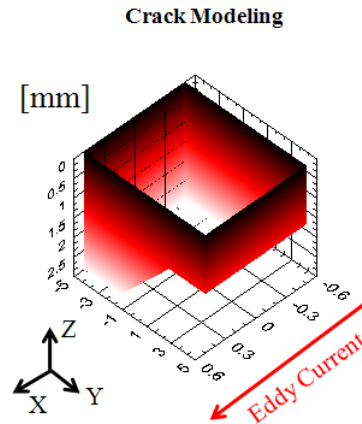**Fig. 3-15** Modeling of elliptical cross-section crack in dipole model software

Fig. 3-16 shows the simulation results of the RMS of vertical (Z-component) magnetic flux density (B_{RMS}) and its differential in the Y-direction (ΔB_{RMS}, Eq. (3-5). The characteristics of the images are very similar to the images of rectangular stepped crack. In the B_{RMS} image, it has two peaks at the two tips of the crack, which is same with the image of the rectangular crack and triangular crack. In the ΔB_{RMS} image, it has four peaks with two negative peaks in the middle of two positive peaks. However, the two negative peaks are connected each other. In the both image of B_{RMS} and ΔB_{RMS}, the images are symmetric to the two planes at the center of crack in the both X-axis and Y-axis, because the crack shape is symmetric in these planes.

3-D View   **Side View**   **Top View**
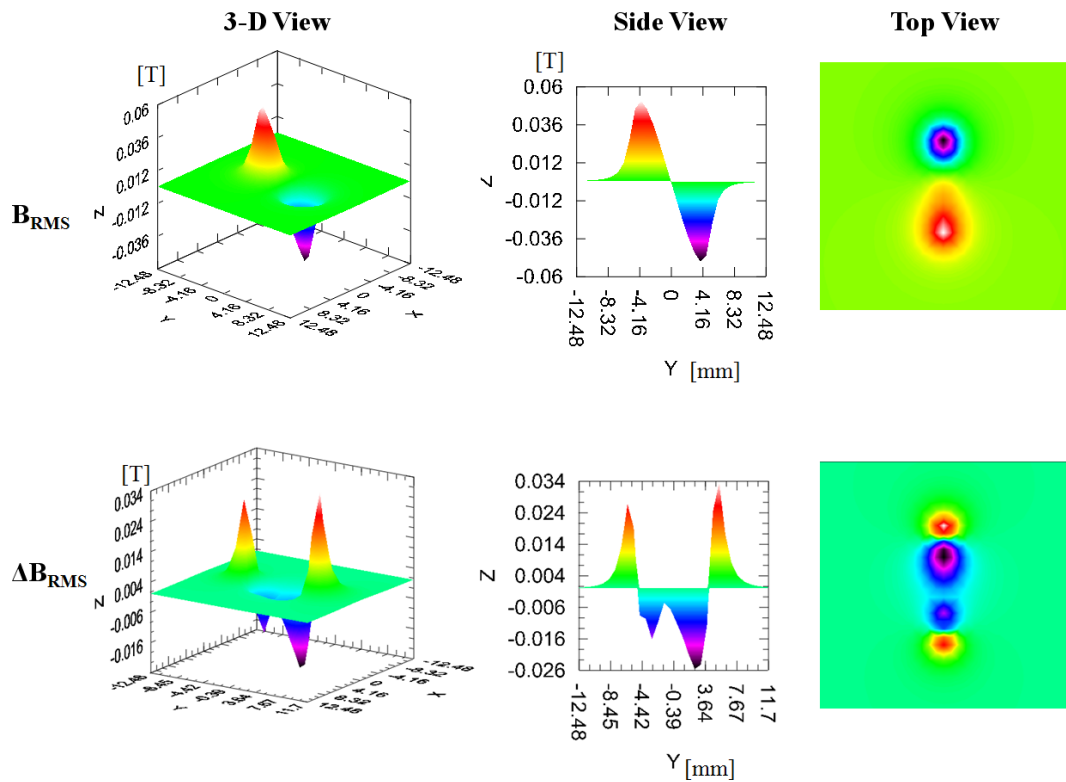
Fig. 3-16 Simulation results for elliptical cross-section crack in dipole model

3.2.   Dipole Model of Cracks on Pipe Specimen

Several numerical analyses have also been conducted for simulation of cracks on small-bore piping systems over the years. Takagi et al. [118], [119] used magnetic vector potential and an edge-based finite element method (FEM) to simulate a multi-coil probe. They also used a quasi-static form of Maxwell's equations for time harmonic fields to simulate a remote field probe. Gotoh et al. [120] used a three-dimensional (3-D) edge-based hexahedral nonlinear FEM to simulate differential search coils. Udpa et al. [121] used reduced magnetic vector potential to simulate a rotated magnetic field. These numerical analyses are extremely useful to analyze ECT probe design and ECT probes signals. However, each component in the simulation needs to be divided into many small elements, and these methods use many relative equations. Thus, these methods are

complicated, computer-intensive and time-consuming. In this section, we propose the DM for the simulation of the AMF around an ODSCC on a small-bore piping system. Good agreement between the results of this method and those obtained using the FEM and a BMC are discussed in next chapter. Furthermore, it is shown that crack volumes can be estimated using the proposed method.

3.2.1. Distribution of Magnetic Charge

Fig. 3-17 shows model of a hole-type crack on a conductive pipe. The model is same with one which is presented in the Chapter 2 and Chapter 3. When an alternating current is supplied to the bobbin coil, an eddy current is induced in the conductive pipe. The eddy current approaches a hole-type crack, it distorts around the crack, as shown in the FEM simulation result in Fig. 3-18. The eddy current flow was obstructed by a crack and diverted around the crack. It is diffused at the terminals and highly concentrated at the two side of the crack. Thus, the eddy current intensity depends on the orientation angle (φ) which indicates the position of the eddy current around the hole crack. In addition, the eddy current intensity also depends on the distance to the surface of the material, which is well known as the "skin effect". In the dipole model, we assumed that magnetic charges appear on the wall of the hole, and they depend on the eddy current intensity. Thus, the magnetic charge at a depth (t) from the surface of the material and orientation angle (φ), can be described by Eq. (3-24) [45], [49].
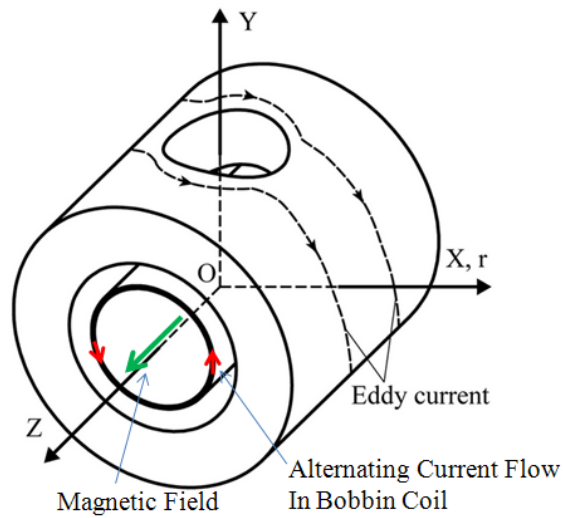
Fig. 3-17 Model of a hole-type crack on a conductive pipe
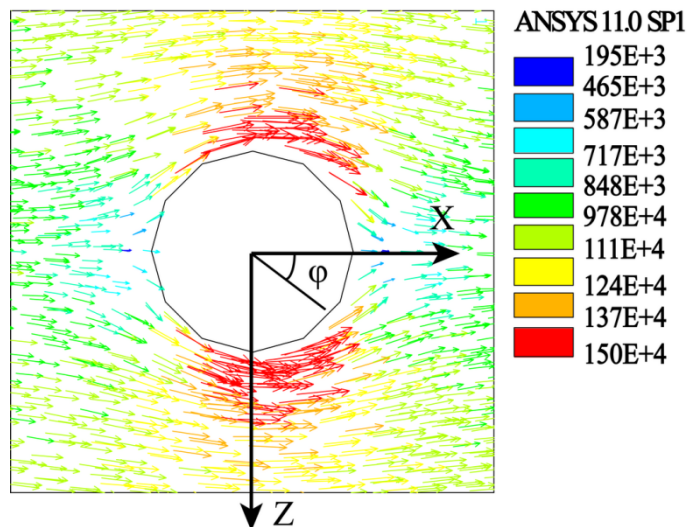
Fig. 3-18 Eddy current flow around a 1.5 mm-diameter through-hole-type crack in a conductive pipe simulated in ANSYS software.

$$m = \xi e^{-\frac{t}{\delta}} sin\varphi, \qquad\qquad \delta = \frac{1}{\sqrt{\pi f \mu \sigma}} \qquad\qquad (3\text{-}24)$$

where ξ, δ, f, μ, and σ are the magnetic charge factor, skin depth, frequency, absolute permeability and electrical conductivity of the specimen, respectively.
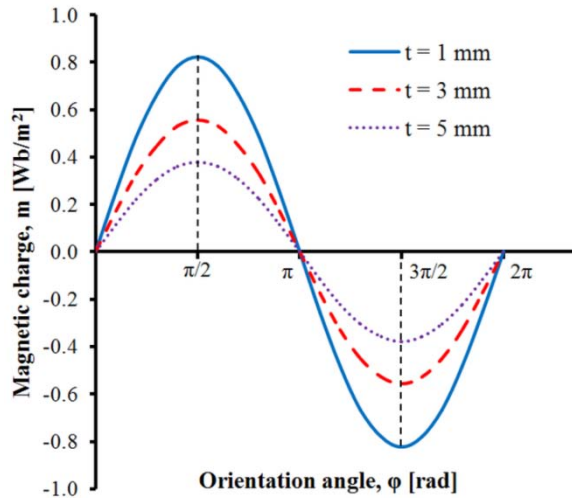
Fig. 3-19 Magnetic charge depends on the skin effect and orientation angle (φ) in Eq. (1) with $\delta = 5.132$ and $\xi = 1$.

The change in the magnetic charge due to the skin depth in the skin effect and the orientation angle in Eq. (3-24) is shown in Fig. 3-19. The skin depth of titanium material at 5 kHz is 5.132 mm, and we assumed the magnetic charge factor $\xi = 1$ Wb/m². Deeper into the material, the magnetic charge decreases due to the skin effect. The magnetic charge attains maximum and minimum values at the right side ($\varphi = \pi/2$) and left side ($\varphi = 3\pi/2$) of the eddy current flow, respectively, and it is zero at the terminals of the distorted eddy current flow ($\varphi = 0, \pi$) [45], [49].

- 84 -

3.2.2. Calculations

There are four types of SCC commonly appear in a piping system: through-hole-type, OD normal-hole-type, ID normal-hole-type and OD complicated-type shape. The models of four types SCC are shown in Fig. 3-20. The each type of SCC is matched with each condition in Eqs. (3-25)–(3-28) [45], [49]. A "through crack" is a crack with a depth larger than the pipe thickness (Eqs. (3-25)), as shown in Fig. 3-20(a). If a crack is located on the outer diameter surface and satisfies Eq. (3-26) or (3-27), it is an OD crack or a complicated OD crack, respectively, as shown in Fig. 3-20 (b), (c). If the crack is located on the inner diameter surface (Eq. (3-28)), it is an ID crack, as shown in Fig. 3-20 (d).

Through	$R_O - R_I \leq d$	(3-25)
OD	$w < 2\sqrt{R_O{}^2 - (R_O - d)^2}$	(3-26)
Complicated OD	$w \geq 2\sqrt{R_O{}^2 - (R_O - d)^2}$	(3-27)
ID	$R_O - R_I > d$ & $inner\ diameter$	(3-28)

where R_O, R_I, R_S, d, and w are, respectively, the outer and inner radii of the pipe, the sensor diameter, and the depth and diameter of the hole-type crack.

Collection @ chosun
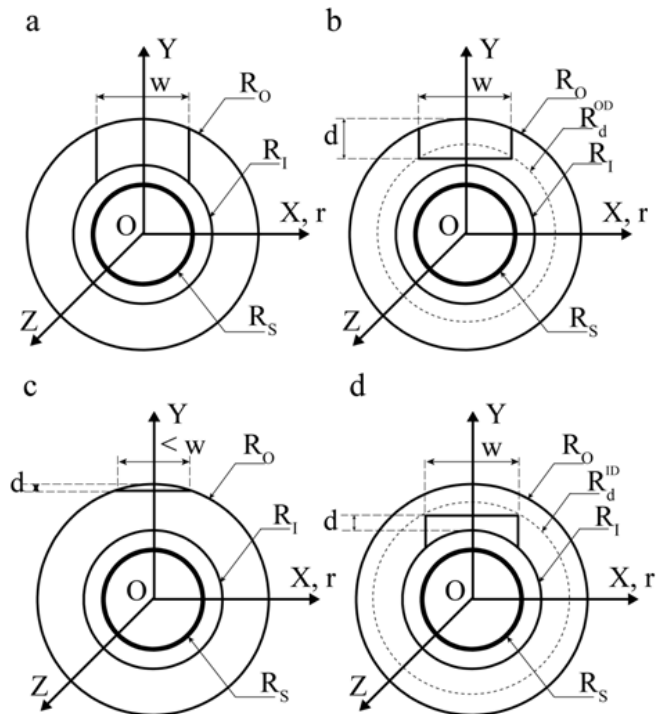
Fig. 3-20 Four hole-type cracks: (a) through, (b) OD, (c) Complicated OD, and (d) ID.
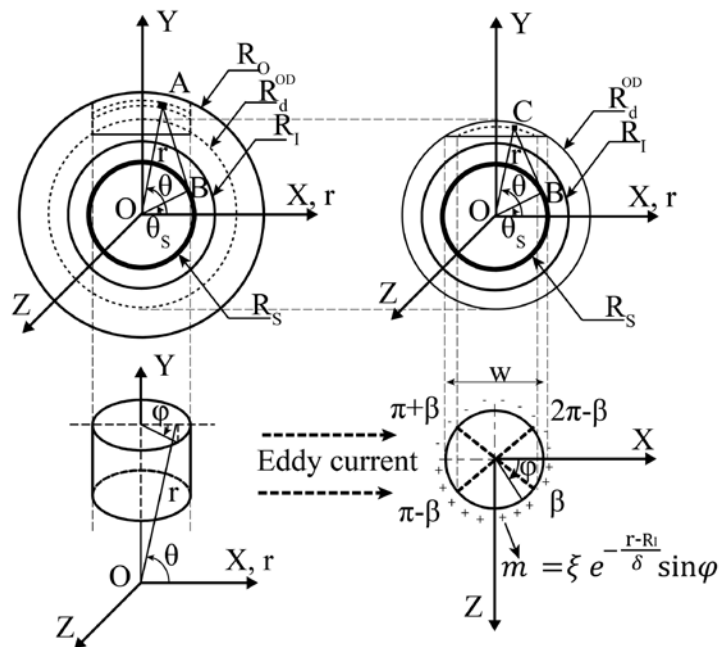
Fig. 3-21 Dipole model of OD crack in a pipe.

$$m = \xi\, e^{-\frac{r-R_I}{\delta}} \sin\varphi$$

3.2.2.1. Hole-type outer diameter crack (OD)

Let's first consider the OD crack shown in Fig. 3-21; by defining the relevant equations for this crack in the both the Cartesian (X, Y, Z) and cylindrical coordinate systems (r, θ, Z), we will have a basis to develop corresponding equations for the other types of cracks. By superposing constituent magnetic fields, the magnetic charges in the crack wall surface can be divided into two areas: one that is bounded by R_O and R_d^{OD} and a second area bounded by R_d^{OD} and the bottom area of the crack. As described by Eq. (5), magnetic charges located at points A and C within these respective areas generate an axial magnetic field $(B_r^A$ and B_r^C, respectively, in the OB direction) at point B in the sensing area. The radial magnetic field B_r^A and B_r^C are calculated by Eq.

(3-30) and Eq. (3-31), respectively. Finally, the radial magnetic field of OD crack is calculated by Eq. (3-36) [45], [49].

$$B_r^{OD} = B_r^A + B_r^C \tag{3-29}$$

$$B_r^A = \int_0^{2\pi} \int_{R_d^{OD}}^{R_O} F \, dr d\varphi \tag{3-30}$$

$$B_r^C = \int_\beta^{\pi-\beta} \int_{R_O-d}^{R_d} F \, dr d\varphi + \int_{\pi+\beta}^{2\pi-\beta} \int_{R_O-d}^{R_d^{OD}} F \, dr d\varphi = \sum_{i=0}^{i=\pi} \int_{i+\beta}^{i+\pi-\beta} \int_{R_O-d}^{R_d^{OD}} F \, dr d\varphi \tag{3-31}$$

$$F = \frac{1}{4\pi} \frac{w}{2} \frac{\xi e^{-\frac{(r-R_I)}{\delta}} \sin\varphi [r\cos(\theta-\theta_s) - R_s]}{[(\frac{w}{2}\sin\varphi - z_s)^2 + r^2 + R_s^2 - 2rR_s\cos(\theta-\theta_s)]^{3/2}} \tag{3-32}$$

$$\theta = \frac{\pi}{2} - \arctan\left(\frac{w}{2}\cos\varphi / \sqrt{\left[r^2 - (\frac{w}{2}\cos\varphi)^2\right]}\right) \tag{3-33}$$

$$R_d^{OD} = \sqrt{(R_O - d)^2 + (w/2)^2} \tag{3-34}$$

$$\cos\beta = 2\sqrt{[r^2 - (R_O - d)^2]}/w \tag{3-35}$$

$$B_r^{OD} = \int_0^{2\pi} \int_{R_d^{OD}}^{R_O} F \, dr d\varphi + \sum_{i=0}^{i=\pi} \int_{i+\beta}^{i+\pi-\beta} \int_{R_O-d}^{R_d^{OD}} F \, dr d\varphi \tag{3-36}$$

- 87 -

where $(r, \theta, w/2\sin\varphi)$ and (R_s, θ_s, z_s) are the coordinates in the cylindrical coordinate system of points A or C on the crack wall and of point B in the sensing area, respectively.

3.2.2.2. Hole-type through crack (through)

Fig. 3-22 shows the dipole model for a through-hole-type crack in a pipeline. To develop similar equations for the through crack, the area bounded by R_O and R_I (the first area) is used. This magnetic field at point B can be described by Eq. (3-37) [45], [49].
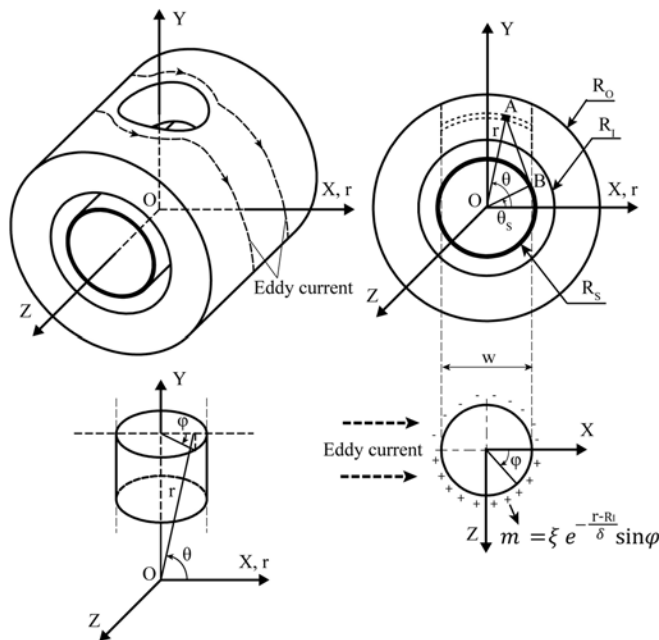
Fig. 3-22 Dipole model of a through- hole-type crack in a pipeline

$$B_r^{Thr} = \int\limits_{0}^{2\pi} \int\limits_{R_I}^{R_O} F \, dr d\varphi \tag{3-37}$$

3.2.2.3. Hole-type complicated OD crack (COD)

Fig. 3-23 shows the dipole model for a complicated OD crack in a pipeline. For the complicated OD crack, only the area bounded by R_O and the crack bottom (second area) is used. In this case, the magnetic field at point B is described by Eq. (3-38) [45], [49].

- 88 -
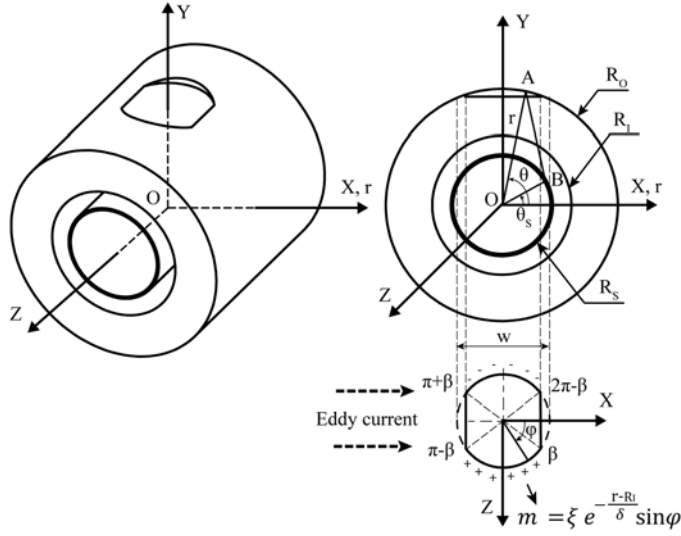
Fig. 3-23 Dipole model of an OD complicated-type crack in a pipeline

$$B_r^{COD} = \int_\beta^{\pi-\beta} \int_{R_O-d}^{R_O} F\, dr d\varphi + \int_{\pi+\beta}^{2\pi-\beta} \int_{R_O-d}^{R_O} F\, dr d\varphi = \sum_{i=0}^{i=\pi} \int_{i+\beta}^{i+\pi-\beta} \int_{R_O-d}^{R_O} F\, dr d\varphi \tag{3-38}$$

3.2.2.4. Hole-type inner diameter crack (ID)

Finally, for the ID crack, the effective magnetic charge area can be modeled by subtracting the area bounded by R_d^{ID} and R_I from the area bounded by R_d and the crack bottom area. The magnetic field at point B can then be described by Eq. (3-39) [45], [49].

$$B_r^{ID} = \int_0^{2\pi} \int_{R_I}^{R_d^{ID}} F\, dr d\varphi - \int_\beta^{\pi-\beta} \int_{R_I+d}^{R_d^{ID}} F\, dr d\varphi - \int_{\pi+\beta}^{2\pi-\beta} \int_{R_I+d}^{R_d^{ID}} F\, dr d\varphi$$

$$= \int_0^{2\pi} \int_{R_I}^{R_d^{ID}} F\, dr d\varphi - \sum_{i=0}^{i=\pi} \int_{i+\beta}^{i+\pi-\beta} \int_{R_I+d}^{R_d^{ID}} F\, dr d\varphi \tag{3-39}$$

$$R_d^{ID} = \sqrt{(R_I + d)^2 + (w/2)^2} \tag{3-40}$$

3.2.3. Simulated Results of Cracks on a Pipe

Fig. 3-24 - Fig. 3-28 show samples simulation result of the four types crack at 5 kHz of excitation frequency. The cracks were simulated on a titanium pipe which has inner diameter of 17.28 mm and outer diameter of 19 mm. The bobbin sensor have diameter of 15 mm respect to the lift-off of 1.14 mm between sensor and the inner surface of the pipe. The meshing grid size of the bobbin sensor is 0.78 mm equivalent to the meshing element size of the bobbin sensor in the FEM. The size of sensor and pipe were same with them in the FEM. The four cracks have same diameter of 4 mm and the depth of 0.86, 0.43, 0.43 and 0.15 respect to the through, OD, ID and COD crack. The depth of cracks is satisfied the condition of each crack type. The COD crack is calculated having depth smaller than 0.21 mm. The detail simulated parameters are shown in the Table 3-2.

Table 3-2 Simulated parameters

Conditions	Simulated parameters	Values
Titanium pipe size	Inner diameter	17.28 mm
	Outer diameter	19 mm
Properties of pipe	Absolute permeability (μ)	1.2566×10^{-6} H/m
	Electrical conductivity (σ)	1.92×10^{6} S/m
Bobbin sensor size	Diameter	15 mm
	Length	24.96 mm
Lift-off	z	1.14 mm
Crack size	Through	Ø4×0.86 mm
	OD	Ø4×0.43 mm
	ID	Ø4×0.43 mm
	COD	Ø4×0.15 mm
Frequency	f	5 kHz
Magnetic charge factor	ξ	1 Wb/m^2
Spatial resolution of the bobbin sensor	Meshing grid size of the software	0.78 mm

3-D View   **Side View**   **Top View**
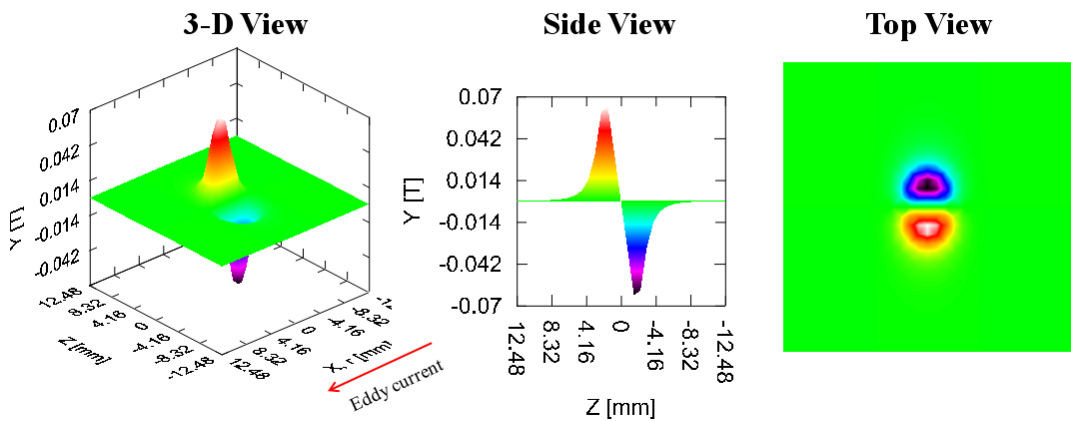
Fig. 3-24 Simulation result of a hole-type through crack

3-D View   **Side View**   **Top View**
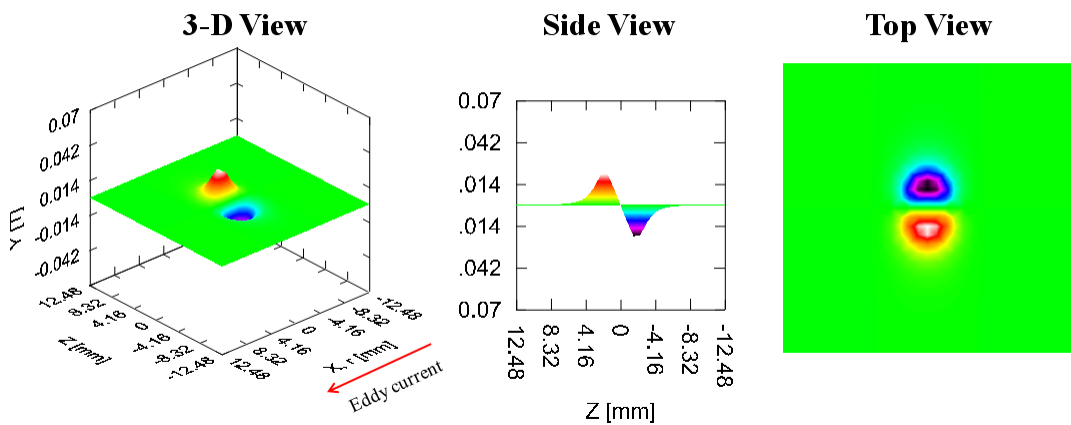
Fig. 3-25 Simulation result of a hole-type OD crack
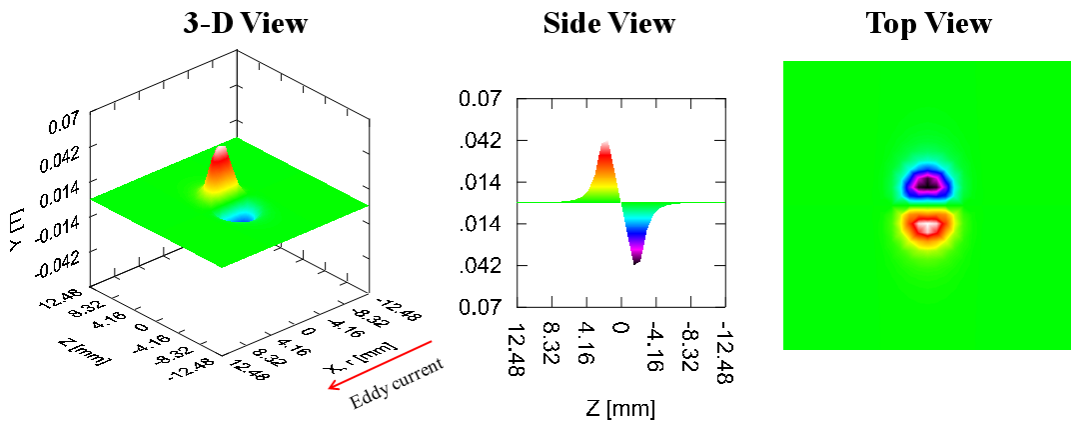
Fig. 3-26 Simulation result of a hole-type ID crack
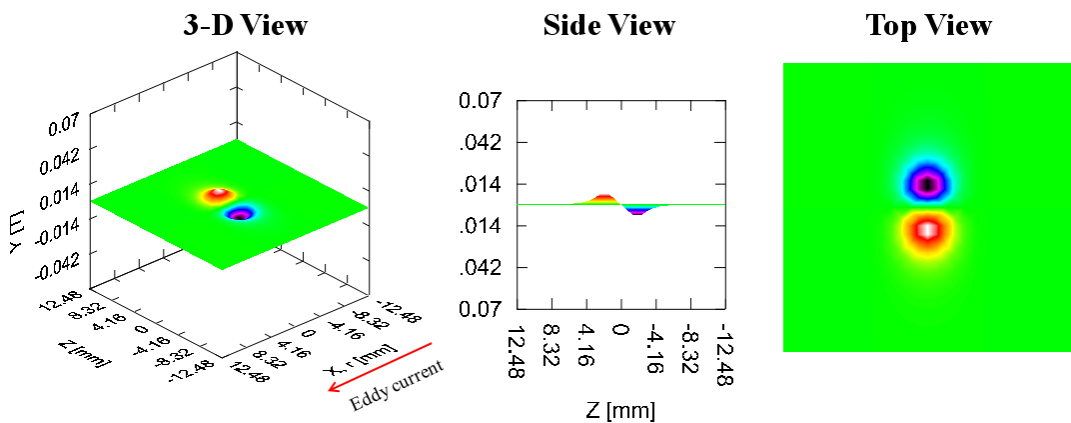
Fig. 3-27 Simulation result of a hole-type COD crack

Fig. 3-28 shows simulation result of the four types crack in the same scale of contour plot and section view plot. The crack images have one positive peak and one negative peak. The images are symmetric due to the symmetric of the crack which are hole-types. The zero cross between the two peaks indicate the center of the crack. We can see clearly the increase of magnetic field due to the increase of the crack depth. Particularly, the OD and ID cracks have same size but the strength of magnetic field is quite different. In the OD crack, it is much smaller than it in the ID crack because the OD

crack is far the sensor than the ID crack, and the OD crack located deeper than the ID crack does in the skin effect.
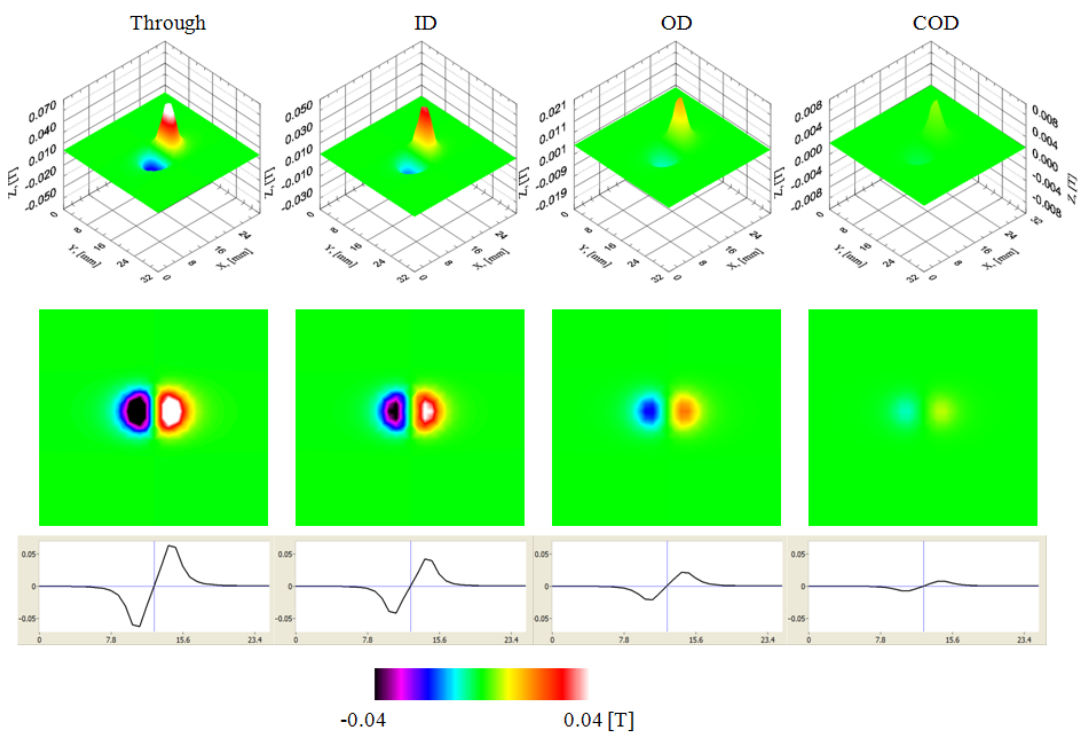
Fig. 3-28 Simulation result of four hole-types crack on a pipe

3.3.   Dipole Model Software

3.3.1. Dipole Model Analysis Software

Dipole model analysis software is able to analyze electromagnetic field distribution around cracks based on dipole model. The dipole magnetic charges are assumed to be appeared around a crack due to the distribution of electromagnetic field (alternating or static field). These dipole magnetic charges induced a magnetic field around the crack which is magnetic flux leakage (MFL) in the case of static field, or alternating magnetic field based on eddy current flow in the case of alternating field. The software has three options of magnetization methods which are horizontal and vertical magnetization in the case of static field, and eddy current in the case of alternating field. Two options of sensors also integrated in the software, which are Hall sensor and magneto-optical sensor to simulate magnetic camera and magneto-optical camera, respectively. Using DM, the simulation becomes easier and faster than using traditional method - FEM. Multiple cracks with different shapes (rectangle, triangle, ellipse, hole, and step) on a flat specimen can be analyzed at the same time for the both MFLT and ECT methods. Furthermore, the hole-type cracks on the surface of inner or outer of pipeline (through, OD, COD, and ID) can be simulated. Crack size, specimen properties and experimental conditions also integrated in the software. The software has three modes: pre-processor (Fig. 3-29), solve (simulation) (Fig. 3-30), and post-processor (Fig. 3-31), and analysis mode. In the post-processor mode, several window forms (Fig. 3-32) can be used for to data processing in the 2D view, 3D view, and crack evaluations.
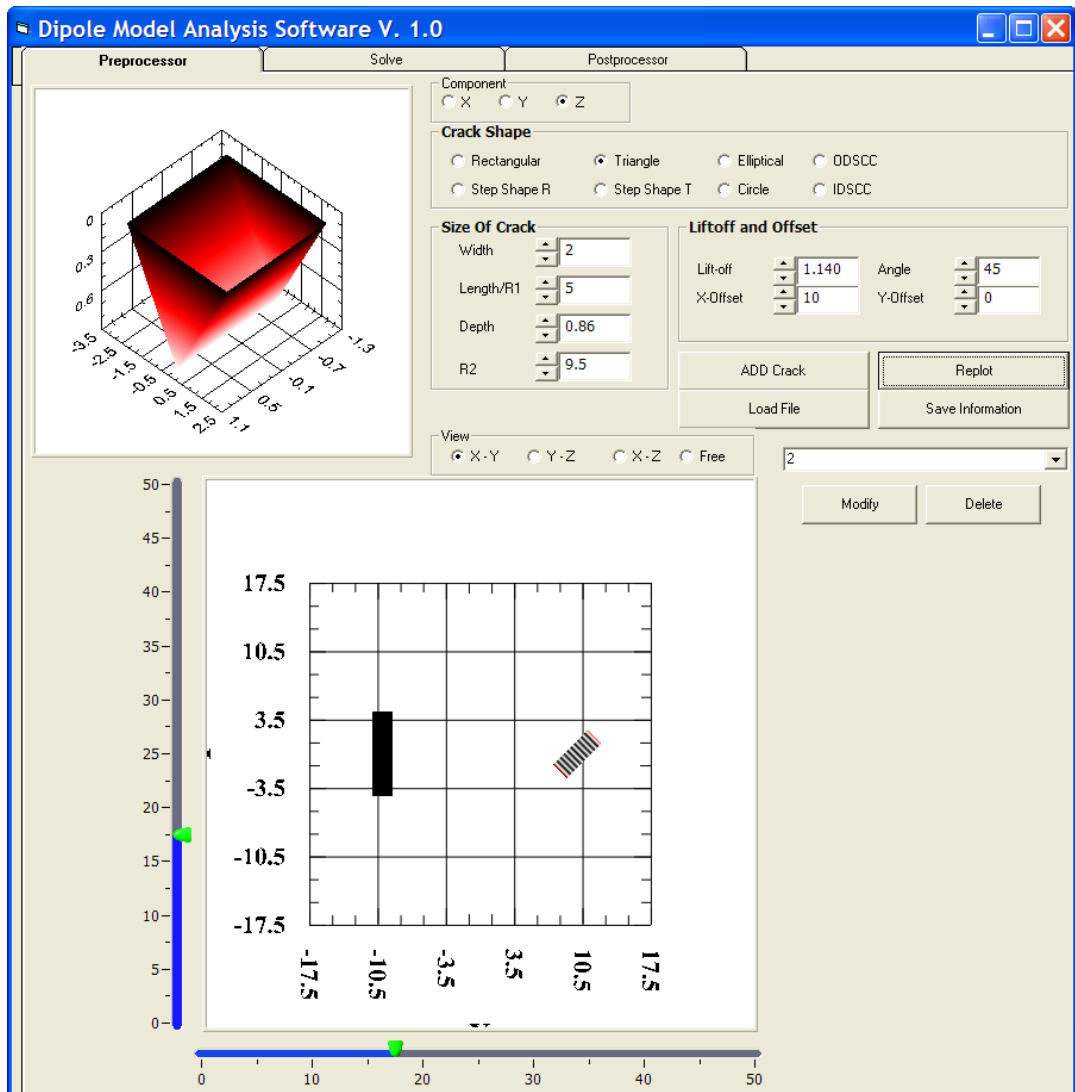
Fig. 3-29 Dipole model software: Pre-processor mode

Pre-processor Mode:

- Select shape of crack as rectangular, triangular, Elliptical, Stepped Rectangular, Stepped Triangular, Circle, ODSCC and IDSCC shapes.

- Input size of crack, and inner and outer diameter of pipeline in the case of ODSCC and IDSCC. Input offset position, angle of crack and lift-off of sensor.
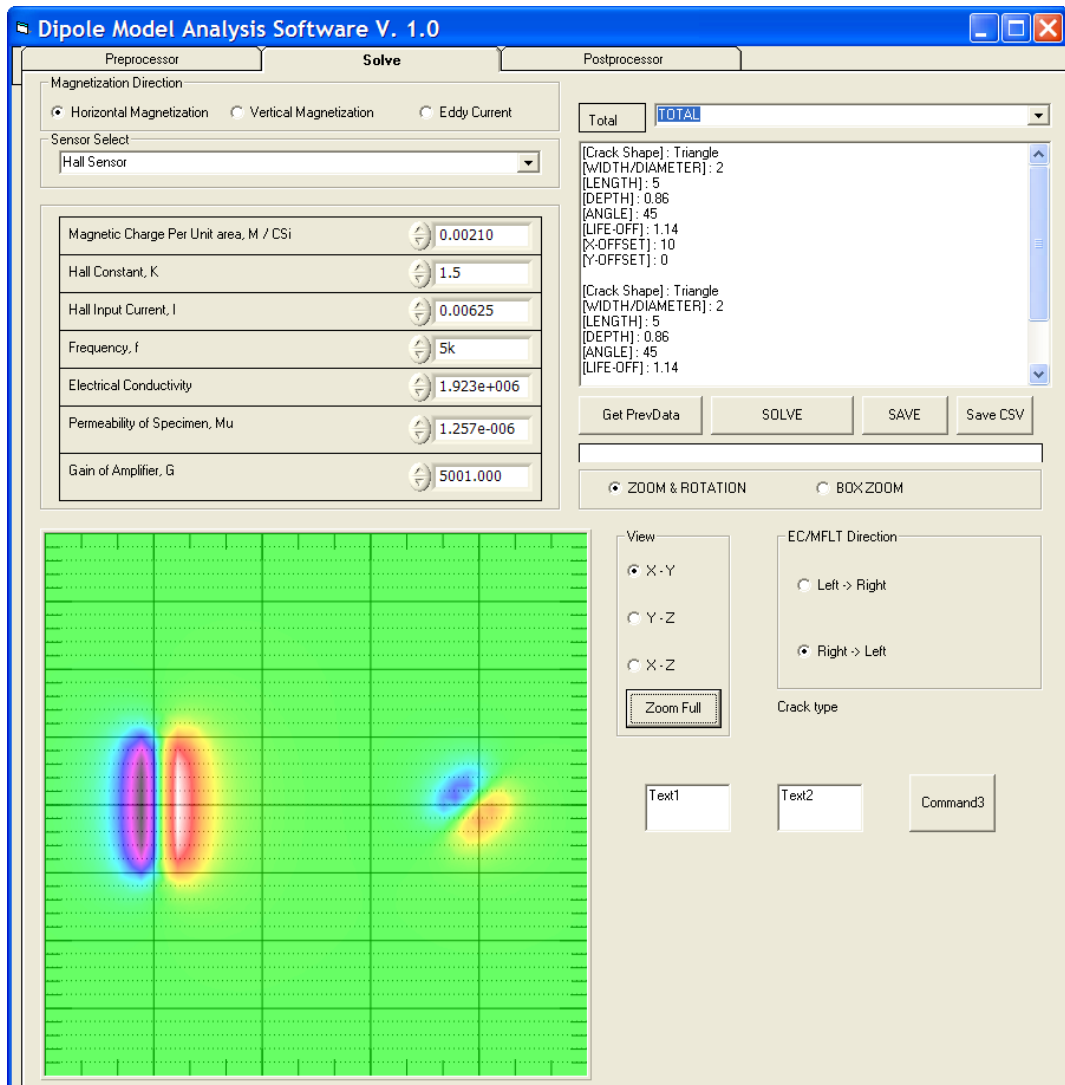
Fig. 3-30 Dipole model software: Solve (Simulation) mode

Solve (Simulation) Mode:

- Choose magnetization direction as horizontal magnetization, vertical magnetization or eddy current. Select type of sensor which is Hall sensor or magneto-optical sensor.

- Input magnetic properties of specimen (permeability and conductivity), frequency (in the case of eddy current), and magnetic charge per unit area. In the case of Hall sensor, we can choose Hall constant, Hall input current and amplifier gain also. In

the case of magneto-optical sensor, we choose saturated magnetic field of sensor, bias magnetic field and temperature of experimental environment.

- After choosing all parameters, start and save the data of simulation.
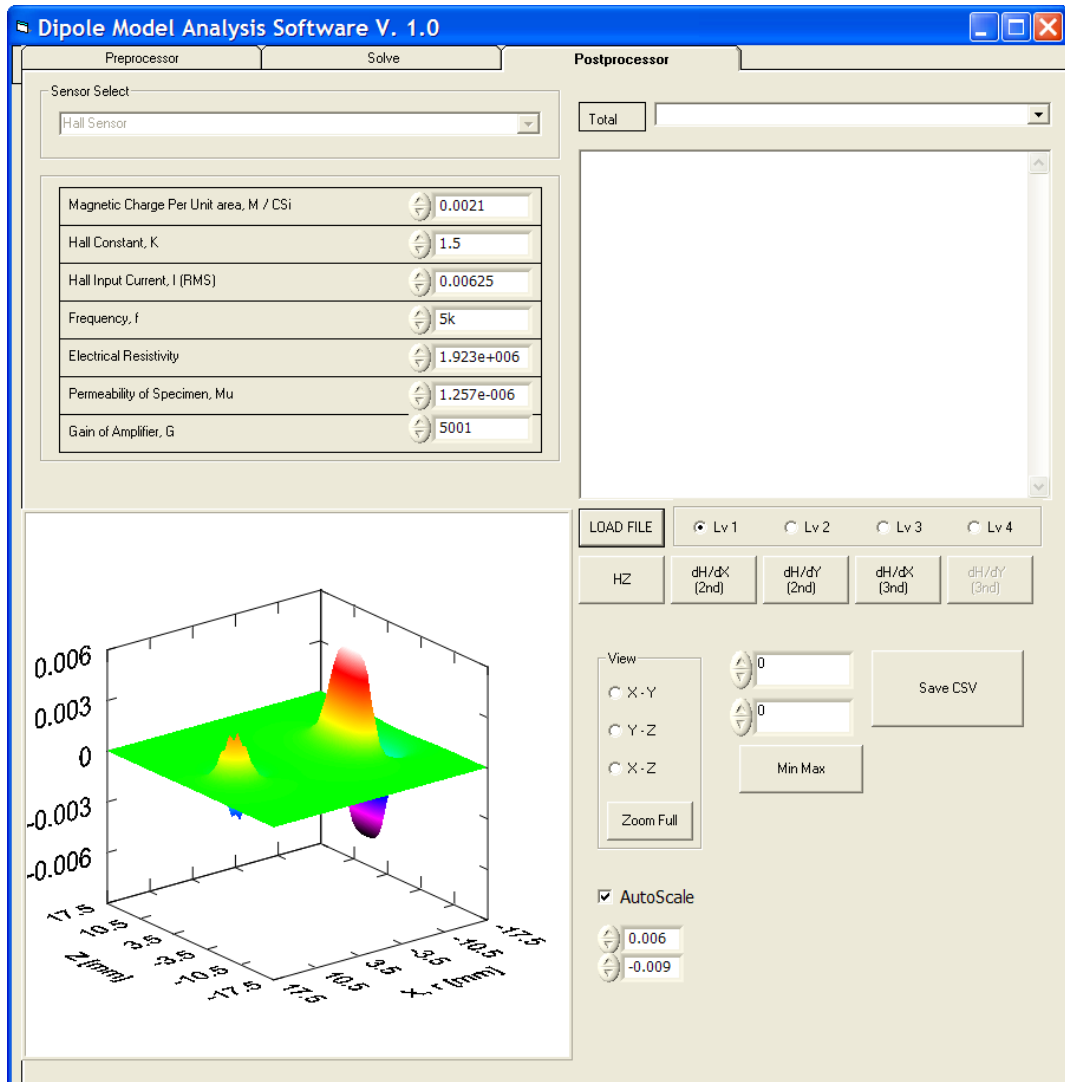
Fig. 3-31 Dipole model software: Post-processor mode
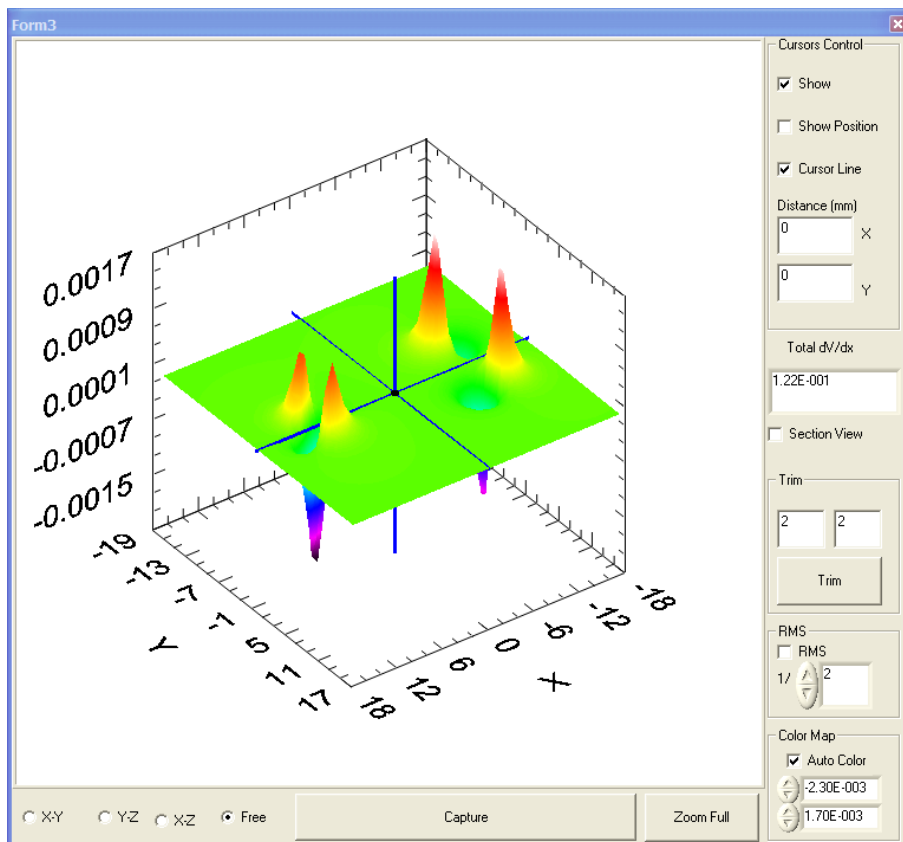
Fig. 3-32 Dipole model software: Post-processor mode (quantitative)

Post-processor Mode:

- We can open solved simulation data and process the data with some differential functions (dH/dX, dH/dY,...). Also quantitative the crack also can be operated in this mode.

3.3.2. Dipole Real-time Simulation Software

The simulation software has been developed by using Microsoft Visual Studio 2008, C# language with integrated of NI Measurement Studio 2009 Tools [49]. The software is able to simulate the scanning state of a bobbin-type magnetic camera. The software has two main modes: Modeling/Simulation and Post-processing mode.

The interface of Modeling/Simulation mode is shown in Fig. 3-33 [49]. The properties of pipe specimen, crack, Hall sensor and maximum magnetic charge factor are input in this mode. The detail properties of each component are listed in the Table 3-3. There is one option for using effective region method with input value of percentage of maximum value of crack image ('Err % of Max'). The sizes of crack are listed in a list and they can be editable. A color indicator helps to indicate selected of modeled crack respect to its size in the crack list. After modeling, we perform simulation in the same window in Fig. 3-33. The normal voltage, differential in X- direction, differential in Y-direction and section view are displayed same time during scanning simulated. We can unselect the data display for a faster simulation.

Table 3-3 Properties of each component in Modeling/Simulation mode

Pipe specimen	Sensor	Crack	Simulation Parameters
• Inner diameter • Outer Diameter • Length	• Diameter • Spatial Resolution • Number of sensors (relate to diameter and spatial resolution)	• Center position in axial direction • Diameter • Depth • Location: OD/ID/Through (auto calculate respect to pipe thickness, crack diameter and crack depth)	• Maximum magnetic charge factor • Frequency • Scan step • Input current for Hall sensor • Hall constant Amplifier gain of amplifier circuit
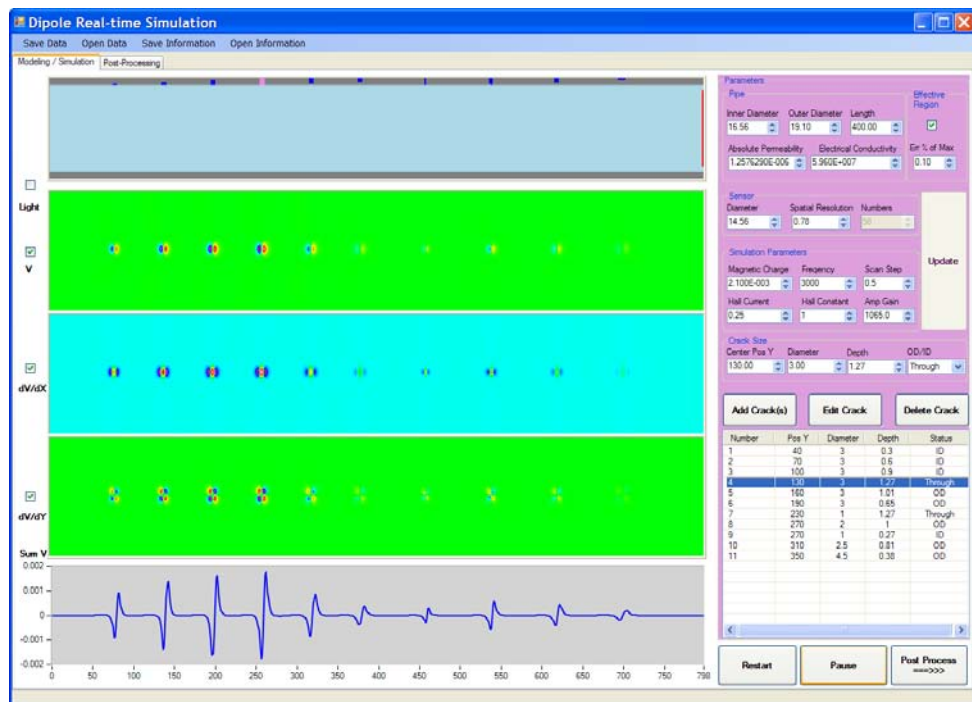
Fig. 3-33 Dipole real-time simulation software: Modeling/Simulation mode.
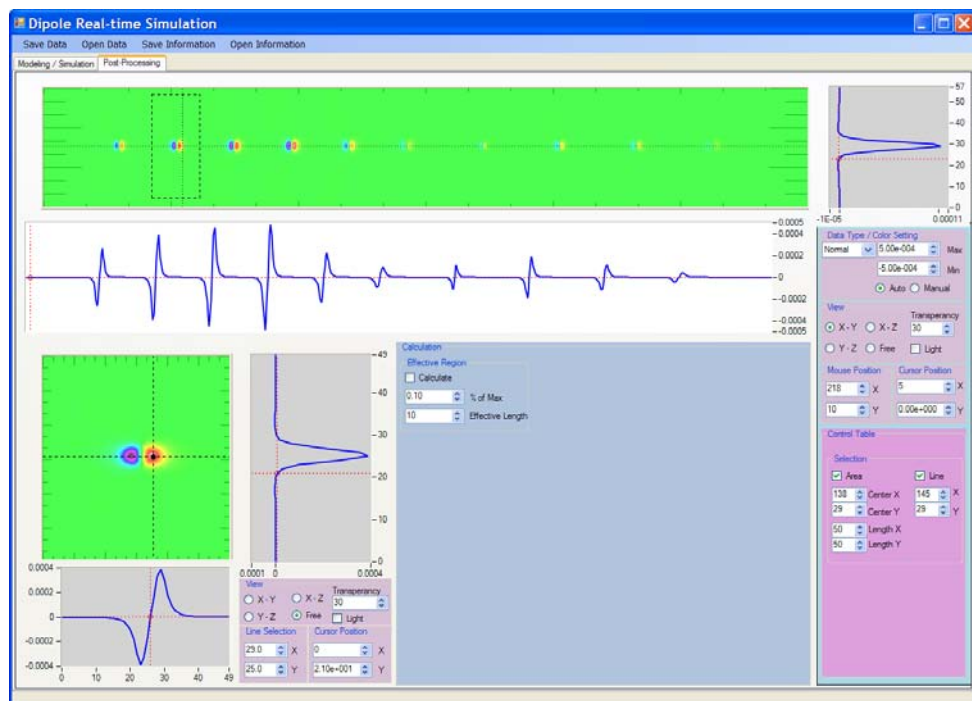
Fig. 3-34 Dipole real-time simulation software: Post-processing, normal data.

- 100 -
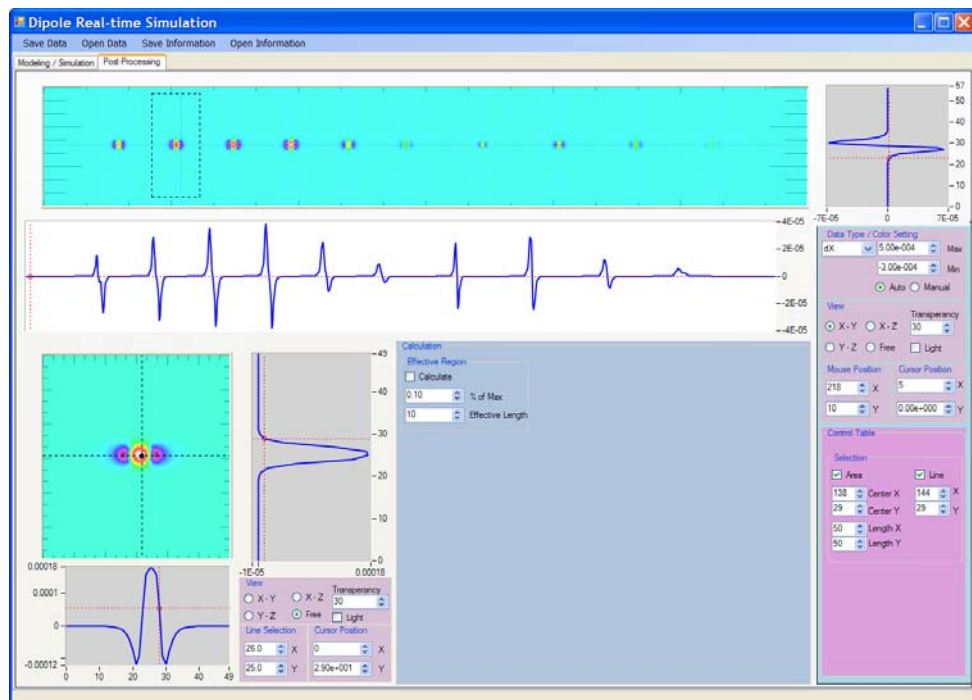
Fig. 3-35 Dipole real-time simulation software: Post-processing, ΔVx.
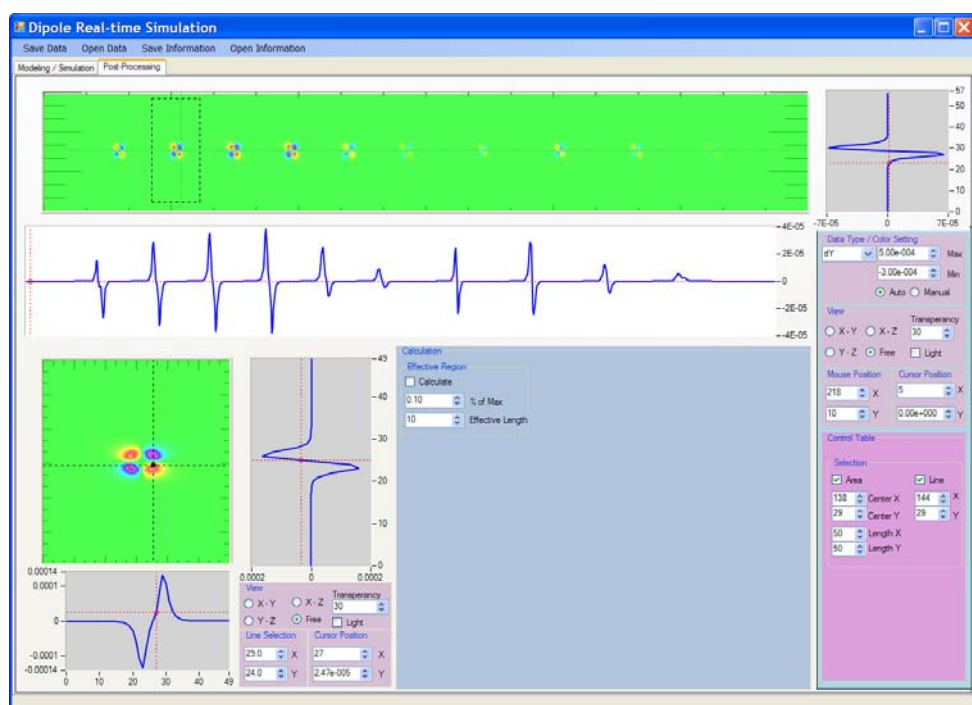
Fig. 3-36 Dipole real-time simulation software: Post-processing, ΔVy.

After finishing the simulation, we can process the simulated data in the Post-processing window, as shown in Fig. 3-34 ~ Fig. 3-36 [49]. In this mode, the three kinds of data: normal voltage and its differential in X- and Y-direction, can be selected for processing. Some convenient cursors in the image are help for easy processing and management. A section view of the main data is displayed intermediately with the changes of the cursor. A small area of data also can be viewed and enlarged in a separated image "Area view". In the area view image, we also can see the section views and others data.

CHAPTER 4 VERIFICATION OF DIPOLE MODEL

The dipole model for several shapes of crack on a flat specimen and hole-type OD and ID cracks was presented in the previous chapter. By analyzing simulation results in the both vertical (Z-component) magnetic flux density (B_{RMS}) and its differential (ΔB_{RMS}), it is found that the ΔB_{RMS} data presents information of distinguishing shape of crack. Furthermore, the ΔB_{RMS} provides non-offset value of output voltage of magnetic sensor (in this paper, we used Hall sensor) and minimizes the different of sensitivity among the sensors. Therefore, in verification of the dipole model, differential data ΔB_{RMS} will be used. To verify the performance of dipole model method, we compared dipole model method with a finite element method and experiment using magnetic cameras.

4.1. Cracks on Flat Specimen

In this section compare the dipole model results with experiment results using Area-type magnetic camera. The simulation and experiment were performed on several shapes of crack on a flat specimen which are used in Chapter 3.

4.1.1. Area-type Magnetic Camera

4.1.1.1.Principle

The principle of Area-type magnetic camera (AMC) is shown in Fig. 4-1 [32], [38]. The Hall sensor array matrix is arrayed as 1024 Hall sensors (32×32), with an effective area of 24.96×24.96 mm^2 and a spatial resolution of 0.78 mm, is placed on a STIC. The STIC consists of two coils, two cores and a copper sheet. When an alternating current is applied to the coils, a current is induced in the copper sheet. If the copper sheet is placed on a conductive specimen, an STIC will be induced in the specimen and distorted due to a crack. This STIC will induce an alternating magnetic field into the normal surface of the Hall sensor array matrix that can be measured.
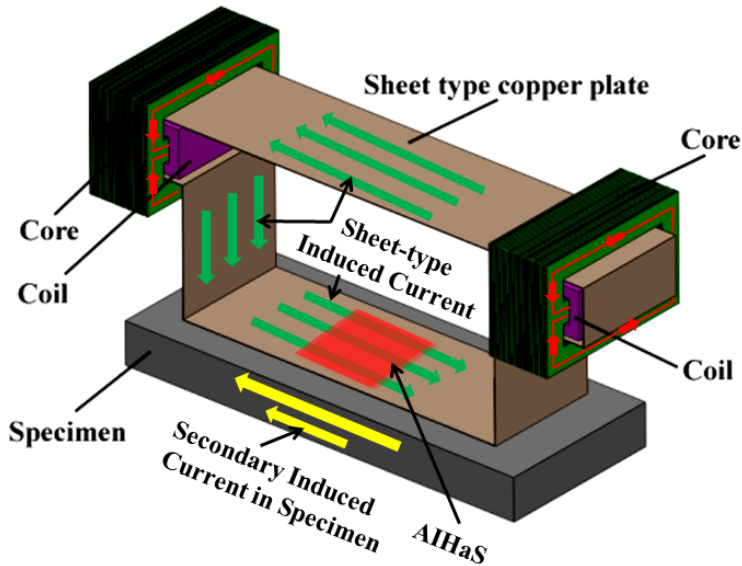
Fig. 4-1 Principle of Area-type magnetic camera

4.1.1.2. Experimental Setup

Fig. 4-2 shows the sensor array method and block diagram of Area-type magnetic camera [32], [38]. The Hall sensors were arranged on a NiZn ferrite wafer in m columns and n rows to yield a large detection area, as shown in Fig. 4-2(b). It was called Area-type integrated Hall sensors array (AIHaS). The switch input power lines (SWa_i and SWb_i, i=1, 2, 3… n) and output signal lines (V_j+ and V_j-, j=1, 2, 3…m) are connected to the input and output pins of the Hall sensors, respectively. Using this wiring method, the differential magnetic intensity can be measured with a crossed input signal row and output signal column. The AIHaS has a flexible cable and is protected by an epoxy cover. In this paper, the Hall sensors were arranged in 32 columns and 32 rows with high spatial resolution of 0.78 mm. Thus, an area of 24.18×24.18 mm^2 can be measured.

- 104 -

Collection @ chosun
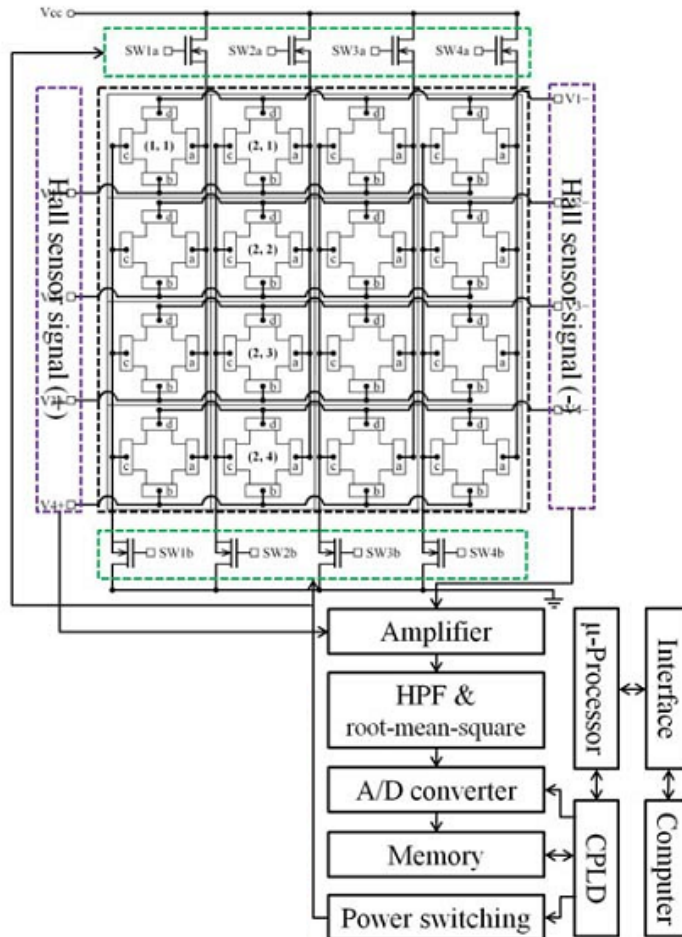
Fig. 4-2 Sensor arrangement method and block diagram of Area-type magnetic camera

The Hall sensor array matrix obtains an alternating magnetic field from the specimen and converts it to a Hall voltage (V_H) signal matrix by Eq. (4-1). The Hall voltages are gained by m amplifiers and filtered noise by m high-pass-filters (HPFs). The voltage is then converted to DC by using a root-mean-square (RMS) circuit. Thus, the phase signal is neglected and only the RMS voltage V_{RMS} (Eq. (4-2)) is used. The RMS voltage is digitized by an analog-to-digital converter (ADC, NI PCI 6071E).. In addition, the differential voltages of consecutive Hall sensors are used and displayed in the software, as expressed by Eq. (4-3).

$$V_H = K_H \cdot I_H \cdot B_Z \qquad\qquad (4\text{-}1)$$

$$V_{RMS} = G \cdot I_H \cdot B_{RMS} \qquad\qquad (4\text{-}2)$$

$$\Delta V_{RMS} = V_{RMS}(i,j) - V_{RMS}(i,j-1) \qquad\qquad (4\text{-}3)$$

where G, K_H, I_H, B_Z and B_{RMS} are the amplifier gain constant, Hall constant, Hall input current, vertical magnetic field to Hall sensor , and RMS magnetic intensity, respectively. i and j are the index of the Hall sensor element in the LIHaS and that of the data point in the scanning direction, respectively.
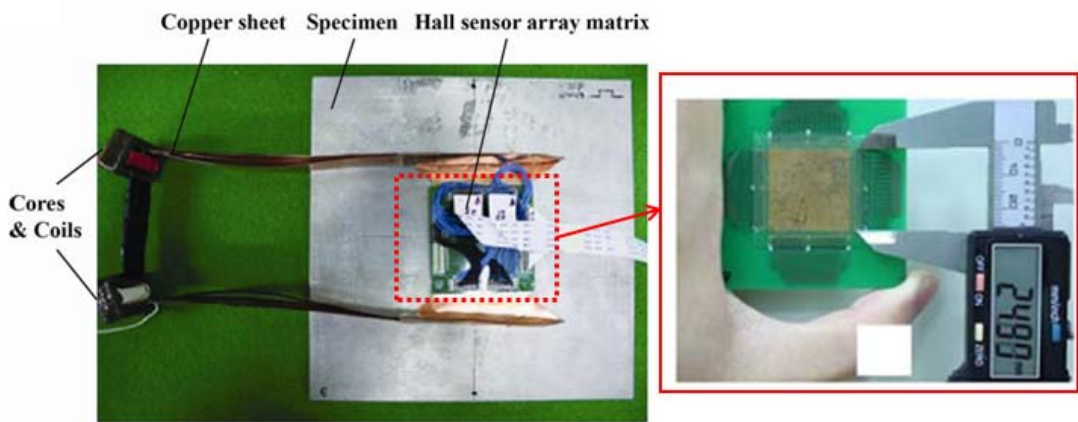
Fig. 4-3 Real picture of Area-type magnetic camera placed on an aluminum plate.

Fig. 4-3 shows a real picture of an Area-type magnetic camera on an aluminum plate [32], [38]. The 0.1 mm thick copper sheet has a 64×64 mm^2 of effective STIC area. Two $25\times40\times11$ mm^3 silicon steel cores, with two 30×5 mm^2 holes were used to induce the current in the STIC. 34 turns of coils were wound around each core center. An alternating current (2.5 A, rms) at 5, 10 and 20 kHz are applied to each coil. The Hall sensor array, with the effective area of 24.96×24.96 mm^2, was positioned on a 64×64 mm^2 printed circuit board (PCB). The Hall voltages are amplified by 72 dB. HPFs with a 1.59 kHz cut-off frequency were used to improve the signal-to-noise ratio.

Fig. 4-4 and Table 2-1 show the shape and size of the cracks with cross-section views of the rectangular, triangular, elliptical and stepped shapes used in experiment [38], [47]. The cracks were machined at the center of each specimen of aluminum alloy (Al7075)

- 106 -

using an electrical discharge machining. Crack angle in Table 2-1 is the angle between the normal of the surface of the specimen and the tangential of the crack tip. The crack angle specifies the shape of crack, which will be discussed in the later section when comparing with simulation results of the DM.
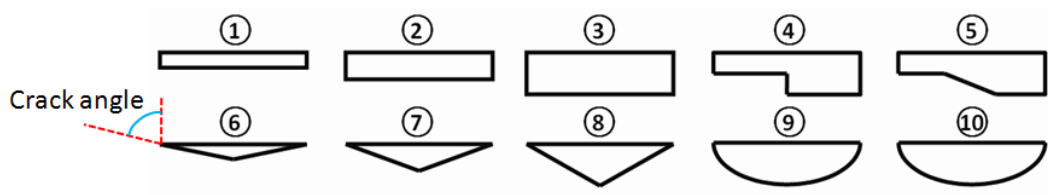
Fig. 4-4 Different cross-section of cracks used in experiment

Table 4-1 Size of each crack

Crack No.	Length [mm]	Width [mm]	Depth [mm]	Crack angle[º]	Volume [mm³]
1	10	0.7	1	90	7
2	10	0.7	2	90	14
3	10	0.7	3	90	21
4	10	0.5	1.5&3	90	11.25
5	10	0.5	1.5&3	90	11.25
6	10	0.7	1	11.3	3.5
7	10	0.7	2	21.8	7
8	10	0.7	3	30.96	10.5
9	10	0.7	3	61.9	16.49
10	10	0.9	3	61.9	21.20

4.1.1.3. Experimental results

Fig. 4-5 shows the ΔV_{RMS} (Eq. (4-3)) images and section views in the experimental results at 10 kHz [38], [46]. The frequency of 10 kHz was chosen because the crack image is the most clearly in this frequency than others frequencies, which was analysis in the FEM simulation using ANSYS software in the Chapter 2, Section 2.2.2. The experimental results show a clear magnetic image for each crack. We can distinguish the crack shapes by

observing the images in the top view. The rectangular crack appears as two colored group regions balanced at each of the two tips (Nos. 1, 2 and 3). In the images of the stepped crack, these groups are not balanced because of the different depths (Nos. 4 and 5). A large group appears at the center of the triangle crack with a smaller group at each tip of the crack (Nos. 6, 7 and 8). In the case of the elliptical crack, two groups in the middle are close and connected to each other (Nos. 9 and 10). The quantitative evaluation analysis of the experimental results will be presented in the next section when comparing DM with experiment.
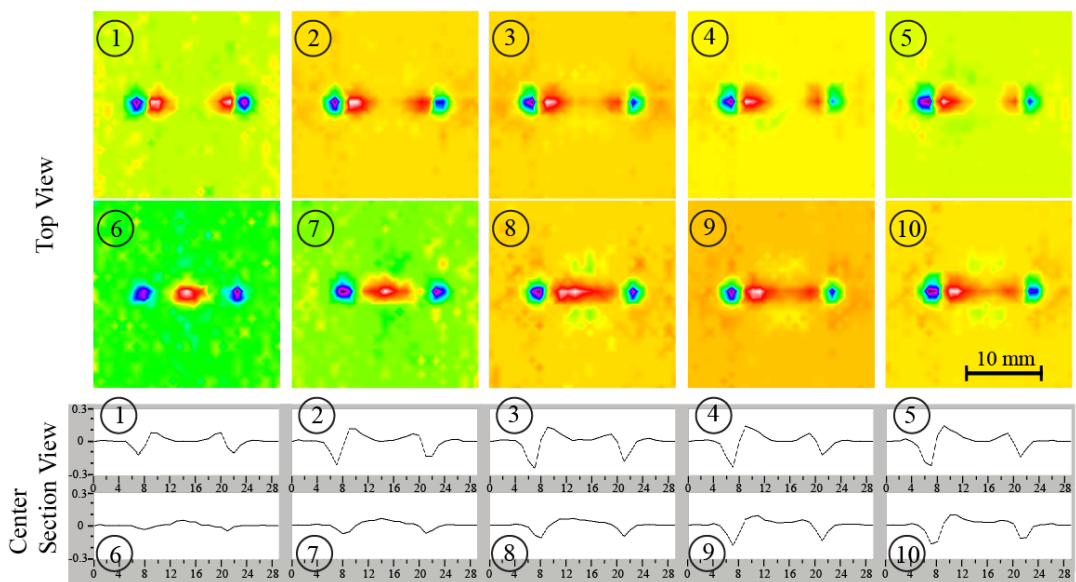
Fig. 4-5 Experimental results of Area-type magnetic camera

4.1.2. Maximum Magnetic Charge Factor

In the some samples of simulation results of dipole model method in Chapter 3, the maximum magnetic charge factor ξ_0 was assumed to be 1 Wb/m^2. This is uncertainty assumption because the ξ_0 depends on the strength of eddy current in the surface of specimen. Therefore, the maximum magnetic charge factor needs to be determined certainty. It can be observed in the calculation of magnetic field density in the Chapter 3 that ξ_0 has a linear relationship with the vertical magnetic field intensity. Thus, the ξ_0 can

- 108 -

be obtained by establishing an optimized function Q which are comparison between the summary of square of crack image in the experimental result and simulated result ($\Delta V_{RMS}|_{total}$, Eq. (3-23)) [47]. The optimized function Q includes crack images at each frequency, as expressed in Eq. (4-5). By finding the mimimum value of function Q, the ξ_0 can be obtained [46].

$$\Delta V_{RMS}|_{total} = \sum_{i=1}^{M} \sum_{j=1}^{N} [\Delta V_{RMS}(i,j)]^2 \tag{4-4}$$

$$Q = \sum_{Freqs} \sum_{Cracks} \left[\left(\Delta V_{RMS}|_{total}^{Exp}\right)^2 - \left(\Delta V_{RMS}|_{total}^{Sim}\right)^2 \right]^2$$

$$= \sum_{Freqs} \sum_{Cracks} \left[\left(\Delta V_{RMS}|_{total}^{Exp}\right)^2 - \xi_0^2 . P^2 \right]^2 \tag{4-5}$$

here, P is a function of G, K_H, I_H and summary of square of the second part (except ξ_0) in the ΔB_{RMS} data. M×N is the size of crack image. In this paper, the size 28×28 was used.

The right side of Eq. (4-5) is a four-order polynomial function respect to variable ξ_0. The function has only one constraint which is positive value of ξ_0 ($\xi_0 > 0$). There is always exists a solution for Eq. (4-5). The solution could be solve by using derivative-free method, an integrated function in Matlab software, namely '*fminsearch*.'

Ten cracks specified in Table 4-1 and the operating parameters in Table 3-2 were used in the experiment. The Area-type magnetic camera operated at 5, 10 and 20 kHz. The lift-off was about 1 mm. The detail of other parameters is indicated in Table 3-2. The resolution of the Area-type magnetic camera was simulated by meshing grid size of sensing area in the dipole model (sensing area is indicated by $\vec{r}(x,y,z)$ in Chapter 3, z is lift-off). The second part of ΔB_{RMS} is easily calculated by assuming $\xi_0 = 1$ [Wb/m^2] [46].

Fig. 4-6 shows the curve of the optimized function Q respect to the maximum magnetic charge factor ξ_0. It shows two minimum peaks of the curve because the function Q is four-order polynomial function. With the constraint of positive value, the maximum magnetic charge factor ξ_0 is found to be 0.0716 [Wb/m^2] [46].

Table 4-2 Relation between real condition and simulated parameters

Real conditions	Simulated parameters	Values in the paper
Properties of specimen	Absolute permeability (μ)	1.2566×10^{-6} H/m
	Electrical conductivity (σ)	3.5461×10^{7} S/m
Lift-off	z	1 mm
Frequency	f	5, 10, 20 kHz
Hall constant	K_H	1.5 V· $(A \cdot mT)^{-1}$
Hall input current	I_H	10 mA
Amplifier	G	$10^{3.6}$ (72 dB)
Spatial resolution of the Hall sensor matrix	Meshing size of the software	0.78 mm
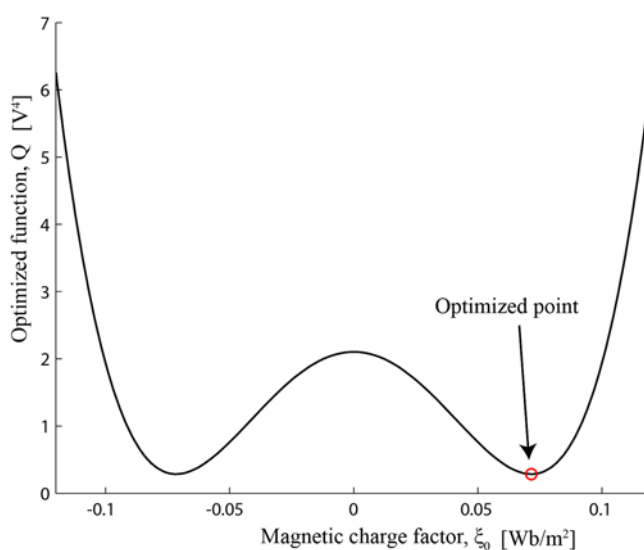
Fig. 4-6 Finding optimized magnetic charge factor by finding minimum of optimized function Q.

4.1.3. Qualitative Comparison

Fig. 4-7 and Fig. 4-8 show the ΔV_{RMS} images and section views in the experimental and simulated results at 10 kHz, respectively [46]. The images of the cracks are clear and show good agreement between the simulated and experimental results. The group colored regions in Fig. 4-7 and the peak values in Fig. 4-8 appear at the two tips of the cracks because the high eddy current concentration there.
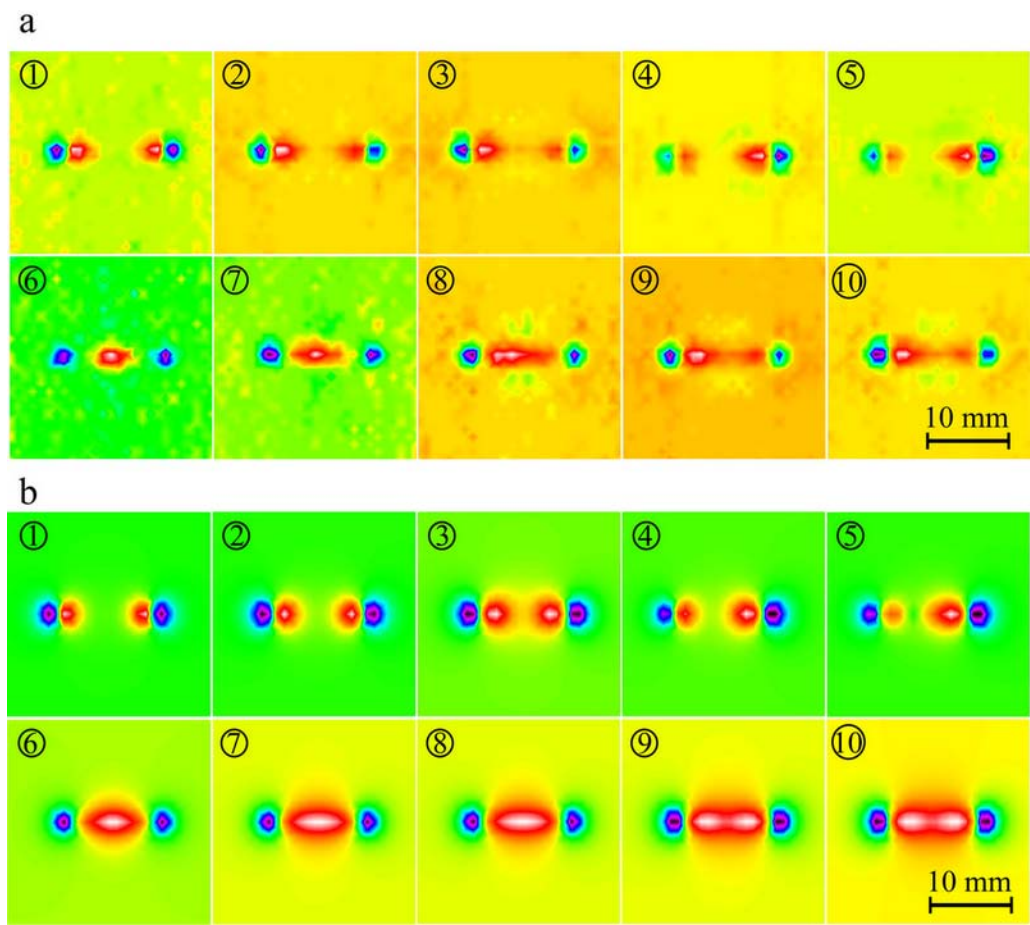
Fig. 4-7 (a) Experimental and (b) simulated results at 10 kHz

Observing the images in Fig. 4-7, we can distinguish the crack shapes. The rectangular crack appears as two colored group regions balanced at each of the two tips

- 111 -

(Nos. 1, 2 and 3). In the images of the stepped crack, these groups are not balanced because of the different depths depths (Nos. 4 and 5). A large group appears at the center of the triangle crack with a smaller group at each tip of the crack (Nos. 6, 7 and 8). In the case of the elliptical crack, two groups in the middle are close and connected to each other (Nos. 9 and 10).

Furthermore, both the size of the middle colored group in Fig. 4-7 and the peak values in Fig. 4-8 differ according to the crack size. In the case of the rectangular (Nos. 1, 2 and 3) and triangular (Nos. 6, 7 and 8) cracks, they increase with the crack depth. In the case of the elliptical cracks (Nos. 9 and 10), they increase with the crack width.
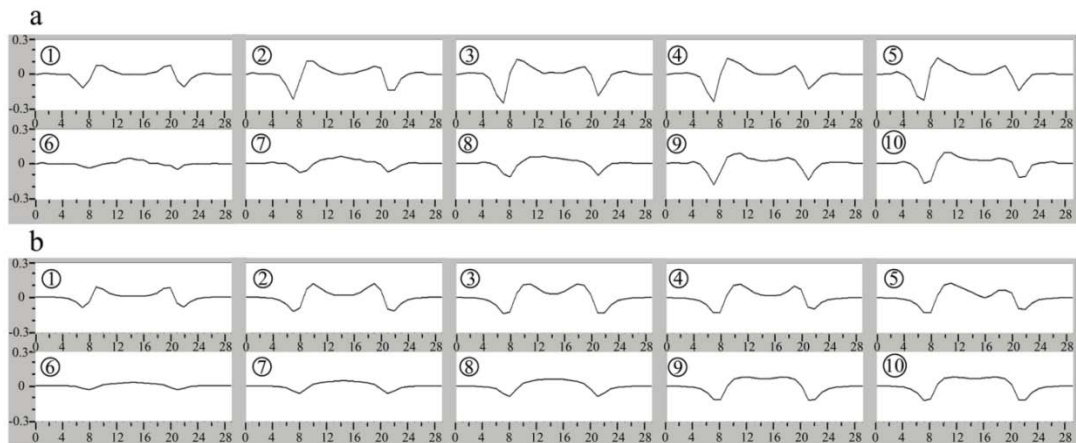
Fig. 4-8 Section view of ΔV_{RMS} images located on the center line of each crack in the experimental (a) and simulated (b) results

4.1.4. Quantitative Comparison

Fig. 4-9(a) and (b) show the relation of the peak-to-peak distance L_p with the crack-angle which is the angle between the specimen surface and the tip-side along the crack depth direction. The L_p value (length) in both the experimental and simulated results ranges from 10.4 mm to 12.3 mm and increases with the crack-angle. In addition, the coefficient angles of the interpolate lines are similar. However, in the experimental result, the coefficient angle exhibits greater variation with respect to frequency than in the

Collection @ chosun

simulated result. By using L_p, we can estimate the crack-angle and subsequently the crack shape.
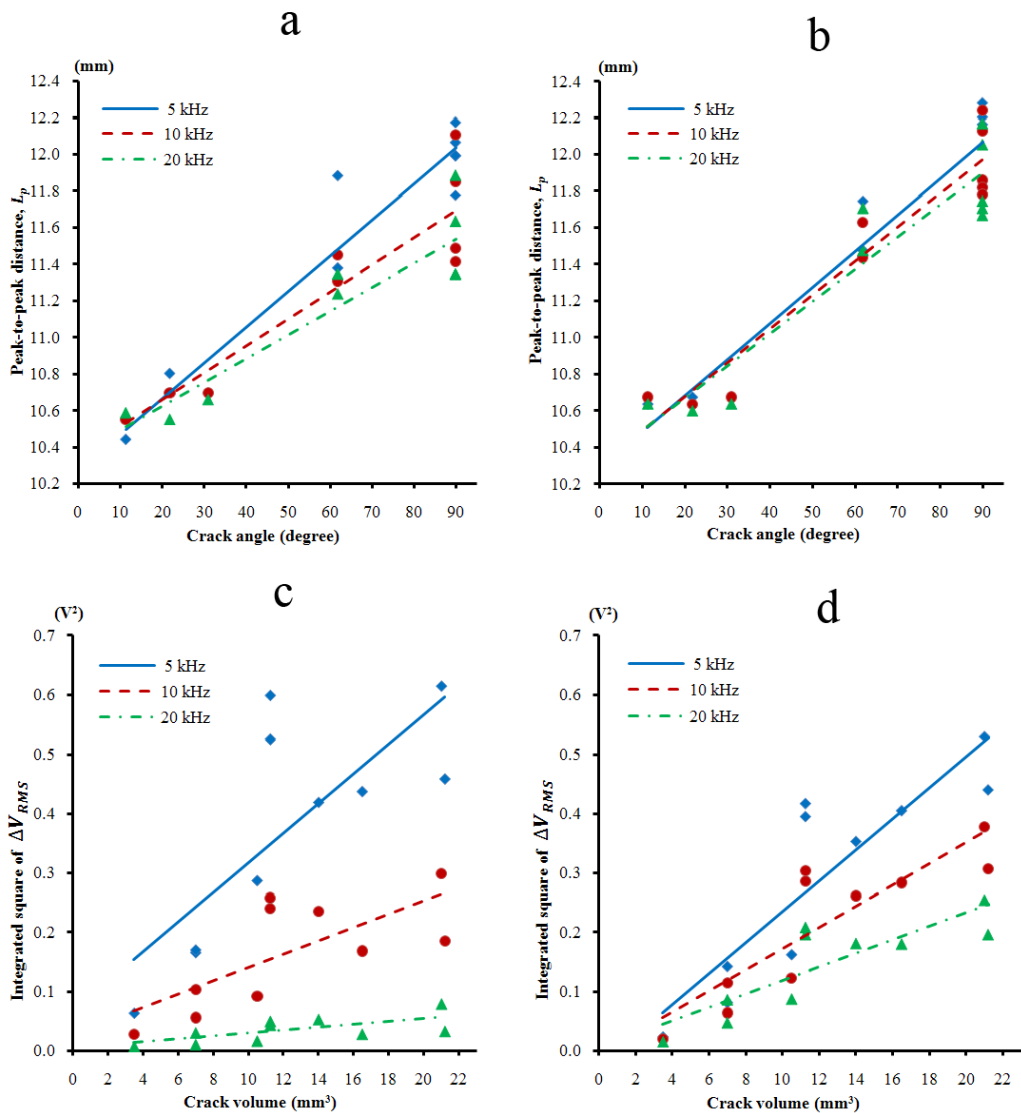
Fig. 4-9 Relation of the peak-to-peak distance (L_p) with the crack-angle, and summary square values of ΔV_{RMS} with the crack volume in the experimental (a), (c) and simulated (b), (d) results.

Fig. 4-9(c) and (d) show the relation of the crack volume with the summary of square of ΔV_{RMS} obtained by in the experimental and simulated results [46]. This value is

proportional to the crack volume. However, in the experimental result, it exhibits greater variation with respect to frequency than in the simulation result. Therefore, the crack volume can be estimated by using this summary square value.

Because of the skin effect, the current density decreases more rapidly when the frequency is higher. Consequently, the effect of the crack depth is less pronounced at higher frequency. Therefore, the L_p value and the summary square of ΔV_{RMS} are lower at higher frequencies, as shown in Fig. 4-9. In addition, all the crack shapes described in this paper are highly dependent on the crack depths. At high frequency, a shallow part of a crack (in the depth direction) has a large effect that is equivalent to the effect of a shallow crack depth. Thus, the crack shape has a small effect at high frequency, indicating that the difference in the measured data between cracks is smaller. Therefore, the data in both the experimental and simulated results in Fig. 4-9(c) and (d) fit better at a higher operating frequency.

4.2. Cracks on Pipe Specimen

In this section, I compare the dipole model results with finite element method and experiment results using Cylinder-type magnetic camera. The simulation and experiment were performed on hole-type OD and ID cracks on a small-bore titanium pipe. The titanium specimen and cylinder sensor were same with these using in Chapter 2 and 3. Some more cracks are added in this chapter.

4.2.1. Cylinder-type Magnetic Camera

Small-bore piping systems are widely used in heat exchangers in nuclear power plants (NPPs), petrochemical plants, petroleum refineries, and natural-gas processing plants. A steam generator (SG) is used to feed the heat exchanger through pipes which are prone to cracking due to the extremely harsh operational conditions in a NPP. SGs transfer heat from the reactor cooling system to the secondary side of the tubes, which contain feed water [107]. They operate under extremely harsh conditions including high water pressure, high temperature, and radioactivity. These conditions cause the initiation and rapid

Collection @ chosun

propagation of cracks. Certain types of cracks typically appear in SGs such as flaw-accelerated corrosion, inter-granular attacks, axial or circumferential outside-diameter (OD) stress corrosion cracking (SCC), and primary water SCC [107], [108]. These cracks degrade the properties of the SG material and threaten the NPPs. Therefore, rapid and accurate inspection of cracks in SGs is important to protect NPPs and reduce costs.

SGs are normally manufactured using austenitic nickel-chromium-based super alloys and non-ferromagnetic titanium alloys. Eddy current testing (ECT) is highly effective and suitable for the inspection and evaluation of cracks [109]-[111]. In each NPP, 2–4 sets of SGs are used. Each set has 3,000 –16,000 SGs, and each SG is about 20 mm in diameter and 21 m in height [108]. An ECT probe needs to be inserted inside these small, long tubes to investigate cracks. Bobbin probes have been used as an ECT probe standard for general inspection of SGs for many years [108], [112]-[114]. They are reliable and can be used to quantify volumetric flaws such as fretting wear and pitting corrosion. However, these probes are only sensitive to axial cracks because they obtain integrated data over the entire diameter of the SG; they are unsuitable for detecting circumferential cracks [108], [112]-[114]. The motorized rotating pancake coil (MRPC) was developed to inspect both axial and circumferential cracks, and record data at each scanning point. However, an MPRC requires a complex installation procedure and it is about 80–120 times slower than a bobbin probe [108], [113]. X-probes that combine coils aligned for axial and circumferential cracks have been developed such that rotation of the coils is not required [108], [114]-[117]. However, the number of coils is limited to 4–19 coils, depending on the SG diameter, which limits the spatial resolution of the sensor. To overcome these limitations, a cylinder-type magnetic camera (CMC) have been developed, which has numerous magnetic sensors arrayed in a matrix with a high spatial resolution and high imaging speed [37], [44]. For example, a CMC has 0.78 mm of spatial resolution, a 32×32 array of InSb Hall sensors, and an imaging speed of 1 frame/s [37]. A CMC can inspect both axial and circumferential cracks on small-bore pipe and estimate crack volumes.

4.2.1.1. Principle and Components

Fig. 4-10 shows the block diagram of a CMC inserted in a small-bore pipe with a crack [37], [44], [122]. The sensor probe consists of a bobbin coil wound around an m×n matrix of solid-state Hall sensor arrays. The bobbin coil, which is the magnetic source of the CMC, induces an eddy current in the circumferential direction in the pipe. The presence of the crack obstructs the eddy current flow, inducing a secondary alternating magnetic field. The Hall sensors measure the radial component of the secondary alternating magnetic field that is perpendicular to the sensor's surface, which is expressed by Eq. (4-6). The output voltages from m channel signal with (m Hall sensors) are transferred to the m amplifiers, after which the noises are filtered using m high-pass filters (HPFs). Next, the signals are converted to a DC signal via m root-mean-square (RMS) circuits, and then transferred to the computer through an ADC converter and interface. Correspondingly, the output signals are expressed by Eq. (4-7). The power switching circuit contributes the power for n channel power (i.e., a line sensor) to operate all the matrix sensors.
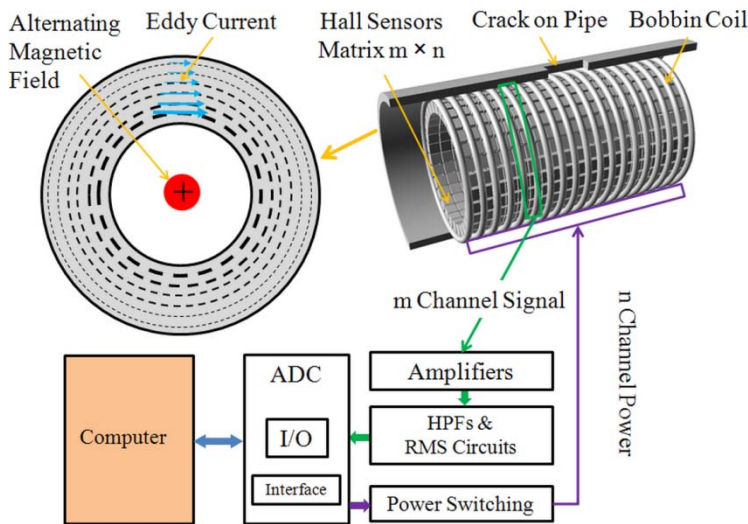
Fig. 4-10 Block diagram of a Cylinder-type magnetic camera

$$V_H(t) = K \cdot I \cdot B_r(t) = K \cdot I \cdot B_{r0} \cdot \sin(2\pi f \cdot t + \varphi) \tag{4-6}$$

$$V_{RMS} = \sqrt{\frac{1}{T}\int_0^T [V_H(t)]^2 dt} = K \cdot I \cdot B_{r0}\sqrt{\frac{1}{T}\int_0^T \sin^2(2\pi f \cdot t + \varphi)dt} \qquad (4\text{-}7)$$

$$= \frac{K \cdot I \cdot B_{r0}}{\sqrt{2}}$$

$$\Delta V_{RMS} = V_{RMS}(i,j) - V_{RMS}(i,j-1) \qquad (4\text{-}8)$$

where f, μ, and σ are the excited frequency, absolute permeability, and electrical conductivity, respectively, of the specimen; K, I, t, B_{r0}, T, and φ are the Hall constant, input current of the Hall sensor, and the time, amplitude, period and phase of the radial component of alternating magnetic field, $B_r(t)$, respectively, which is perpendicular to the Hall sensor surface. i and j are index of Hall sensor in the circumferential direction and index of data point in the scan direction. ΔV_{RMS} is the differential of V_{RMS} in the scan direction.

4.2.1.2. Experiment Setup

The setup of the CMC system with a Linear guide motor (LGM) is shown in Fig. 4-11 [122]. The CMC was made of array 32×32 Hall sensors in a matrix on a cylinder shape with a diameter of 14.9 mm and spatial resolution of 0.78 mm [37], [44], [122]. Thus, the sensing area is 24.96 mm × 202°. The matrix Hall sensors is called Cylinder-type integrated Hall sensors array (CIHaS). The number of amplifiers, HPFs, and RMS circuits are same with number of channel signal that is 32. The gain of amplifiers is 60 dB and cut-off frequency of HPFs is 300 Hz. The commercial ADC (NI PCI 6071E) with 1.25 MS/s, ±10 V measurement range, and 12 bits corresponding to 4.88 mV resolution was used. A 0.25 mm diameter coil was wound around the CMC sensor with 120 turns in 30 mm length to make a bobbin coil.

The small-bore titanium alloy pipe specimen was manufactured accordance with the ASME SB338 GR2 standard. The titanium pipe has an inner diameter, outer diameter, and thickness of 17.28 mm, 19 mm, and 0.86 mm, respectively (Fig. 4-12). The titanium pipe has 5 artificial OD cracks and one OD circumferential crack. The detailed sizes and types of the copper pipe and titanium pipe are listed in Table 4-3. The volumes of the

cracks were calculated using a 3D design tool (Solidworks 2009). The volume of each crack is different and the value was calculated using the diameter and the depth of the crack. Cracks No. 5 in has four OD cracks positioned equally around the pipe. However, only three cracks were inspection targets because of the detectable angle (202°) of the sensor.
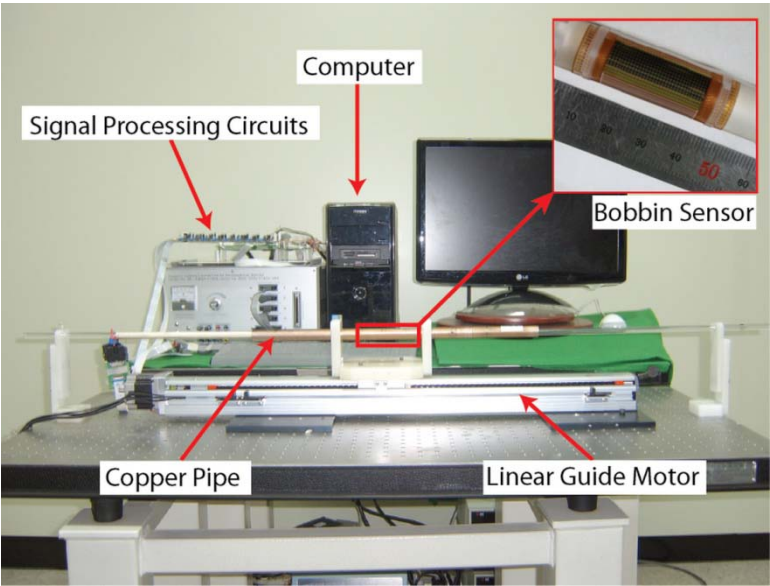
Fig. 4-11 Setup of the CMC system with two scanning modes using an LGM.
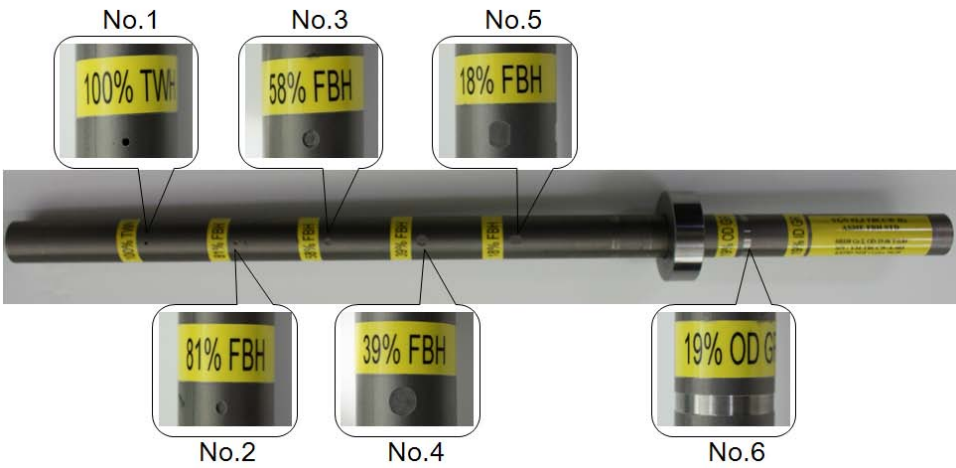
Fig. 4-12 Picture of cracks on a titanium alloy pipe

Table 4-3 Shape and size of cracks in titanium alloy pipes

No.	Shape	Depth [mm]	Diameter [mm]	Volume [mm3]
1	Through (ID)	0.860	1.0	0.68
2	OD	0.697	1.8	1.77
3	OD	0.499	2.7	2.86
4	OD	0.335	4.6	5.57
5	OD × 4	0.155	4.6	2.57
6	Circumferential (OD)	0.163	3.0 (width)	17.09

4.2.1.3. Experimental results
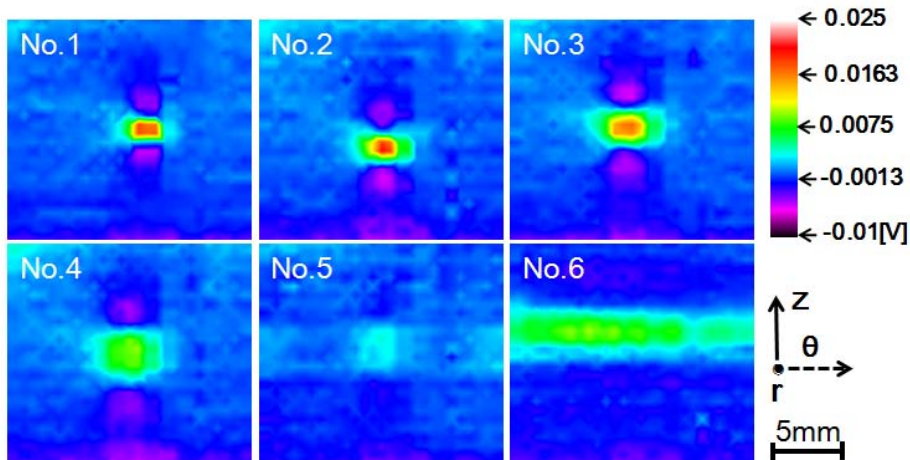
Fig. 4-13 Experiment results for titanium alloy pipe

Fig. 4-13 shows the experiment results for the titanium alloy pipe in ΔV_{RMS} (Eq. (4-8)) images obtained by the CMC in the ASM [37]. An alternating current of 0.6 A amplitude and 5 kHz was supplied to the bobbin coil. The imaging speed was same in the experiment of the copper alloy pipe, which is 1 fps. The electrical conductivity of titanium alloy is 1.92×10^6 S/m much smaller than electrical conductivity of copper alloy (59.6×10^6 S/m). However, by increasing the input current to the bobbin coil, all the cracks were still clearly imaged. The No. 5 has 4 OD cracks equally distributed around the pipe; however, only 3 cracks were inspected due to measuring region of CIHaS was 202°. In the results,

- 119 -

we displayed only one crack image of No. 5. The OD circumferential crack No. 6 was also inspected.

4.2.2. Maximum Magnetic Charge Factor

Table 4-4 lists the crack shapes and sizes used in the comparison [45]. The cracks in the Chapter 2 and 3 are used in this chapter. Some more cracks are added in the dipole model because they are easy to be simulated. Three types of crack are used in this section; they are hole-type through, OD, and COD cracks. Totally, 17 cracks are used. The depth of cracks ranges from 37% to 100% of the titanium pipe thickness. The diameter of cracks ranges from 1 mm to 4.6 mm. There is only one COD crack which is used to compare the dipole model with experiment.

Table 4-4 Shape and size of cracks on a pipeline

No.	Shape	Depth [% - mm]	Diameter [mm]	Volume [mm³]	Experiment	FEM	DM
1	Through	100% - 0.86	1.0	0.675	✓		✓
2	OD	37% - 0.315	1.5	0.543		✓	✓
3	Through	100% - 0.86	1.5	1.521		✓	✓
4	OD	58% - 0.499	1.8	1.242		✓	✓
5	OD	81% - 0.697	1.8	1.746	✓	✓	✓
6	OD	37% - 0.315	2.7	1.666		✓	✓
7	OD	58% - 0.499	2.7	2.719	✓	✓	✓
8	OD	81% - 0.697	2.7	3.852		✓	✓
9	Through	100% - 0.86	2.7	4.936		✓	✓
10	COD	18% - 0.155	4.6	2.575	✓		✓
11	OD	37% - 0.315	4.6	4.067		✓	✓
12	OD	39% - 0.335	4.6	4.310	✓	✓	✓
13	OD	58% - 0.499	4.6	8.285		✓	✓
14	OD	81% - 0.697	4.6	10.415		✓	✓
15	Through	100% - 0.86	4.6	14.409		✓	✓
16	Through	100% - 0.86	4.2	11.909		✓	✓
17	Through	100% - 0.86	4.0	10.802		✓	✓
18	Circum-ferential	19% - 0.163	3.0 width	7.628	✓	✓	
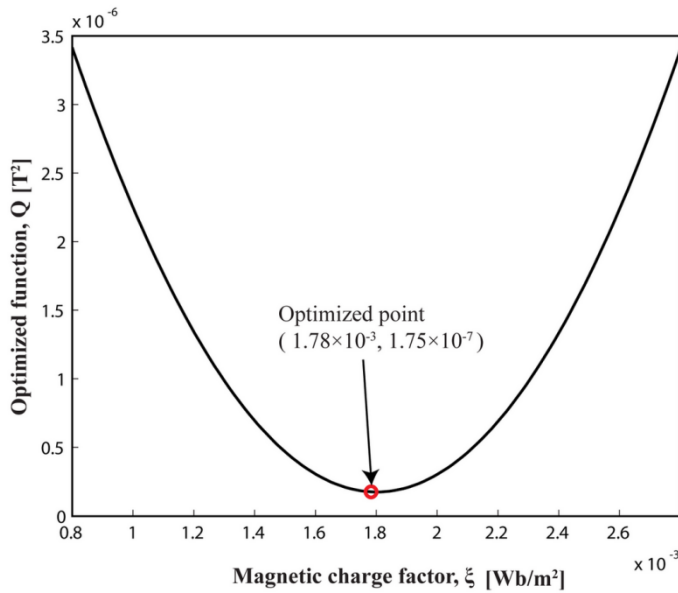
Fig. 4-14 Optimized magnetic charge factor obtained by determining the minimum optimized function.

A square optimized function (or cost function) Q in Eq. (4-11) is established [45]. The function Q is the difference between the total absolute data of the same selected area around a crack in the FEM and DM simulations. It is the second-order polynomial respect to the variant ξ. A small value of Q shows a good agreement between the DM and FEM. We can determine the magnetic charge factor (ξ) by finding the minimum value of Q. The relationship between the optimized function Q and the magnetic charge ξ is shown in Fig. 8. Next, we obtained the optimized magnetic charge factor $\xi = 1.78 \times 10^{-3}$ [Wb/m^2] and an offset value $\gamma = 1.75 \times 10^{-7}$ [T^2] [45].

$$\Delta B|_{total} = \sum_{i=0}^{M} \sum_{j=0}^{N} |\Delta B_r(i,j)| \tag{4-9}$$

$$Q = \sum_{Cracks} [\Delta B|_{total}^{FEM} - \Delta B|_{total}^{DMM} - \gamma]^2 \tag{4-10}$$

$$= \sum_{Cracks} [\Delta B|_{total}^{FEM} - \xi P - \gamma]^2 \tag{4-11}$$

- 121 -

where $P = \Delta B|_{total}^{DMM}$ with $\xi = 1$, and γ is the constant offset value which relates to the accumulated errors and biased magnetic field in the FEM simulation.

4.2.3. Qualitative Comparison

Fig. 4-15 shows simulated results for the (a) FEM and (b) DM [45]; details of the shapes and sizes of the cracks are listed in Table 4-4. A total of 12 cracks of through-hole and normal-hole types were provided in here with the changes of depth and diameter. The cracks in each column have the same depth but different diameters, and the cracks in each row have the same diameter but different depths. The image of a crack is the distribution of the differential magnetic field (ΔB_r) around that crack, which has 2 fairly symmetric groups and an oval-shape in the center. The results show good agreement between the 2 simulation methods. The distribution area of ΔB_r increases with an increase in crack diameter, as seen by glancing over the figure from left to right. When glancing over the figure from bottom to top, the value of ΔB_r is seen to increase with an increase in crack depth. In addition, the image intensity of each crack shows good agreement in the both methods. In the FEM simulation, the images of the results were not as clear as those in the DM simulation. This is due to the accumulated errors in the FEM simulation, which implies that the DM has superior performance as compared to the FEM. Furthermore, upon comparing the computation times of these methods, the DM was found to be much faster than the FEM. For example, the FEM simulated the cracks 2 and 15 using 381,021 and 484,713 elements, and required 13 m 55 s and 21 m 24 s, respectively. Conversely, the DM required only 3 s and 1 s for each crack, respectively, when using same computer: Intel Xeon (CPU E5410, Speed 2.33 GHz, 8 GB RAM) with Win XP x64, SP2.
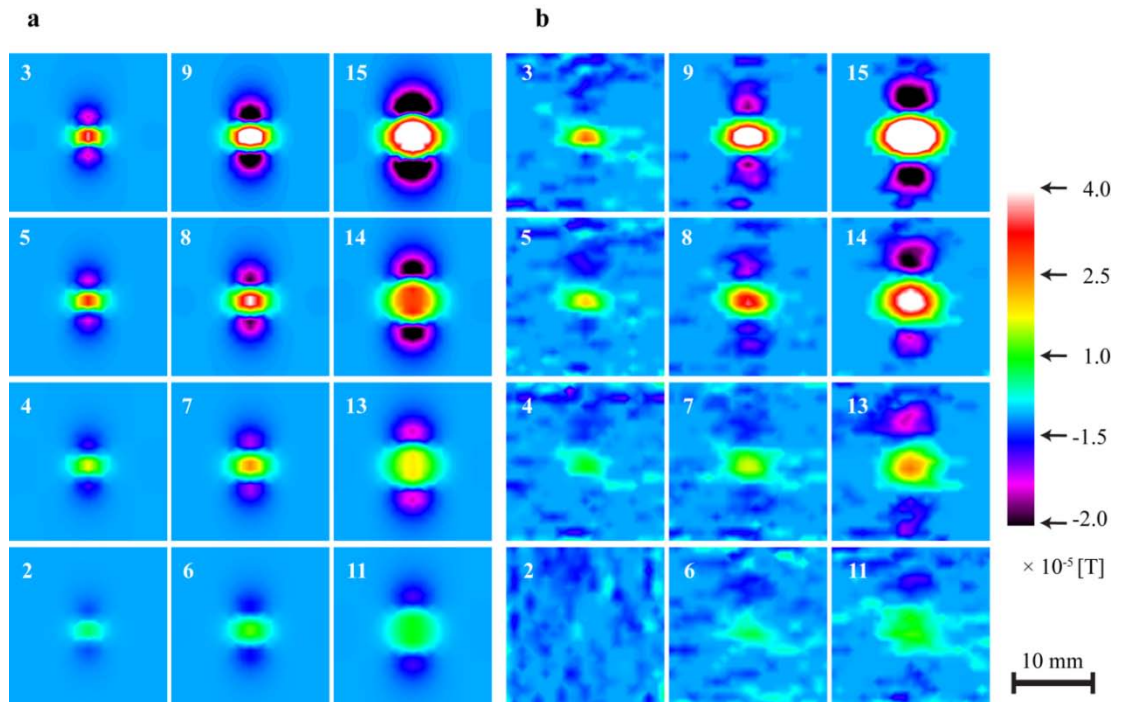
Fig. 4-15 Simulated results of the dipole model method (a) and the finite element method (b).

Some simulated results were extracted from the FEM and DM to compare their performance with those obtained using an actual inspection system (CMC), as shown in Fig. 4-16 [45]. The cracks also increased in diameter and depth (in the left and right columns of each figure, respectively), as indicated in Table 4-4. There was good agreement among the three methods. When the depths and diameters increased, the crack images increased. Clear images could be obtained using the CMC, and this indicates that smaller cracks can be inspected using the CMC. Not only do hole-type cracks obstruct the eddy current flow, but circumferential cracks that are aligned parallel to the eddy current flow can be detected using the CMC (Fig. 4-16). Similar results were obtained by the FEM, but, the DM was limited to simulate circumferential cracks.
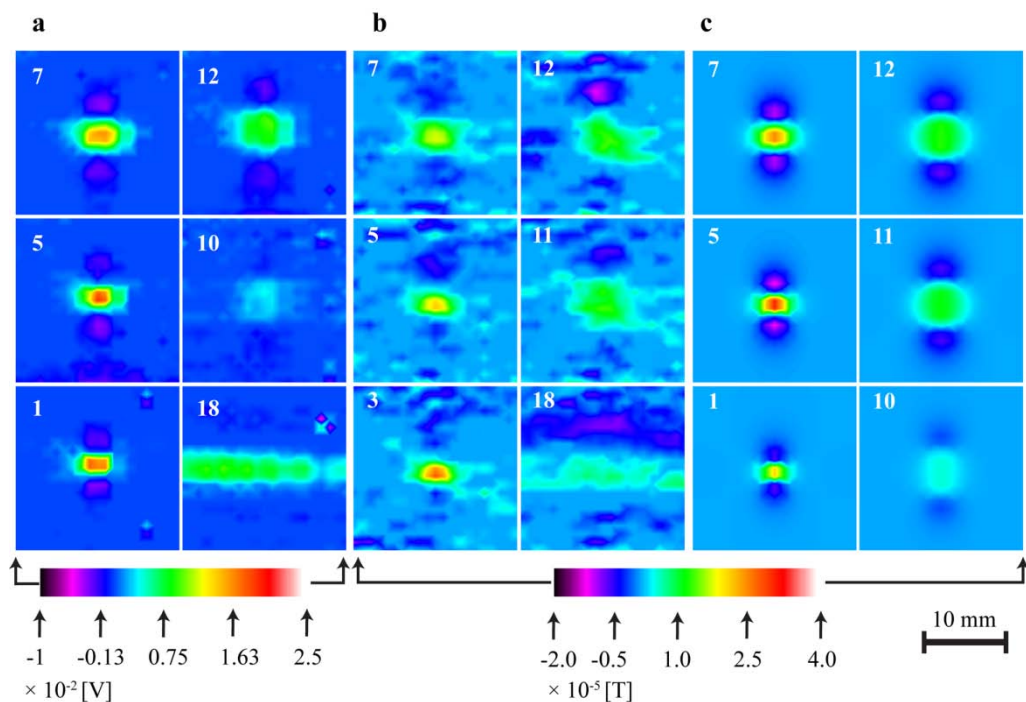
Fig. 4-16 (a) Experimental results, and simulated results of (b) the finite element method, and (c) the dipole model method

4.2.4. Quantitative Comparison

To estimate the volume of the cracks, the integrated absolute data ($\Delta B_r|_{total}$ in Eq. (9) for the FEM and DM and $\Delta V|_{total}$ in Eq. (4-12) for the BMC) were used [45]. The same area around a crack image was selected to perform this operation; herein, we selected $M \times N = 20 \times 20$. The relationship between the integrated absolute data and crack volume (Vol) was found to be a linear relation, as indicated by Eq. (4-13) for the CMC, Eq. (4-14) for the FEM, and Eq. (4-15) for the DM [45]. Thus, the crack volume could be estimated as shown in Fig. 4-17. The standard deviations in the results of the experiment, FEM, and DM were 1.148, 1.513, and 1.485, respectively. The data from the 3 methods were found to have a very good correlation. In particular, the results of the FEM and DM had extremely good correlation which validates the DM.
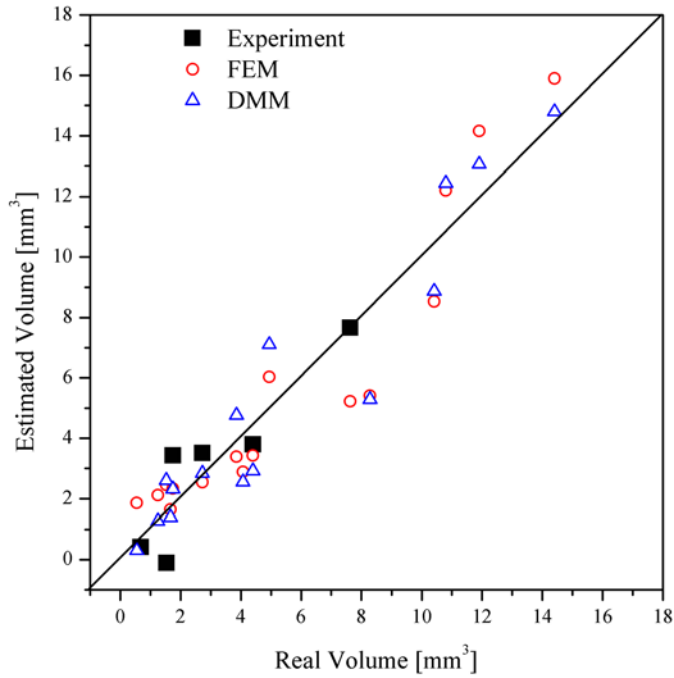
Fig. 4-17 Estimated crack volume using the integrated absolute data.

$$\Delta V|_{total} = \sum_{i=0}^{M} \sum_{j=0}^{N} |\Delta V(i,j)| \qquad (4\text{-}12)$$

$$\Delta V|_{total} = 0.342 Vol + 0.181 \qquad [\text{V-mm}^3] \qquad (4\text{-}13)$$

$$\Delta B|_{total}^{FEM} = 14.82 \times 10^{-5} Vol + 4.35 \times 10^{-5} \qquad [\text{T-mm}^3] \qquad (4\text{-}14)$$

$$\Delta B|_{total}^{DM} = 14.61 \times 10^{-5} Vol + 5.21 \times 10^{-5} \qquad [\text{T-mm}^3] \qquad (4\text{-}15)$$

4.3. Simulation of Scanning Bobbin-type Magnetic Camera

For easy understanding the ECT systems used in the small-bore piping system, the simulation of the scanning state of the sensor probe is necessary to be performed. The simulation help the user understand the changes of signal during operation of the ECT equipments. The previous FEM methods [55], [57], [58] generally require meshing each component within each position of the coil probe which can lead to inefficient computation owing to time consumption and to large computational errors from limitations in the meshing size. To solve these problems, Zheng et al. [127], [128] have developed an extended iteration finite element model in which the coil probe is not necessarily meshed; however, their method is still based on the FEM, which is time-consuming and complicated to implement.

In this section, I present a method of simulating the alternating magnetic field around cracks in a pipeline system that arises when a bobbin coil is inserted into the pipeline. Based on the movement of the bobbin coil, the distribution of the magnetic field can be simulated and observed at high speed by using the DM. The DM provides easy implementation and fast simulation that can simulate the scanning state of the bobbin coil. To validate the effectiveness of this method, we performed experiments using a BMC that can inspect cracks in a small-bore piping system.

4.3.1. Bobbin-type Magnetic Camera

4.3.1.1. Experimental Setup

The CMC was designed to operate in two modes: line scan mode (LSM) and area scan mode (ASM). In the LSM, a circumferential arrayed sensor (usually in the center) is selected, so called "bobbin-type magnetic camera" (BMC), and it scans the entire pipe. Therefore, the radial magnetic field distribution of the disturbed eddy current in the pipe can be continuously captured. The circumferential arrayed sensor is called Bobbin-type integrated Hall sensors array (BIHaS). A BMC could simply include only one circumferential arrayed sensor s which is in the next generation of magnetic camera.

There are two small pipe specimens were used in the experiment. One was copper alloy (Cu 90%, Ni 10%), and another was titanium alloy. The small-bore copper alloy pipe was a standard specimen (ASME/ID PIT CAL. STD for YG12), which has inner diameter, outer diameter, and thickness of 16.56 mm, 19.1 mm, and 1.27 mm, respectively (Fig. 4-18). The copper pipe has total of 10 artificial hole-type cracks and 2 circumferential cracks as simulations of inner diameter (ID), outer diameter (OD) and circumferential corrosions. The through hole-type cracks were classified as the ID type. Cracks No. 10 in copper pipe has four OD cracks positioned equally around the pipe; however, only 3 cracks were inspected due to measuring region of the CIHaS was 202°.
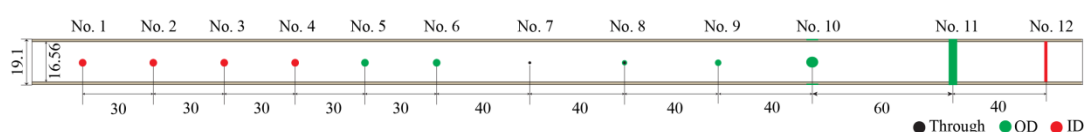
Fig. 4-18 Cracks on a copper alloy pipe

Table 4-5 Shape and size of cracks in copper alloy and titanium alloy pipes

Specimens	No.	Shape	Depth [mm]	Diameter [mm]	Volume [mm3]
Copper alloy	1	ID	0.30	3.0	2.36
	2	ID	0.60	3.0	4.48
	3	ID	0.90	3.0	6.60
	4	Through (ID)	1.27	3.0	9.01
	5	OD	1.01	3.0	6.93
	6	OD	0.65	3.0	4.38
	7	Through(ID)	1.27	1.0	1.00
	8	OD-Through (ID)	1/0.27	2.0/1.0	3.32
	9	OD	0.81	2.5	3.87
	10	OD ×4	0.38	4.5	4.98
	11	Circumferential (OD)	0.22	3.0 (width)	17.72
	12	Circumferential (ID)	0.22	1.0 (width)	4.58

- 127 -

4.3.1.2. Experimental Results

Fig. 4-19 shows the experiment results for the copper alloy pipe in ΔV_{RMS} (Eq. (4-8)) images obtained by the CMC in the both two modes [44]. An alternating current of 0.45 A amplitude and 5 kHz was supplied to the bobbin coil. The speed of power switching in the ASM was 30 ms. Hence, the frame speed of the CMC was 1 fps. The center circumferential arrayed sensor was selected for the BMC (LSM). The BMC was operated at about 5 mm/s and 0.5 mm of scan step. It's observed that the results of the CMC and the BMC have good agreements.

In addition, OD as well as ID cracks were clearly detected. As shown in No. 10, 3 OD cracks were detected. Although there are 4 OD cracks, only 3 cracks were detected because the measuring region was 202° as mentioned in the previous section. Furthermore, circumferential OD and ID cracks were detected, as shown in No. 11 and No. 12, respectively. Here, we note that when a circumferential crack is oriented along the same direction as that of the current induced by the bobbin coil, the delectability of cracks is minimized. Nonetheless, the circumferential IDSCC and ODSCC could be detected and displayed.
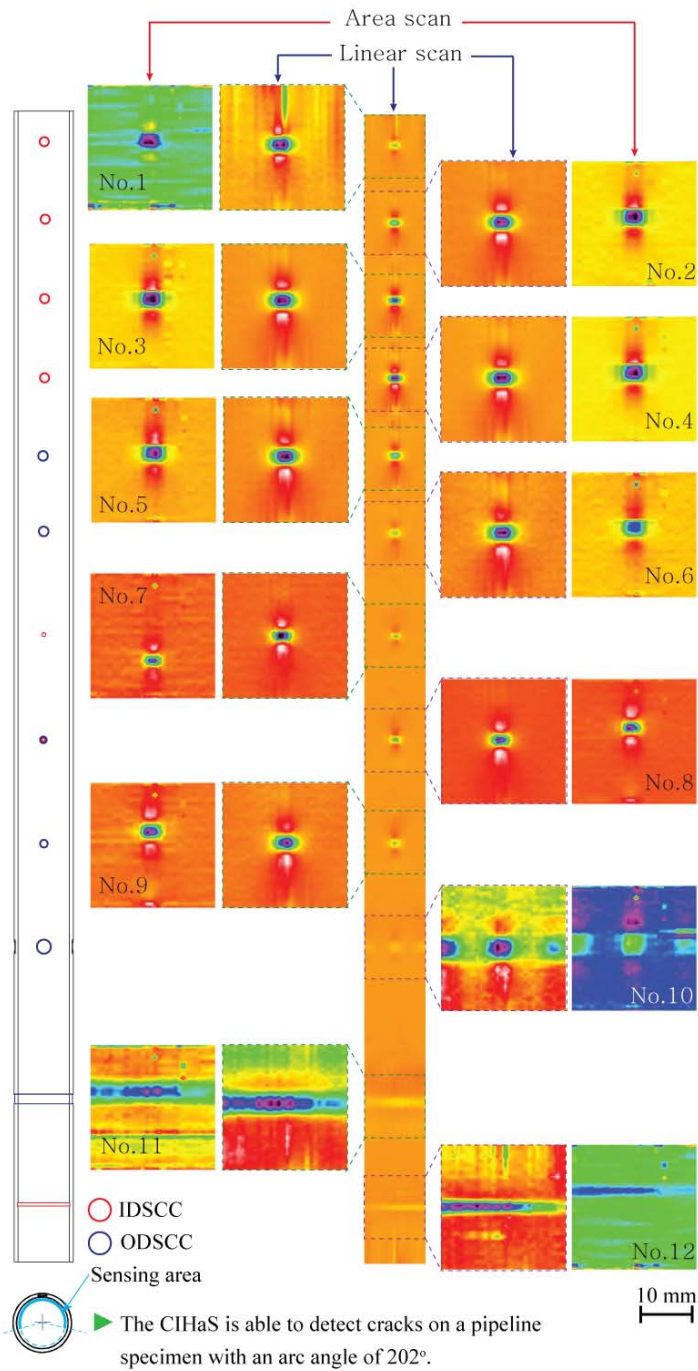
Fig. 4-19 Experiment results for copper alloy pipe

4.3.2. Simulation Algorithm

The simulation algorithm has five steps, as shown in the algorithm in Fig. 4-20 [49].
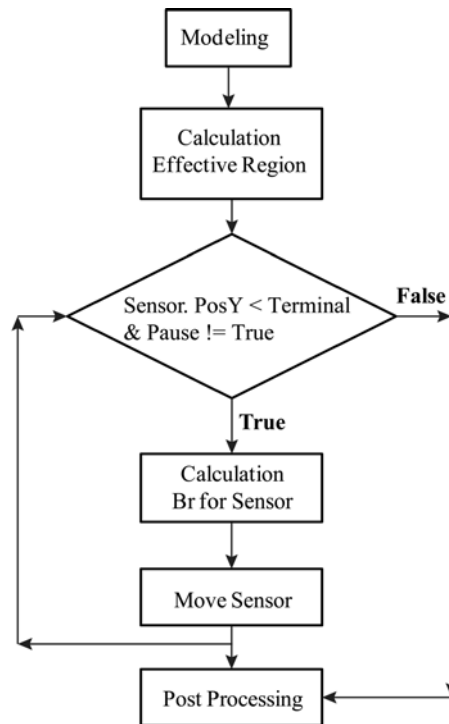
Fig. 4-20 Simulation algorithm.

Step 1: Modeling

In this step, the pipe and crack are modeled and automatically calculated for various crack types (i.e., through, OD, COD, ID). In addition, some magnetic properties of pipe material such as permeability and conductivity, as well as on sensor characteristics (diameter, spatial resolution, and number of sensors) are input.

Step 2: Calculation of effective region

Generally, at each sensor position, the total magnetic field induced by each crack must be calculated even that the crack is far to the sensor. As this task is lengthy and

requires a large amount of computational resources, we propose a method for the calculation of the effective region of each crack based on a threshold value that is a percentage of the maximum possible magnetic field of a crack, as shown in Fig. 4-21. If the sensor is positioned outside of this region, the crack will not affect the magnetic field of sensor, and the magnetic field induced by the crack at the sensor is set equal to zero.
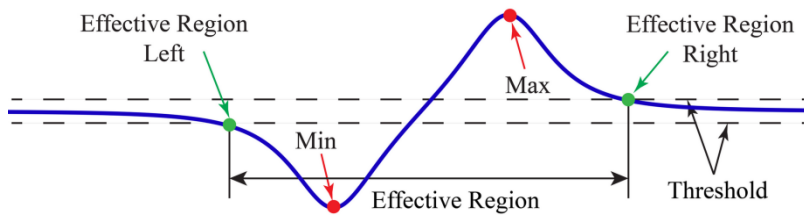
Fig. 4-21 Effective length calculated from the software.

Step 3: Calculation of Br

In this step, the magnetic field at each sensor position is calculated using Eqs. (5-8) and stored in a database.

Step 4: Move sensor

The position of the sensor is then increased by one scan step value. If the terminal position is reached or the pause button is pressed, the simulation pauses and the post-processing mode is commenced; otherwise, the algorithm returns to step 3.

Step 5: Post-processing

In post-processing mode, data obtained from the simulation, such as the calculated effective region, section view, and small area view, is analyzed. This step is also useful for solving inverse NDT problems such as determining the crack shape, depth, diameter, or volume.

4.3.3. Maximum Magnetic Charge Factor

The maximum magnetic charge factor ξ_0 can be obtained by establishing an optimized function Q [45], [47]. In this section, the Q function is the comparison between the center section view of crack image of magnetic field in the experimental result and simulated result ($B_{RMS}|_{Section}^{Re}$) [49]. The $B_{RMS}|_{Section}^{Re}$ is the relative magnetic flux density to no crack area, as described in Eq. (4-16). It was taken at the sensor number 16. The optimized function Q includes 9 crack images at 3 kHz, as expressed in Eq. (4-18) [49]. By finding the mimimum value of function Q using *'fminsearch'* function in Matlab software, the ξ_0 was found to be 0.017 Wb/mm^2, as shown in Fig. 4-22 [49].

$$B_{RMS}|_{Section}^{Re} = B_{RMS}|_{Section} - B_{RMS}|_{Section}^{no\ crack} \tag{4-16}$$

$$Q = \sum_{Cracks} \left[\left(B_{RMS}|_{Section}^{Re\_Exp} \right)^2 - \left(B_{RMS}|_{Section}^{Re\_Sim} \right)^2 \right]^2$$

$$= \sum_{Cracks} \left[\left(B_{RMS}|_{Section}^{Re\_Exp} \right)^2 - \xi_0^2 . P^2 \right]^2 \tag{4-17}$$
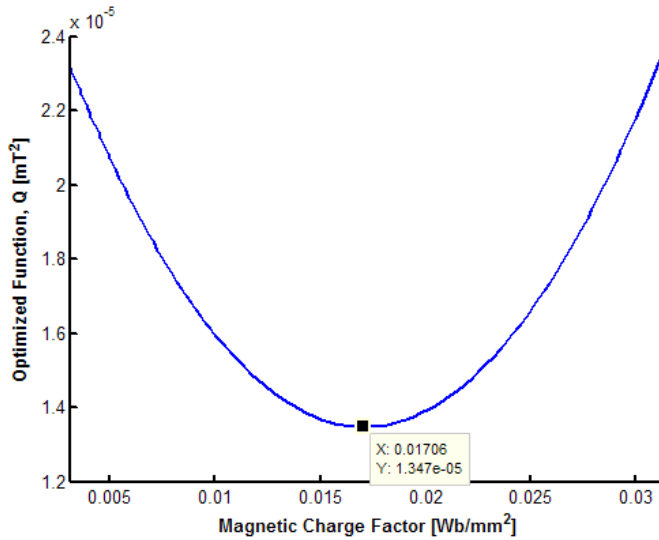
Fig. 4-22 Optimized function curve

4.3.4. Effective Region

In order to find the relationship between the effective region and the crack diameter, eight through-type cracks in the abovementioned copper pipe with diameters ranging from 1 to 8mm were sampled; the simulation parameters are shown in Table 2. Based on the recorded data on the maximum percentage value (effective threshold, P) for each crack, as shown in Fig. 4-23, a good linear relationship can be observed between the effective region (L, in Fig. 4-21) and the crack diameter (w). This relationship can be described by Eq. (4-18) [49].

$$L = (-0.472\ln P + 1.552)w - 0.426\ln P + 9.78 \qquad (4\text{-}18)$$
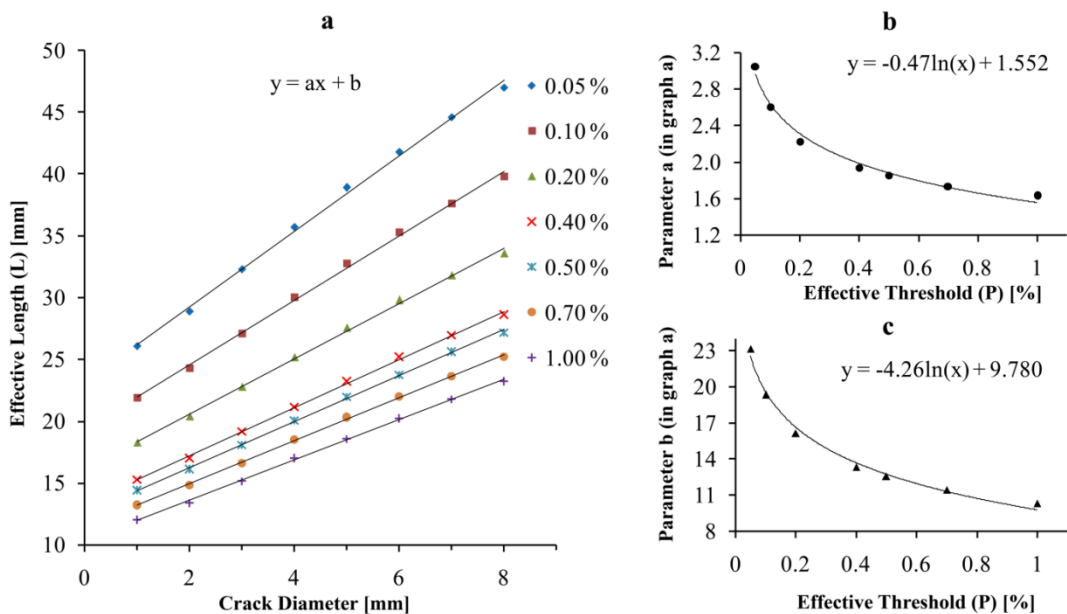
Fig. 4-23 Calculation of effective region of a crack according to diameter.

4.3.5. Comparison

Fig. 4-24 shows the experimental and simulated results in two types of data: magnetic intensity (B), and differential of magnetic intensity ($\partial B/\partial x$) at 3 kHz [49]. The simulation parameters are listed in Tables 1 and 2. A crack image has two peaks in the B images and three peaks in the $\partial B/\partial x$ images. It shows a good agreement in the peaks

position between the simulated and the experimental results, as well as the trend of the data. As seen the ID cracks Nos. 1-3 and OD cracks Nos. 5-6, the crack image increases in width (Fig. 4-24(b), (c), (e), and (f)) and peak value (Fig. 4-24(d) and (g)) when the crack depth increases. This relationship also holds for the width of the crack, as can be observed from through cracks 4, 7, and 8. A clear skin effect can also be observed in cracks 2 (ID) and 6 (OD), which have the same width and similar depth but the width and peak value of their images are quite different. The center of peak-peak in the section view of B (Fig. 4-24(c)) and the middle peak in the section view of $\partial B/\partial x$ image (Fig. 4-24(g)) indicate the position of crack.
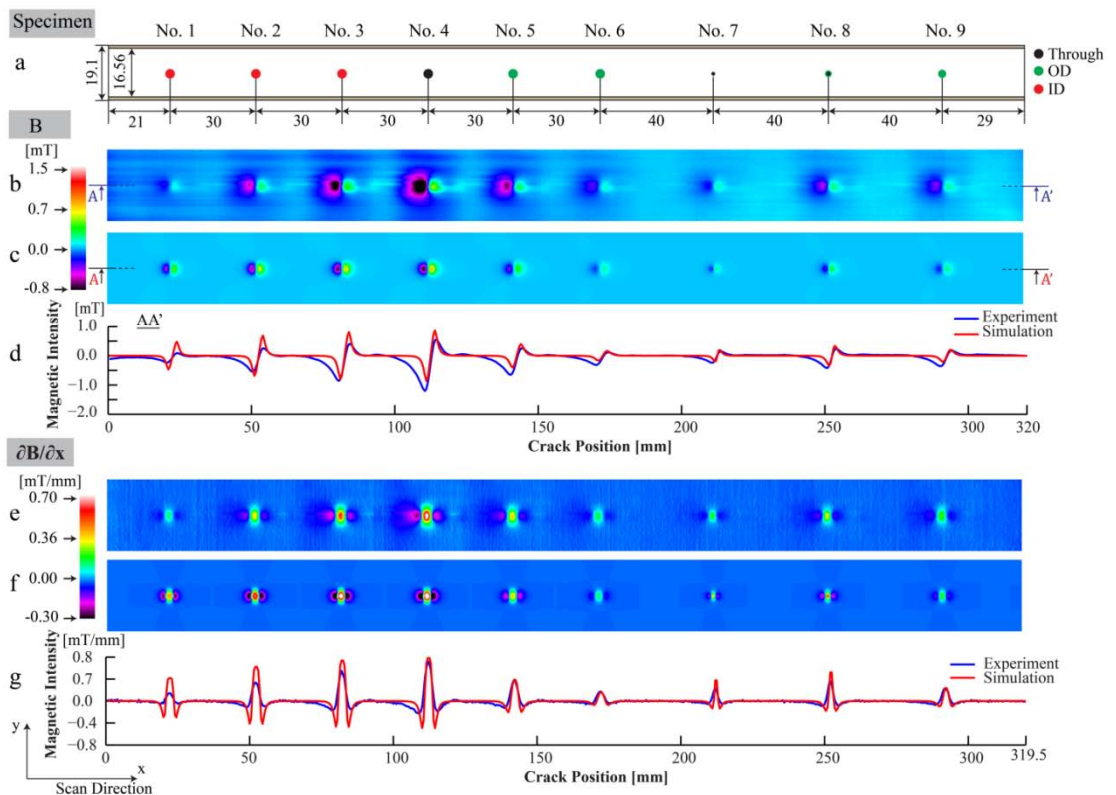
Fig. 4-24 Comparison of simulated results with experimental results: magnetic intensity, B (a, b, c), and differential magnetic intensity in scan direction, $\partial B/\partial x$ (e, f, g)

However, the crack images in the experimental results are larger than those in the simulation. The enlargement of crack images is caused by neighboring cracks distorting

the magnetic field of the bobbin coil when a given crack is scanned; this effect demonstrates that the eddy current in the experimental pipe used in the experiment are not really uniform, as is assumed in the simulation. To resolve this discrepancy, the length of the bobbin coil should be reduced. Thus, the affection of the neighboring cracks to the induced current of the bobbin coil is reduced.

Using the dipole model method, the distribution of magnetic fields around cracks can be simulated quickly at each sensor position: to simulate 9 cracks in a 400 mm length of pipe with 0.5 mm scan steps, for instance, an Intel(R) (Core 2 Quad, Q9400, Speed 2.66GHz, 3GB RAM) with Win XP x32, SP2 computer requires only 64.7s [49]. In addition, the simulated data can be analyzed quickly in post-processing. This simulation method could prove useful in quickly delivering training in the use of bobbin-type magnetic cameras to inspect cracks in heat exchanger tubes. Help to solve the inverse problem in non-destructive evaluation such as estimation of crack's volume, depth and diameter. Using the post-processing mode, which can display various types of information such as normal and differential data and section and area views, it is easy to understand and process detailed data produced by this method.

CHAPTER 5 CONCLUSIONS

This study presents a simulation method for electromagnetic testing using a dipole model. For several decades, the dipole model has been known as a fast and easy simulation method for simulation of a magnetic flux leakage around a crack in the magnetic flux leakage testing. However, the dipole model for eddy current testing has just started for simulation of a magneto-optical film since the few years ago. The current study provided an improvement of the dipole model for the eddy current testing which is used to simulate AC-type magnetic cameras.

The development of dipole model was verified by comparing its simulation results with simulation results of the finite element method using commercial ANSYS software and experimental results using area-type magnetic camera and cylinder-type magnetic camera. The comparison was done for cracks on plate specimen and small-bore piping specimen, and a good agreement among the three methods has been found. The dipole model results image quality is cleaner compare with the finite element model results because the finite element method has accumulate errors due to the size of elements and using a lots of equations, but the dipole model method uses only few simple equations. The signal trend in the dipole model results and experimental results is good, as observed in the section line signal of several crack shape on plate specimen and hole-type inner and outer diameter cracks on a small-bore pipe. The quality and trend of crack image when changing diameter, depth and shape of crack are good agree for the three results.

The evaluation of crack shape and sizes in nondestructive evaluation has been done by using the dipole model method. The crack shape such as rectangular, triangular, and elliptical sectional on plate specimen was recognized by using peak-to-peak distance in the differential signal. The crack volume was estimated by using sum absolute data of crack image for the three methods.

Table 5-1 shows the improvements of the proposed dipole model with the previous dipole model and the FEM. Various kinds of crack shape such as rectangular, triangular, elliptical, circular, stepped sectional shape were implemented in dipole model software with a 3-D graphic display and data analysis. In the dipole model, several equations in

finite integral form are used which is easy to understand and implement in the software; thus, the simulation speed is very fast. For example, for simulation of a hole-type crack in a pipe, the finite element method had 484,713 elements of components and took 21 m 24 s. Conversely, the dipole model took only 3 s. The fast and easy performances of the dipole model make it possible to simulate a scanning state of a bobbin-type magnetic camera inside a small pipe. But, it is impossible to use the finite element method. The fast simulation, easy data analysis and good accurate of simulation result of the dipole model provide a potential and convenient method for development quantitative evaluation method in nondestructive evaluation.

Table 5-1 Comparison among the FEM, previous and improved dipole model

Simulation Method	Component Geometry	Implementation	Simulation Time	Error	Scanning State
FEM	Any	Difficult	Slow	High	No
Previous Dipole Model	**Plate specimen:** • Rectangular	Easy	Fast	Low	No
Improved Dipole Model	**Plate specimen:** • Rectangular • Triangular • Elliptical • Steeped crack **Pipe specimen:** • Through • Outer diameter • Complicated outer diameter • Inner diameter	Easy	Fast	Low	Yes

The further research should be done by establishing dipole model for more various kinds of crack shape, more complicated shape or a general case of crack shape and specimen geometry. It will become a reliable and powerful simulation method which can be widely used in industry. In addition, inverse problems in the NDE could be done by establishing a library which contains information of crack and its equivalent magnetic signal. Thus, once we obtain

the magnetic signal in the experiment result, we can refer to the library to pick up the equivalent information of the crack such as size and shape.

REFERENCES

[1]   T. Vetterlein, S. Georgi, Tiede, M. Wagener, H. Rongen, "Automated Dye Penetrant Systems with Process Control and Documentation in the Aerospace Industry" ECNDT 2006 - Mo.2.1.2.

[2]   N. P. Migoun, A. B. Gnusin, M. Stadthaus, G. R. Jaenisch, "New Potentials of Penetrant Testing", ECNDT 2006 - Th.1.8.1.

[3]   Brian Larson, "Study of the Factors Affecting the Sensitivity of Liquid Penetrant Inspections: Review of Literature Published from 1970 to 1998", DOT/FAA/AR-01/95, 1/2002.

[4]   https://www.asnt.org/MajorSiteSections/NDT-Resource-Center/Introduction%20to%20Nondestructive%20Testing

[5]   http://www.iprt.iastate.edu/assistance/nde/tools/radiographic

[6]   V. Nagarkar, J. Gordon, S. Vasile, P. Gothoskar, F. Hopkins, "High resolution X-ray sensor for non destructive evaluation", Nuclear Science Symposium and Medical Imaging Conference Record 1996, Vol. 43, pp. 1559 - 1563.

[7]   X. Wang, B. Wong, K. Khoo, C. Tui, F. Foo, "Image Enhancement for Radiographic Non-Destructive Inspection of the Aircraft", APCNDT 2006.

[8]   J. Xu, T. LIU, B. Wong , S. Hassan, "Automatic X-ray Crack Inspection for Aircraft Wing Fastener Holes", AeroNDT 2010.

[9]   X. Wang, B. Wong, C. Tui, "Real-time Radiographic Non-destructive Inspection for Aircraft Maintenance", WCNDT 2008.

[10]   Wei Dong, Zhou Zhenggan, Ni Xiansheng, "Application of linear frequency modulation pulse compression in air-coupled ultrasonic testing", ICACC 2010, Vol. 2, pp. 53 – 57.

[11]   Y. Ito, T. Masuda, K. Nagao, K. Matsuoka, "Ultrasonic testing system for ERW mill", IAS '97, Vol. 2, pp. 866 – 872.

[12]   Liu Guimin, Yong Qingsong, Li Bin, "Experiments on the Ultrasonic Testing of the Austenitic Dissimilar Welding Joint of Steel Type 22SiMn2TiB", ICMTMA 2011, Vol. 2, pp. 156 – 159.

[13] Zhou Runjing, Zhang Fei, "Application of Ultrasonic for Pipeline Flaw Detection", ICEMI '07, pp. 4-472 - 4-475.

[14] Peter J. Shull, " Nondestructive Evaluation Theory, Techniques, and Applications", CRC Press, 1st Edition (May 8, 2002), Chapter 3.

[15] http://www.ndt-ed.org/EducationResources/CommunityCollege/Ultrasonics/Introduction/description.htm

[16] P. E. Mix, "Magnetic Particle Testing," in Introduction to Nondestructive Testing: A Training Guide, Second Edition, ed, pp. 247-299.

[17] C. E. Betz, Principles of magnetic particle testing: Magnaflux Corporation Chicago, 1967.

[18] A. Lindgren, H. Weltman, J. Reynolds, J. Halkias, W. Kaarlela, O. Molina, "Magnetic particle inspection," ASM Handbook., vol. 17, pp. 89-128, 1989.

[19] http://www.ndt-ed.org/EducationResources/CommunityCollege/MagParticle/Indications/WetExamples.htm

[20] K. Mandal and D. L. Atherton, "A study of magnetic flux-leakage signals," Journal of Physics D, vol. 31, pp. 3211-3217, 1998.

[21] P. E. Mix, "Magnetic Flux Leakage Theory," in Introduction to nondestructive testing: a training guide, ed: Wiley-Interscience, 2005, pp. 73-78.

[22] G. S. Park and E. S. Park, "Improvement of the Sensor System in Magnetic Flux Leakage-Type Nondestructive Testing (NDT)," IEEE transactions on magnetics, vol. 38, pp. 1277-1280, 2002.

[23] K. Kosmas, C. Sargentis, D. Tsamakis, and E. Hristoforou, "Non-destructive evaluation of magnetic metallic materials using Hall sensors," Journal of Materials Processing Technology, vol. 161, pp. 359-362, 2005.

[24] S. H. Choi, J. Y. Lee, K. C. Lee, and J. S. Hwang, "A study of leakage magnetic flux detector using Hall sensors array," Key Engineering Materials, vol. 306, pp. 235-240, 2006.

[25] G. Dobmann, G. Walle, and P. Höller, "Magnetic leakage flux testing with probes: physical principles and restrictions for application," NDT International, vol. 20, pp. 101-104, 4/1987.

[26] J Kim, "Development and Application of a Magnetic Vector Camera using Heterogeneous Magnetic Sensors", PhD Thesis, Chosun University, Korea, 2013.

[27] Lee J, Jun J, Kim J, Lee J. An application of a magnetic camera for an NDT system for aging aircraft. Journal of the Korean Society for Nondestructive Testing 2010;30(3).

[28] Kosmas K, Sargentis C, Tsamakis D, Hristoforou E. Non-destructive evaluation of magnetic metallic materials using Hall Sensors. Journal of Materials Technology 2005;161:359–92.

[29] He Y, Pan M, Luo F, Tian GY. Pulsed eddy current imaging and frequency spectrum analysis for hidden defect nondestructive testing and evaluation. NDT & E Int. 2011;44(4):344–352.

[30] P. E. Mix, "Eddy Current Theory," in Introduction to nondestructive testing: a training guide, ed: Wiley-Interscience, 2005, pp. 66-72.

[31] http://www.microwavesoft.com/eddy-current-1.gif

[32] http://www.ndt-ed.org/EducationResources/CommunityCollege/EddyCurrents/Instrumentation/impedanceplane.htm

[33] J. Jun and J. Lee, "Nondestructive evaluation of a crack on austenitic stainless steel using a sheet type induced current and a Hall sensor array," Journal of Mechanical Science and Technology, vol. 22, pp. 1684-1691, 2008.

[34] J. Jongwoo, C. Myungki, and L. Jinyi, "Nondestructive Evaluation of Austenitic Stainless Steel Using CIC-MFL and LIHaS," Magnetics, IEEE Transactions on, vol. 47, pp. 3959-3962, 2011.

[35] K.-K. Park, "Consideration of Penetrant Inspection," Journal of the Korean society for nondestructive testing, vol. 3, pp. 36-39, 1984.

[36] J. S. Hwang and J. Y. Lee, "Magnetic Images and NDT of the Express Train Wheel Using a High Speed Scan-Type Magnetic Camera," Key Engineering Materials, vol. 417-418, pp. 169-172, 2010.

[37] Lee J, Jun J, Kim J, Choi H, Le M. Bobbin-type Solid-state Hall Sensor Array with High Spatial Resolution for Cracks Inspection in Small-Bore Piping Systems. IEEE Trans Mag 2012;48(11): 3704–3.

[38] J. Jun, Y. Park, and J. Lee, "Real time visualization of alternating magnetic fields using 2-dimensional integrated Hall sensor array," Journal of Electrical Engineering-Elektrotechnicky Casopis, vol. 61, pp. 32-35, 2010.

[39] J. M. Kim and J. Y. Lee, "Inspection of the Internal Cracks on a Pipe Using a Cylinder-Type Magnetic Camera," Key Engineering Materials, vol. 417-418, pp. 165-168, 2010.

[40] J. Lee, J. Jun, J. Kim, and J. Lee, "An application of a magnetic camera for an NDT system for aging aircraft," Journal of the Korean Society for Nondestructive Testing, vol. 30, 2010.

[41] J. N. Lee, J. S. Hwang, S. Choi, and J. K. Lim, "Detection Probability Improvement for Nondestructive Evaluation Using a Magnetic Camera," Key Engineering Materials, vol. 306-308, pp. 241-246, 2006.

[42] J. Y. Lee and J. S. Hwang, "A Study of the Quantitative Nondestructive Evaluation Using the Cross Type Magnetic Source and the Magnetic Camera," Key Engineering Materials, vol. 321-323, pp. 1447-1450, 2006.

[43] J. Jun, J. Lee, and D. Park, "NDT of a nickel coated inconel specimen using by the complex induced current-magnetic flux leakage method and linearly integrated hall sensor array," Journal of Mechanical Science and Technology, vol. 27, pp. 375-82, 2007.

[44] Jun J, Lee J, Kim J, Le M, Lee S. Eddy current imager based on bobbin-type Hall sensor array for nondestructive evaluation in small-bore piping system. In: Proceedings of the 39th annual review of progress in quantitative nondestructive evaluation. Denver, Colorado, USA; July 12-20 2012.

[45] Le M, Lee J, Jun J, Kim J. Estimation of sizes of cracks on pipes in nuclear power plants using dipole moment and finite element methods. NDT & E Int 2013;58:56-63.

[46] Le M, Lee J, Lee S, Shoji TA. A simulation of magneto-optical Eddy current imaging. NDT & E Int 2011;44:783–788.

[47] Le M, Lee J, Jun J, Kim J, Moh S, Shin K. Hall sensor array based validation of estimation of crack size in metals using magnetic dipole models. NDT & E Int 2013;53:18-25.

[48] Le M, Vu H, Kim J, Angani C.S, Lee J. Quantitative Evaluation of Corrosion in a Thin Small-Bore Piping System Using Bobbin-Type Magnetic Camera. JONE 2014;33(1):74-81.

[49] Le M, Vu H, Kim J, Angani C.S, Lee J. Fast simulat ion of alternat ing magnetic fields around a crack in a pipeline syst em using a dipole model method. Int. J. Numer. Model 2014. DOI: 10.1002/jnm.1929.

[50] J. M. Jin, The finite element method in Electromagnetics, Wiley-IEE Press, ISBN 0471438189, 2002.

[51] D. Z. Chen, K. R. Shao and J. D. Lavers, A very fast numerical analysis of Benchmark Models of Eddy current testing for steam generator tube. IEE Trans. Mag. 2002, Vol. 38, No. 5, pp. 2355-2362.

[52] B. Klimpke, " A hybrid magnetic field solver using a combined finite element/ boundary element field solver", Presented at the U.K. Magnetics Society Conference. "Advanced Electromagnetic Modelling & CAD for Insdustrial Application", Feb 2003, pp. 1-8.

[53] R. V. Sabarego, J. Gyselinck, C. Geuzaine, P. Dular and W. Legros, "Application of the fast multipole method to hybrid finte element-boundary element models", Journal of Computational and Applied Mathematics, Vol. 168, Iss. 1-2, pp. 403-412, 2004.

[54] C.V. Dodd and W.E. Deeds, "Analytical Solution to Eddy-Current Probe-Coil Problems," Journal of Applied Physics, Vol. 39, pp. 2829-2838, 1968.

[55] Huang H, Sakurai N, Takagi T, Uchimoto T. Design of an eddy-current array probe for crack sizing in steam generator tubes. NDT & E Int 2003;36(7):515–22.

[56] Fukutomi H, Takagi T, Nishikaw M. Remote Field eddy current technique applied to non-magnetic steam generator tubes. NDT & E Int 2001;34(1):17–23.

[57] Gotho Y, Fujioka H, Takahashi N. Proposal of Electromagnetic Inspection Method of Outer Side Defect on Steel Tube With Steel Support Plate Using Optimal Differential Search Coils. IEEE Trans Mag 2011;47(5):1006–9.

[58] Xin J, Lei N, Udpa L, Udpa SS. Nondestructive Inspection Using Rotating Magnetic Field Eddy-Current Probe. IEEE Trans Mag 2011;47(5):1070–3.

[59] COMSOL Corporation, "FEMLAB V4.4 Manual", 2013. http://www.comsol.com/

[60] Infolytica, http://www.infolytica.com/

[61] ANSYS Corporation, "Maxwell EM V15.0 Manual", 2013. http://ansoft.com/

[62] T. Theodoulidis and E. Kriezis, "Series expansion in eddy current nondestructive evaluation models," Journal of Materials Processing Technology, Vol. 161, pp. 343-347, 2005.

[63] T. P. Theodoulidis and E.E. Kriezis, "Eddy current canonical problems (with application to nondestructive evaluation)," Forsyth, GA: Tech Science Presss, 2006.

[64] T. P. Theodoulidis and J. R. Bowler, "Eddy current coil interaction with a right-angled conductive wedge," Proceedings of the Royal Society A: Mathematical, Physical and Engineering Sciences, vol. 461, pp. 3123-3139, 2005.

[65] J. R. Bowler and T. P. Theodoulidis, "Coil impedance variation due to induced current at the edge of a conductive plate," Journal of Physics D: Applied Physics, vol. 39, pp. 2862-2868, 2006.

[66] S. K. Burke, J. R. Bowler, and T. P. Theodoulidis, "An Experimental and Theoretical Study of Eddy-Current End Effects In Finite Rods and Finite Length Holes," in American Institute of Physics, 2006, pp. 361-368.

[67] Y. Li, T. Theodoulidis, and G. Y. Tian, "Magnetic Field-Based Eddy-Current Modeling for Multilayered Specimens," IEEE Transactions on Magnetics, vol. 43, pp. 4010-4015, 2007.

[68]   N. Zatsepin and V. Shcherbinin, "Calculation of the magnetostatic field of surface defects. I. Field topography of defect models," Defek-toskopiya , no. 5, pp. 50–59, Sep.–Oct. 1966.

[69]   V. Shcherbinin and A. Pashagin, "Influence of the extension of a de -fect on the magnitude of its magnetic field," Defektoskopiya , no. 4, pp.74–82, Jul.–Aug. 1972.

[70]   F. Forster, "Newfindings in the field of non -destructive magnetic leakage field inspection," NDT Int. , vol. 19, no. 1, pp. 3–14, Feb. 1986.

[71]   C. Edwards and S. Palmer, "The magnetic leakage field of surface-breaking cracks," J. Phys. D: Appl. Phys. , vol. 19, pp. 657–673, 1986.

[72]   K. Mandal and D. Atherton, "A study of magneticflux -leakage sig-nals," J. Phys. D: Appl. Phys. , vol. 31, pp. 3211–3217, 1998.

[73]   D. Minkov, Y. Takeda, T. Shoji, and J. Lee, "Estimating the sizes of surface cracks based on hall element measurements of the leakage magneticfield and a dipole model of a crack," Appl. Phys. A: Mater. Sci.Process. , vol. 74, no. 2, pp. 169–176, 2002.

[74]   D. Minkov, J. Lee, T. Shoji, Improvement of the Dipole Model of a Surface Crack, Material Evaluation, Vol. 58, No. 5, pp. 661-666, 2000.

[75]   D. Minkov, T. Shoji, Method for sizing of 3-D surface breaking flaws by leakage flux, NDT&E Int, Vol. 31, No. 5, pp. 317-324, 1998.

[76]   C. Mandache and L. Clapham, "A model for magnetic leakage   signal predictions," J. Phys. D: Appl. Phys. , vol. 36, pp. 2427–2431,2003.

[77]   S. M. Dutta, F. H. Ghorbel, R. K. Stanley, Dipole modeling of magnetic flux leakage, IEEE Trans. Mag., Vol.45, No.4, pp. 1959-1965, 2009.

[78]   S. M. Dutta, F. H. Ghorbel, R. K. Stanley, Simulation and analysis of 3-D magnetic flux leakage, IEEE Trans. Mag., Vol.45, No.4, pp. 1966-1972, 2009.

[79]   J. Lee, S. Lyu, Y. Nam, An algorithm for the characterization of surface crack by use of dipole model and magneto-optic Non-Destructive inspection system, KSME Vol. 14, No. 10, pp. 1072-1080, 2000.

[80] J. Lee, T. Shoji, D. Seo, Theoretical consideration of nondestructive testing by use of vertical magnetization and magneto-optical sensor, KSME Int J Vol.18 No. 4, pp 640~648, 2004.

[81] J. Lee, J. Hwang, T. Shoji, J. Lim, Modeling of characteristics of Magneto-optical sensor using FEM and Dipole Model for Nondestructive Evaluation, Key Engineering Materials Vols.297-300 (2005) pp.2022-2027.

[82] M. Le, "Simulation of Magneto-Optical Nondestructive Testing", Master Thesis, Chosun University, Aug. 2009.

[83] Le HM, Lee J, Lee S, Shoji T. Simulation technique of non-destructive testing using magneto-optical film. E-Journal of Advanced Maintenance 2011;3(1):25–38.

[84] Bastos J.P.A, Sadowski N (2003). Electromagnetic modeling by finite element methods. CRC Press, 1st Ed, ISBN-13: 978-0824742690.

[85] Jin J (2002). The finite element method in electromagnetics. Jonh wiley & Son, Inc, 2nd Ed. ISBN 0-471-43818-9.

[86] Peter Monk (2003). Finite Element Methods for Maxwell's Equations. Oxford UK: Oxford University Press. p. 1 ff. ISBN 0-19-850888-3.

[87] David M Cook (2002). The Theory of the Electromagnetic Field. Mineola NY: Courier Dover Publications. p. 335 ff. ISBN 0-486-42567-3

[88] Mook G, Hesse O, Uchanin V. Deep Penetrating Eddy Currents and Probes.Materials Testing 2007, 49:5, 258-264.

[89] Hagemaier D. Eddy current standard depth of penetration. Materials evaluation, vol. 43, pp. 1438-1442, 1985.

[90] Mottl Z. The quantitative relations between true and standard depth of penetration for air-cored probe coils in eddy current testing. NDT International, vol. 23, pp. 11-18, 1990.

[91] Gyimesi M., Lavers D., Pawlak T. and Ostergaard D., "Application of the General Potential Formulation in the ANSYS®Program", IEEE Transactions on Magnetics, Vol. 29, pp. 1345-1347 (1993).

[92] Gyimesi, M. and Lavers, J. D., "Generalized Potential Formulation for 3-D Magnetostatic Problems", IEEE Transactions on Magnetics, Vol. 28, No. 4 (1992).

[93]   Gyimesi, M., Lavers, J., Pawlak, T., and Ostergaard,D., "Biot-Savart Integration for Bars and Arcs", IEEE Transactions on Magnetics, Vol. 29, No. 6, pp. 2389-2391 (1993).

[94]   Zienkiewicz, O. C., Lyness, J., and Owen, D. R. J., "Three-Dimensional Magnetic Field Determination Using a Scalar Potential - A Finite Element Solution", IEEE Transactions on Magnetics, Vol. MAG-13, No. 5, pp. 1649-1656 (1977).

[95]   Mayergoyz, I. D., "A New Scalar Potential Formulation for Three-Dimensional Magnetostatic Problems", IEEE Transactions on Magnetics, Vol. MAG-23, No. 6, pp. 3889-3894 (1987).

[96]   Silvester, P. P., Cabayan, H. S., and Browne, B. T., "Efficient Techniques for Finite Element Analysis of Electric Machines", IEEE Transactions on Power Apparatus and Systems, Vol. PAS-92, pp. 1274-1281 (1973).

[97]   Demerdash, N. A., Nehl, T. W., Fouad, F. A. and Mohammed, O. A., "Three Dimensional Finite Element Vector Potential Formulation of Magnetic Fields in Electrical Apparatus", IEEE Transactions on Power Apparatus and Systems, Vol. PAS-100, No. 8, pp. 4104-4111 (1981).

[98]   Weiss, J., "Efficient Finite Element Solution of Multipath Eddy Current Problems", IEEE Transactions on Magnetics, Vol. MAG-18, No. 6, pp. 1710-1712 (1982).

[99]   Garg, V. K., and Weiss, J, "Finite Element Solution of Transient Eddy-Current Problems in Multiply-Excited Magnetic Systems", IEEE Transactions on Magnetics, Vol. MAG-22, No. 5, pp. 1257-1259 (1986).

[100]   Biro, Oszkar and Preis, Kurt, "On the Use of the Magnetic Vector Potential in the Finite Element Analysis of Three-Dimensional Eddy Currents", IEEE Transactions on Magnetics, Vol. 25, No. 4, pp. 3145-3159 (July 1989).

[101]   Gyimesi, M. and Lavers, D., "Application of General Potential Formulation to Finite Elements", Second Japan Hungarian Joint Seminar on Electromagnetics, Sapporo, Japan (1992). Applied Electromagnetics in Materials and Computational Technology, ed. T. Honma, I. Sebestyen, T. Shibata. Hokkaido University Press (1992).

[102] Gyimesi, Miklos and Ostergaard, Dale, "Mixed Shape Non-Conforming Edge Elements", CEFC '98, Tucson, AZ (1998).

[103] Ostergaard, Dale and Gyimesi, Miklos, "Analysis of Benchmark Problem TEAM20 with Various Formulations", Proceedings of the TEAM Workshop, COMPUMAG Rio, pp. 18-20 (1997).

[104] Ostergaard, Dale and Gyimesi, Miklos, "Magnetic Corner: Accurate Force Computations", Analysis Solutions, Vol 1, Issue 2, pp. 10-11 (1997-98).

[105] Biro, O., Preis, K., Magele, C., Renhart, W., Richter, K.R., Vrist, G., "Numerical Analysis of 3D Magnetostatic Fields", IEEE Transaction on Magnetics, Vol. 27, No. 5, pp. 3798-3803 (1991).

[106] ANSYS Coroporation, "ANSYS help V.11.0", 2007.

[107] Park DG, Ryu KS, Son D. Detection of magnetic phase in the steam generator tubes of NPP. InTech 2011, pp. 165–84.

[108] Obrutsky L, Renaud R, Lakhan R. Steam generator inspections: faster, cheaper and better, are we there yet? IV Conferencia Panamericana de END 2007, pp. 1–17.

[109] Lee J, Jun J, Kim J, Lee J. An application of a magnetic camera for an NDT system for aging aircraft. Journal of the Korean Society for Nondestructive Testing 2010;30(3).

[110] Kosmas K, Sargentis C, Tsamakis D, Hristoforou E. Non-destructive evaluation of magnetic metallic materials using Hall Sensors. Journal of Materials Technology 2005;161:359–92.

[111] He Y, Pan M, Luo F, Tian GY. Pulsed eddy current imaging and frequency spectrum analysis for hidden defect nondestructive testing and evaluation. NDT & E Int. 2011;44(4):344–352.

[112] Drunen G.V, Cecco V.S. Recognizing limitations in eddy current testing. NDT & E Int 1984;17(1):7–9.

[113] Sadek HM. NDE technologies for the examination of heat exchangers and boiler tubes – principles, advantages and limitations. Insight 2006;48(3):181–3.

[114] Uchanin V, Najda V. The Development of Eddy Current Technique for WWER Steam Generators Inspection. InTech 2011, pp. 145–64.

[115] Kurokawa M, Miyauchi R, Enami K, Matsumoto M. New eddy current probe for NDE of steam generator tubes. Electromagnetic nondestructive evaluation (III). IOS Press; 1999. p. 57 – 64.

[116] Joubert PY, Bihan YL, Placko D. Localization of defects in steam generator tubes using a multi-coil eddy current probe dedicated to high speed inspection. NDT & E Int 2002;35(1):53–9.

[117] Lafontaine G, Hardy F, Renaud J. X-Probe® ECT array: A high-Speed Replacement for Rotating Probes. 3nd International Conference on NDE in Relation to Structural Integrity for Nuclear and Pressurized Components, Nov 14-16, 2001, Seville Spain.

[118] Huang H, Sakurai N, Takagi T, Uchimoto T. Design of an eddy-current array probe for crack sizing in steam generator tubes. NDT & E Int 2003;36(7):515–22.

[119] Fukutomi H, Takagi T, Nishikaw M. Remote Field eddy current technique applied to non-magnetic steam generator tubes. NDT & E Int 2001;34(1):17–23.

[120] Gotho Y, Fujioka H, Takahashi N. Proposal of Electromagnetic Inspection Method of Outer Side Defect on Steel Tube With Steel Support Plate Using Optimal Differential Search Coils. IEEE Trans Mag 2011;47(5):1006–9.

[121] Xin J, Lei N, Udpa L, Udpa SS. Nondestructive Inspection Using Rotating Magnetic Field Eddy-Current Probe. IEEE Trans Mag 2011;47(5):1070–3.

[122] Le M, Lee J, Jun J, Kim J. Estimation of sizes of cracks on pipes in nuclear power plants using dipole moment and finite element methods. NDT & E Int 2013;58:56-63.

[123] Le M, Lee J, Jun J, Kim J. Nondestructive testing of train wheels using differential-type integrated Hall sensor matrixes embedded in train rails. NDT&E Int 2013;55;28-35.

[124] Kim J, Le M, Lee J, Hwang Y.H. Non-destructive testing and evaluation of far-side corrosion around rivet in jet-engine intake of aging supersonic aircraft. JONE 2014. Submitting.

[125] Jun J, Lee J, Park D: NDT of a nickel inconel specimen using by the complex induced current-magnetic flux leakage method and linearly integrated Hall sensor array. J Korean Soc Nondestr Test. 27(5), 375-382 (2007).

[126] Jun J, Choi M, Lee J, Seo J, Shin K: Nondestructive testing of express train wheel using the linearly integrated Hall sensors array on a curved surface. NDT&E Int. 44(5), 449-455 (2011).

[127] ZengZhiwei, Udpa L, Udpa SS. An efficient finite element method for modeling ferrite-core eddy current probe. Int J App Ele Mech 2010;33:481-486.

[128] ZengZhiwei, Udpa L, Udpa SS. Finite-Element Model for Simulation of Ferrite-Core Eddy-Current Probe. IEEE Trans Mag 2010;46(3):905-909.

[129] Li Y, Tian GY, Ward S. Numerical simulations on electromagnetic NDT at high speed. Insight 2006;48(2):103–8.

[130] Harfield N, Bowler J. Theory of thin-skin eddy-current interaction with surface of cracks. Journal of Applied Physics 1997;82(9):4590-4603.

[131] Badics Z, et al.. An effective 3-D element scheme for computing electromagnetic field distortions due to defects in eddy-current nondestructive evaluation. IEEE Trans. Mag. 1997;33(2):1012-1020.

[132] Bowler JR, Johnson M. Pulsed eddy-current response to a conducting half-space. IEEE Trans. Mag. 1997;33(3):2258–64.

[133] Li Y, Theodoulidis TP, Tian GY. Magnetic field-based eddy current modelling for multilayered specimens. IEEE Trans Magn 2007;43(11):4010–5.

ACKNOWLEDGEMENT

I would like to express my gratitude to my advisor, Prof. Jinyi Lee at Department of Control, Instrumentation and Robot Engineering for his supports. That he willingly shared the knowledge with me during the research and writing of my thesis. His advices are always very helpful in both doing research and living in Korea.

I would also like to thanks to Prof. Nak-Yong Ko, Prof. Chang-Hyun Cho, Prof. Keun-Chang Kwak and all professors at Department of Control, Instrumentation and Robot Engineering for teaching me the knowledge and help me to complete the thesis. I would also like to thanks to Prof. Kisu Shin at Department of Weapon Systems, Korea National Defense University and Dr. Jongwoo Jun at Nedtech Company, Busan. I like to thanks to my lab-mates of Sensor Device Laboratory, Chosun University for 5 years of my studying and living in Korea.

I am extremely thankful to my parents, all my family and friends for their love, support, and encouragement in every moment of my life. From my heart, I always wish and pray for them.

Le Minh Huy

저작물 이용 허락서

학 과	제어계측공학과	학 번	20117763	과 정	박사
성 명	한글 레민후이 한문 영문 LE MINH HUY					
주 소	광주시 동구 지산동 504-8					
연락처	e-mail : kebitmat_f@yahoo.com					
논문제목	한글: 비파괴 평가를 위한 교류형 자기카메라의 다이폴 모델 기반 시뮬레이션 기법에 관한 연구 영문: Simulation Method based-on Dipole Model for the AC-type Magnetic Camera in the Nondestructive Testing and Evaluation					

본인이 저작한 위의 저작물에 대하여 다음과 같은 조건 아래 조선대학교가 저작물을 이용할 수 있도록 허락하고 동의합니다.

- 다 음 -

1. 저작물의 DB 구축 및 인터넷을 포함한 정보통신망에의 공개를 위한 저작물의 복제, 기억장치에의 저장, 전송 등을 허락함
2. 위의 목적을 위하여 필요한 범위 내에서의 편집과 형식상의 변경을 허락함(다만, 저작물의 내용변경은 금지함)
3. 배포·전송된 저작물의 영리적 목적을 위한 복제, 저장, 전송 등은 금지함
4. 저작물에 대한 이용기간은 5 년으로 하고, 기간종료 3 개월 이내에 별도의 의사 표시가 없을 경우에는 저작물의 이용기간을 계속 연장함
5. 해당 저작물의 저작권을 타인에게 양도하거나 출판을 허락을 하였을 경우에는 1개월 이내에 대학에 이를 통보함
6. 조선대학교는 저작물 이용의 허락 이후 해당 저작물로 인하여 발생하는 타인에 의한 권리 침해에 대하여 일체의 법적 책임을 지지 않음
7. 소속 대학의 협정기관에 저작물의 제공 및 인터넷 등 정보통신망을 이용한 저작물의 전송·출력을 허락함

동의여부 : 동의(○) 반대( )

2014년 8월 25일 Le Minh Huy (인)

조선대학교 총장 귀하